The design and thermal measurement of III-V integrated micro-coolers for thermal management of microwave devices

James Glover

School of Engineering and Sustainable Development

De Montfort University

A thesis submitted for the degree of

Doctor of Philosophy

Sept 2016

I would like to dedicate this thesis to my family and friends, without their constant pushing and reminders to write-up my work this thesis would never have been possible.

Acknowledgements

I would like to thank my primary supervisor, Dr. Chris Oxley, for all of his support, advice and understanding throughout this drawn-out process. I am sure that he will be happy to finally see the end of this project.

I would like to acknowledge all the collaborators involved in this project as a whole, including; Geoff Dunn and Alex Stephen from the University of Aberdeen, Ata Khalid and David Cumming from the University of Glasgow, and Miguel Montes Bajo and Martin Kuball from the University of Bristol. And, of course, I would like to thank the Engineering and Physical Sciences Research Council (EPSRC) for financially supporting this project.

There have also been a number of people at De Montfort University that have been there to help and advice me throughout this project, including; Gwynne Evans for his secondary supervision work and introduction to LaTeX for this thesis, Alistair Duffy for his persistent support and encouragement, and Manbir Sambhi, Ashok Karavadra, and Prakash Patel for their technical and equipment assistance.

And finally, a special thank you to all of those who have pushed me to get this finished; Susan Glover, Stephen Glover, Claire Glover, Nick Glover, Peter Glover, Krishna Nama Manjunatha, Salah Maswoud, Mohamed Ismaeel Maricar, and Nare Gabrielyan.

Abstract

Modern high frequency electronic devices are continually becoming smaller in area but capable of generating higher RF power, thereby increasing the dissipated power density. For many microwave devices, for example the planar Gunn diode, standard thermal management may no longer be sufficient to effectively remove the increasing dissipated power. The work has looked at the design and development of an active micro-cooler, which could be fully integrated with the planar Gunn diode at wafer level as a monolithic microwave integrated circuit (MMIC). The work also resulted in the further development of novel thermal measurement techniques, using micro-particle sensors with infra-red (IR) thermal microscopy and for the first time to measure thermal profiles along the channel of the planar Gunn diode.

To integrate the gallium arsenide (GaAs) based planar Gunn diode and micro-cooler, it was first necessary to design and fabricate individual GaAs based planar Gunn diodes and micro-coolers for thermal and electrical characterisation. To obtain very small area micro-coolers, superlattice structures were investigated to improve the ratio between the electrical and thermal conductivities of the micro-cooler. To measure the specific contact resistivity of the superlattice based micro-cooler contacts, the Reeves & Harrison TLM (transmission line method) was used as it included both horizontal and vertical components of the contact resistance. It was found, for the GaAs based micro-cooler, only small amounts of cooling (<0.4 °C) could be obtained, therefore the novel temperature measurement method using micro-particle sensors placed on both the anode and cathode contacts was utilised.

The bias probes used to supply DC power to the micro-coolers were found to thermally load these very small structures, which led to anomalously high measured cooling temperatures of >1 °C. A novel approach of determining if the measured cooling temperature was due to cooling or probe loading was developed.

A 1D model for the integrated micro-cooler was developed and the results indicated that when the micro-cooler was used as a cooling element in a monolithic microwave integrated circuit, the supporting

substrate thickness was very important. Simulation showed to obtain cooling the substrate thickness had to be very thin (<50 μm), which may preclude the use of GaAs micro-coolers as part of a monolithic microwave integrated circuit.

Nomenclature

Roman Symbols

Symbol	Description
ℓ	Gap length between TLM contacts
ȩ	Surface emissivity
Ŗ	Emitted IR radiation
Ŗ_{b}	Emitted IR radiation by an ideal blackbody
Ŗ_{0}	Background IR radiation
A	Area
d	Length of TLM contact
d_B	Barrier thickness
e^-	Electron
h^+	Hole for an electron
I	Current
J	Current density
k	Boltzmann constant
L	Length
L_T	Transfer length
L_{ac}	Anode-cathode separation
q	Charge of an electron
Q	Net cooling power
Q_t	Cooling power of a micro-cooler

Q_{hc}	Heat conduction power of a micro-cooler
Q_{jh}	Joule heating power of a micro-cooler
Qd	Net cooling power density of a micro-cooler
Qd_{t}	Cooling power density of a micro-cooler
Qd_{hc}	Heat conduction power density of a micro-cooler
Qd_{jh}	Joule heating power density of a micro-cooler
R	Resistance
R_{C}	Contact resistance
R_{p}	Probe resistance
R_{BC}	Bottom contact resistance of a micro-cooler
R_{DUT}	Internal DUT resistance
R_{pc}	Probe to contact resistance
R_{SH}	Sheet resistance of the bulk semiconductor
R_{SK}	Sheet resistance directly underneath the contact
R_{SL}	Bulk electrical resistance of the semiconductor layers of a micro-cooler
R_{TC}	Top contact resistance of a micro-cooler
R_{tot}	Total resistance
S	Seebeck coefficient
T	Temperature
t	Thickness
T_{c}	Temperature of the cold side of a thermoelectric cooler
T_{h}	Temperature of the hot side of a thermoelectric cooler
T_{amb}	Ambient temperature
T_{rise}	Temperature rise from operating temperature
V	Voltage
W	Width

Greek Symbols

ΔT	Temperature difference between the hot and cold sides of a thermoelectric cooler
δT	Temperature difference across an individual barrier within a thermionic cooler
κ	Thermal conductivity
κ_{SL}	Thermal conductivity of a superlattice
λ	Wavelength
λ_{E}	Electron relaxation length
ϕ	Barrier height
ρ	Resistivity
ρ_{C}	Specific contact resistivity
σ	Electrical conductivity
σ_{C}	Specific contact conductivity
θ	Thermal resistivity
Θ	Thermal impedance
Θ_{C}	Thermal impedance of a micro-cooler
Θ_{S}	Thermal impedance of a substrate

Material Abbreviations

AlGaAs	Aluminium gallium arsenide
AlGaN	Aluminium gallium nitride
GaAs	Gallium arsenide
GaN	Gallium nitride
InAlAs	Indium aluminium arsenide
InGaAs	Indium gallium arsenide
InP	Indium phosphide
Si	Silicon

Acronyms

AFM	Atomic force microscopy
CPW	Coplanar waveguide
DC	Direct current
DUT	Device under test
EBL	Electron beam lithography
EPSRC	Engineering and Physical Sciences Research Council
HEMT	High electron mobility transistor
IR	Infra-red
IV	Current-voltage
MBE	Molecular beam epitaxy
MESFET	Metal semiconductor field effect transistor
MMIC	Monolithic microwave integrated circuit
MOCVD	Metal organic chemical vapour deposition
MTTF	Mean time to failure
NDR	Negative differential resistance
RF	Radio frequency
SEM	Scanning electron microscope
SThM	Scanning thermal microscopy
TEC	Thermoelectric cooler
TLM	Transmission line method
VNA	Vector network analyser
VPE	Vapour phase epitaxy

Contents

Acknowledgements ii

Abstract iii

Nomenclature v

1 Introduction 1
- 1.1 Motivation . . . 1
- 1.2 Outline of the work . . . 2
- 1.3 Thesis structure . . . 2
  - 1.3.1 Chapter 2: Background . . . 2
  - 1.3.2 Chapter 3: Infra-red thermal measurement . . . 3
  - 1.3.3 Chapter 4: Planar Gunn diodes . . . 3
  - 1.3.4 Chapter 5: Micro-coolers . . . 4
  - 1.3.5 Chapter 6: Simulations and optimisation of micro-cooler designs . . . 4
  - 1.3.6 Chapter 7: Conclusions & future work . . . 4
- 1.4 Summary of research findings . . . 5
- 1.5 List of my publications . . . 5
  - 1.5.1 Journal papers . . . 5
  - 1.5.2 Conference proceedings . . . 6
  - 1.5.3 Posters . . . 6

2 Background 7
- 2.1 Thermal measurement techniques . . . 7
  - 2.1.1 Contact thermal measurements . . . 8
  - 2.1.2 Non-contact thermal measurements . . . 9
  - 2.1.3 IR thermal microscopy . . . 10
- 2.2 Gunn diodes . . . 17
  - 2.2.1 Vertical vs. planar Gunn diodes . . . 21
- 2.3 Micro-coolers . . . 23

2.3.1 Thermoelectric effect 24
2.3.2 Thermoelectric cooling 25
2.3.3 Miniaturisation of coolers 30
2.3.4 Integration 32

3 Infra-red thermal measurement **33**
3.1 Operation of the IR microscope 36
3.2 Micro-particle sensor 36
3.3 Micro-particle emissivity 38
3.4 Micro-particle characterisation 38
3.5 Micro-particle measurement techniques 41
3.6 Micro-particle manipulation 42
3.6.1 Optical grid for particle manipulation 44

4 Planar Gunn diodes **46**
4.1 Understanding Gunn diode notations 47
4.2 RF measurements 49
4.2.1 VNA measurements 49
4.2.2 Spectrum analyser measurements 50
4.3 DC measurements 50
4.3.1 Semi-automatic IV measurement system 52
4.4 Thermal measurement techniques 55
4.4.1 Conventional IR thermal measurements 55
4.4.2 Micro-particle IR thermal profile measurements 61
4.5 Summary 68

5 Micro-coolers **69**
5.1 Design 69
5.2 Electrical measurement techniques 72
5.2.1 IV characterisation 72
5.2.2 TLM measurements 73
5.3 Thermal measurement techniques 79
5.3.1 Thermal analysis of thermal loading 85
5.3.2 Analytical analysis of thermal loading 87
5.4 Summary 92

6 Simulations and optimisation of micro-cooler designs **93**
6.1 1D Model to match literature results 94
6.2 Combining cooling equations to make a complete 1D model 97
6.3 How material properties of the semiconductor will affect cooling performance 101

6.3.1 Effect of contact resistance 103
6.3.2 Thermal conductivity 104
6.3.3 Comparing experimental results with the model 108
6.4 Creating model of integrated micro-cooler 108
6.4.1 Effect of substrate thickness 109
6.5 Summary 114

7 Conclusions & future work 115
7.1 Infra-red thermal measurement 115
7.2 Planar Gunn diode 115
7.3 Micro-coolers 116
7.4 Integration of micro-cooler 117
7.5 Future work 118

Appendix A1 120

Appendix A2 122

Appendix B1 125

Appendix B2 130

Appendix B3 134

Appendix B4 137

Appendix B5 140

Appendix B6 142

List of Figures

2.1 Spectral emissive power . . . 11
2.2 Basic set-up of an IR thermal microscope. . . . 12
2.3 Multi-layer IR emission of transparent materials. . . . 14
2.4 Plot comparing the measured temperature rise from a conventional (uncoated) IR thermal measurement with measurements using a black paint coating and micro-particle sensors. . . . 17
2.5 Basic current-voltage plot for a Gunn diode. . . . 18
2.6 Scanning electron microscope images of a vertical and a planar Gunn diode. . . . 18
2.7 Basic layer structure of a Gunn diode. . . . 19
2.8 Gunn domain formation. . . . 20
2.9 Schematic view of Gunn layers and direction of current flow. . . . 21
2.10 Basic coplanar waveguide structure. . . . 23
2.11 Closed loop made of two dissimilar materials with electron current flow. . . . 26
2.12 Basic thermoelectric cooler. . . . 27
2.13 Basic semiconductor thermoelectric cooler, using both n-type and p-type materials. . . . 28
2.14 Electrical interconnections between many PN semiconductor pairs in a TEC. . . . 28
2.15 Multi-stage TEC. . . . 29
2.16 Basic superlattice structure. . . . 31

3.1 De Montfort University's IR microscope set-up. . . . 34
3.2 Emitted IR radiation from a micro-particle sensor. . . . 37
3.3 Plot comparing the level of IR radiation detected as a function of the diameter of the micro-particle sensor. . . . 41
3.4 Scientifica micro-manipulator. . . . 42
3.5 Optical image of micro-particle sensor and manipulator probe. . . . 43
3.6 (a) Scientifica's micro-manipulator controller and (b) Scientifica's LinLab software. . . . 44

3.7 Optical grid. 45

4.1 Current flow between anode and cathode contacts of a planar Gunn diode. 47
4.2 Schematics of planar Gunn diode contact structures. 48
4.3 Basic representation of S-parameter pairs for a 2-port network. . . 49
4.4 Basic spectrum analyser set-up. 50
4.5 Schematic showing the resistances involved with probing a DUT. . 51
4.6 Basic set-up for 4-probe IV measurements. 52
4.7 De Montfort University's microscope table with four probes for analysing DC of on-wafer devices. 53
4.8 Semi-automatic IV measurement software. 54
4.9 IV characteristic of three planar Gunn diodes. 54
4.10 Conventional IR thermal measurement on a SLAO1×60 Gunn diode. 57
4.11 Conventional IR thermal measurement on a SHAO1.5×120 Gunn diode. 58
4.12 Conventional IR thermal measurement on an ACAO1×120 Gunn diode. 59
4.13 Conventional IR thermal measurement on an ACAO3×120 Gunn diode. 60
4.14 Schematic showing measurement direction in relation to Gunn contacts for thermal profiles made with a micro-particle sensor manipulated across the channel of a planar Gunn diode. 62
4.15 Schematic showing measurement direction in relation to Gunn contacts for thermal profiles made with a micro-particle sensor manipulated along the channel of a planar Gunn diode. 62
4.16 An ACAO3×120 profiled across the channel. 63
4.17 An ACAO4×120 profiled along the channel. 64
4.18 Current distribution along ACAO4×120 channel. 65
4.19 An ACAO3×120 profiled along the channel. 66
4.20 13 micro-particle sensors placed within the channel of an ACAO3×120 planar Gunn diode. 67
4.21 An ACAO3×120 profiled along the channel. 68

5.1 Basic cooler structure, showing cathode contact on top of the mesa and anode contacts off-mesa, to the sides of the mesa. 70
5.2 (a) Cross-sectional schematic of the contact geometry and wafer layers for the micro-cooler wafers. (b) Plan-view image of micro-cooler with a round structure and ring-like top contact. 71
5.3 Measured R_{tot} of micro-coolers against area. 73
5.4 Example TLM contact layout. 73

5.5 Plot from TLM measurements. 74
5.6 Basic representation of the resistances involved when a current flows between two ohmic contacts. 74
5.7 Simple bulk semiconductor structure with two sheet resistances. . 75
5.8 Representation of the resistances involved when a current flows between two ohmic contacts, showing the additional R_E. 76
5.9 Comparison of specific contact resistivity for all 6 micro-cooler fabrication iterations analysed. 77
5.10 IV characteristics, showing Schottky contact behaviour. For four TLM pad separation distances measured on the 1st micro-cooler wafer iteration. 78
5.11 Temperature comparison between two micro-particle sensors, on different device contacts. 80
5.12 Micro-cooler B14 with a central (ring-like) cathode and surrounding anode. 82
5.13 Thermal analysis of B14. 83
5.14 Thermal analysis of ΔT between the micro-particle sensors on the anode and cathode contacts of cooler B9. 83
5.15 Thermal analysis of ΔT between the micro-particle sensors on the anode and cathode contacts of cooler A9. 84
5.16 Micro-particle sensors placed on neighbouring TLM contacts to check for thermal loading from the DC probes. 85
5.17 Measured temperature difference against bias current when particle B was closer to the bias probes. 86
5.18 Measured temperature difference against bias current when particle A was closer to the bias probes. 87
5.19 Cooler A9 appearing to show exceptional levels of cooling. 89
5.20 Analysed plot showing that the higher current points do not fit with the conventional behaviour. 90
5.21 Micro-coolers with thermally isolated cathodes via bond wires to probe pads on an alumina stand-off. 91
5.22 Analysis on the thermal results from a thermally isolated cooler. . 91

6.1 Plot of net cooling power density against barrier thickness for three barrier heights. 95
6.2 Plot of current density against barrier thickness for three barrier heights. 96
6.3 Initial 1D model plot of net cooling power density against barrier thickness for three barrier heights. 96
6.4 Plot of approximated current density against barrier thickness for three barrier heights. 97

6.5 1D model plot of net cooling power density against barrier thickness for three barrier heights. 98
6.6 Basic 1D model structure of a micro-cooler. 101
6.7 Modelled plot showing how ΔT_{max} changes with respect to ρ_C. . . 103
6.8 Modelled plot showing how ΔT changes with respect to I, for four values of ρ_C. 104
6.9 Modelled results to analyse the thermal conductivity of $In_{1-x}Ga_xAs$ 106
6.10 Modelled results to analyse the thermal conductivity of $Al_xGa_{1-x}As$. 106
6.11 Comparison between experimental results with model. 108
6.12 Basic structure of a planar Gunn diode integrated as part of the micro-cooler. 109
6.13 Micro-cooler and substrate structure. 109

List of Tables

2.1 Comparison of thermal measurement techniques. 16
2.2 Comparison between vertical and planar Gunn diodes. 22

3.1 Measurement accuracy for micro-particle diameters on a gold background. 39
3.2 Measurement accuracy for micro-particle diameters on an aluminium background. 40

4.1 List of Gunn diode contact structures. 48
4.2 Planar Gunn diodes measured by conventional IR thermal microscopy. 56

5.1 Micro-cooler wafer specification. 70
5.2 Selection of micro-cooler geometries and contact metallisations. . 81

6.1 No semi-insulating substrate. 113
6.2 50 μm substrate. 113
6.3 600 μm substrate. 113

Chapter 1

Introduction

1.1 Motivation

As modern electronics develop, they increase in power capacity while decreasing in area. This leads to very high dissipated power density. The generated heat, therefore, needs to be spread out or removed as quickly as possible. An example where this is likely to become problematic is the planar Gunn diode. Early planar Gunn diodes were shown to have fundamental oscillations around 100 GHz [1], but as the planar Gunn diode has been developed, the fundamental frequency has been increased [2; 3; 4; 5]. The fundamental frequency was increased by reducing the channel length, while the input power and efficiency remained very similar, therefore, the power density within the channel region was higher. As the development of the planar Gunn diode continues towards terahertz frequencies (for applications such as communications, radar, imaging, spectroscopy, and security screening [6]), the channel length will continue to reduce and the dissipated power density increase. There will be a point where standard passive cooling will be insufficient for these devices. To generate useful RF output powers of the order of 1 mW (or greater) with an efficiency of around 1% at frequencies of ∼220 GHz, the estimated heat flux will be in excess of 145 kW/cm^2 compared with 70 kW/cm^2 for the state-of-the-art 77 GHz vertical Gunn diode with a gold integral heat-sink [7]. Typically, 77 GHz vertical Gunn diodes have a thermal impedance of ∼20 °C/W, with a typical input electrical power of 3.5 W this will result in a rise in junction temperature of approximately 70 °C. The electrical performance and reliability of these vertical Gunn diodes is commercially viable and this temperature rise will be used as a base line for the planar Gunn diode. As the planar Gunn diode has at least twice the power dissipation of the vertical Gunn diode novel heat management solutions will have to be found and devel-

oped. One of these methods will be an integrated active cooler, which uses an electro-thermal effect.

1.2 Outline of the work

The focus of this research work was to consider an active cooling technology that could be integrated with a planar Gunn diode, at wafer level. One technology considered was thermoelectric cooling. This required a semiconductor cooler structure that utilised a current flow that was perpendicular to the wafer surface, on which the planar Gunn diode layers are grown. For a planar Gunn diode structure with a channel length and channel width of 2 and 120 μm (2×120) respectively, the total planar Gunn area was around 300×300 μm and therefore the cooler had to have a similar area. For wafer level integration with the planar Gunn diode, the micro-cooler needed to consist of materials that could be grown during the same wafer growth process as the Gunn diode. Initial planar Gunn diodes were fabricated from GaAs based materials, and so the same GaAs based materials were needed for the micro-cooler structure. Published work also indicated that superlattice structures would give an improved thermoelectric type cooling.
Novel IR thermal microscopy techniques were developed to measure the operational temperatures of both the planar Gunn diode and the micro-cooler structures. As there were so many possible micro-cooler structures some of the work was carried out by developing simple 1D models for the micro-cooler.

1.3 Thesis structure

1.3.1 Chapter 2: Background

The chapter describes the basic background information for each of the three main areas of this research:

1) Thermal measurement techniques

The section describes the different types of thermal measurement available and undertakes a review of them. The conventional infra-red (IR) thermal microscopy technique is described in detail and the use of IR thermal microscopy with micro-particle sensors is introduced.

2) Gunn diodes

Gunn diodes and their different geometries (vertical and planar) are described. A brief history of them is also included, followed by a comparison between the vertical and planar Gunn diodes.

3) Micro-coolers

The section introduces micro-coolers and the thermoelectric effect that they utilise. The function of the more traditional PN thermoelectric cooler (TEC) is described, followed by the problems this cooler style has with miniaturisation and integration. This then leads to a description of the thermionic effect and superlattice micro-coolers.

1.3.2 Chapter 3: Infra-red thermal measurement

The chapter details the IR thermal microscope system used in this research. The work focusses on the use of micro-particle sensors for thermal measurements on different materials, for example those transparent to IR or with low surface emissivities. The calibration and measurement temperature accuracy of the micro-particles are discussed and the manipulation methods to place the micro-particles, including a developed optical camera software, which superimposes a measurement grid onto a still frame of the device under test (DUT). The grid is used to measure distances.

1.3.3 Chapter 4: Planar Gunn diodes

The different planar Gunn diode structures measured within this research are documented. Followed by an outline of the electrical and thermal measurements used to characterise the Gunn diodes. These included IV characteristics and channel thermal profile measurements. Thermal channel measurements of the planar Gunn diode were made, for the first time, using the IR micro-particle sensor technology. The thermal measurements on the planar Gunn diode are shown and discussed

1.3.4 Chapter 5: Micro-coolers

The micro-cooler wafer structure used in this project is introduced, along with the micro-cooler geometries. The IV characteristic and contact resistance measurement techniques used to measure the micro-cooler structures are described. The importance of detailed specific contact resistivity measurements for these devices is also discussed.
A novel thermal measurement technique to analyse both the anode and cathode temperatures of the micro-cooler at the same time is introduced, and the findings reported. Problems due to thermal loading from bias probes are discussed and novel analyses to verify its occurrence are described.

1.3.5 Chapter 6: Simulations and optimisation of micro-cooler designs

The chapter describes the development of a detailed 1D model to represent a vertical micro-cooler structure. This model was verified against previously published micro-cooler results. Equations were developed to show how cooling performance changes with different, important material properties (for example; thermal conductivity, contact resistance, etc.). The importance of reducing the contact resistance is shown, as well as a method to estimate the thermal conductivity of a superlattice consisting of III-V semiconductor alloys. Simulations also considered using an aluminium gallium arsenide (AlGaAs) superlattice micro-cooler as an element in an integrated circuit, the subsequent effect on its cooling performance, and the importance of substrate thickness. To the author's knowledge, the effect of substrate thickness on micro-cooler performance has never been looked at in detail.

1.3.6 Chapter 7: Conclusions & future work

The chapter brings together the main findings from this research work, including a discussion on difficulties to be faced when integrating the micro-cooler as part of a monolithic microwave integrated circuit (MMIC).

1.4 Summary of research findings

Areas of novelty reported in this research work are:

- The first use of micro-particle sensors with IR thermal microscopy for measuring thermal profiles along the central channel region of a planar Gunn diode.
- A novel temperature comparison method, for measuring the temperature difference between the heated anode and cooled cathode contacts on a superlattice micro-cooler.
- The development of a novel method to ascertain if a measured micro-cooler temperature difference between the anode and cathode contacts is due to cooling or probe-loading [8].
- An analysis of the micro-cooler as part of a MMIC, showed that the cooling performance is very dependent on the thickness of the supporting substrate. For an AlGaAs superlattice micro-cooler, it was found that the substrate thickness had to be less than 50 μm to observe any real cooling. Even then the cooling was very small (<0.4 °C). The work suggests the use of micro-coolers as a heat management element in a MMIC is unlikely to be feasible on a GaAs substrate [9].

1.5 List of my publications

1.5.1 Journal papers

1. J. Glover, A. Khalid, D. R. S. Cumming, M. M. Bajo, M. Kuball, A. Stephen, G. M. Dunn, and C. H. Oxley, "On wafer thermal characterization of miniature gallium arsenide microcoolers with thermal loading from DC probes," Microw. Opt. Technol. Lett., vol. 56, no. 11, pp. 2699-2700, Nov. 2014. (Reference [8])
2. J. Glover, A. Khalid, A. Stephen, G. Dunn, D. Cumming, and C. H. Oxley, "Micro-coolers fabricated as a component in an integrated circuit," Semicond. Sci. Technol., vol. 30, no. 1, p. 5, 2015. (Reference [9])
3. A. Stephen, G. M. Dunn, C. H. Oxley, J. Glover, M. M. Bajo, D. R. S. Cumming, A. Khalid, and M. Kuball, "Improvements in thermionic cooling through engineering of the heterostructure interface using Monte Carlo simulations," J. Appl. Phys., vol. 114, no. 4, p. 43717, 2013.

4. A. Stephen, G. M. Dunn, J. Glover, C. H. Oxley, M. M. Bajo, D. R. S. Cumming, A. Khalid, and M. Kuball, “Micro-cooler enhancements by barrier interface analysis,” AIP Adv., vol. 4, no. 2, p. 27105, Feb. 2014.

1.5.2 Conference proceedings

1. J. Glover, R. H. Hopper, M. I. Maricar, A. Khalid, D. R. S. Cumming, M. M. Bajo, M. Kuball, G. M. Dunn, A. Stephen, and C. H. Oxley, “Novel Infra-red (IR) Thermal Measurements on GaAs Micro-coolers,” in ARMMS RF and Microwave society, 2012, pp. 1-7.
2. R. H. Hopper, J. Glover, G. A. Evans, and C. H. Oxley, “Thermal measurement of RF and microwave devices using a novel thermal probe,” in 2nd Annual Passive RF and Microwave Components Seminar, 2011, pp. 69-71.
3. M. I. Maricar, J. Glover, G. A. Evans, A. Khalid, V. Papageorgiou, G. M. Dunn, A. Stephen, M. M. Bajo, M. Kuball, D. R. S. Cumming, and C. H. Oxley, “Planar gunn diode characterisation and resonator elements to realise oscillator circuits,” in International Conference on Advanced Nanomaterials & Emerging Engineering Technologies, 2013, pp. 597-601.

1.5.3 Posters

1. J. Glover, C. H. Oxley, A. Khalid, D. R. S. Cumming, M. M. Bajo, M. Kuball, A. Stephen, and G. M. Dunn, “Analysis to determine external heating of wafer-based GaAs micro-coolers,” in IeMRC 8th Annual Conference, 2013.

Chapter 2

Background

2.1 Thermal measurement techniques

Thermal measurement techniques have been developed over many years to measure the operating junction temperatures of solid-state electronic devices. The temperatures may be the average temperature from a collection of active/passive devices in a circuit, or the temperature of a single electronic device, for example a transistor or diode. All active electronic devices will produce thermal energy (known as Joule or self heating). The amount of Joule heating will increase as the bias level to the device is increased and for most electronic devices there is a maximum temperature of operation which is determined by the required mean time to failure (MTTF) of a device. A device can still be operated at higher bias levels, resulting in higher temperatures, however this will compromise its reliability and therefore its estimated MTTF. To determine the reliability of an electronic device, it is necessary to know its operating temperature for a particular bias condition and this can be difficult to compute accurately. If looking at a collection of electronic devices (combined as part of a circuit or chip), the thermal interactions between the devices will be difficult to model. Also, the maximum junction temperature for a device may need to be determined, which may only be due to a small area (or hot-spot) on the device i.e. a semiconductor junction or metal contact. These hot-spots can equally be very difficult to compute with any accuracy. Therefore, highly specialised temperature measurements of electronic devices have been developed and can be categorised in two classifications; (i) contact and (ii) non-contact methods.

2.1.1 Contact thermal measurements

Contact thermal measurements use a measuring sensor, which is in direct physical contact with the device. Provided the sensor has a thermal mass that is much smaller than the device being measured it will acquire the same temperature as the device and is said to be in isothermal contact. Common examples of contact temperature measurement systems are the mercury-in-glass thermometer and the electrical thermocouple probe. Temperature measurements using these methods are very straightforward, for example the mercury-in-glass thermometer only requires an initial calibration to ascertain the expansion of the mercury over the required temperature range and will give near real-time results (the only delay being for the mercury within the thermometer to reach equilibrium with the temperature of the device being measured). Examples of mercury thermometers include clinical or jam making thermometers (a lot of these thermometers no longer use mercury but a coloured alcohol because of the potential health risk with the toxicity of mercury).

For the mercury or alcohol based thermometers, the probe tip (pool of mercury at the end of the thermometer) is relatively large and so is ideal for measuring the average temperature of relatively large items. However, an electrical thermocouple probe can be made much smaller (typical commercially available probes can be as small as 200 μm in diameter and are constructed by welding two dissimilar metal wires together). The temperature measurement depends on an electrical voltage that is generated between the two dissimilar metals and the magnitude of this voltage increases with temperature (as described by the Peltier effect, discussed in section 2.3 of this chapter). As with the mercury thermometer, the thermocouple needs an initial calibration (normally between two known temperatures; the transformation of pure water to ice, 0 °C, and the vaporisation of pure water, 100 °C) to set the voltage to a known temperature. The probe tip can then be used to measure an unknown temperature. However, the thermal mass of the probe tip will determine the speed in obtaining the measured temperature as well as the maximum thermal spatial resolution. A measurement probe with a large thermal mass will take longer to heat up and reach isothermal equilibrium with the device being measured. It will also act as a thermal conductor removing heat from the device being measured, this will result in the measured surface temperature being suppressed by the heat lost within the probe, limiting the measurement accuracy. However, in the case of AFM/SThM (Atomic Force Microscopy/Scanning Thermal Microscopy), the probe is heated by a laser (used to measure the deflection of the probe's cantilever) and will transfer some heat to the sample being measured, resulting in a higher measured surface temperature [10].

The mapping of the surface temperature of a device will be limited to the size of the probe, if hot-spots are smaller than the probe they will not be correctly resolved. The probe (which is most often metal) can also interfere with the electrical performance of the electronic device under test (DUT).

2.1.2 Non-contact thermal measurements

With non-contact thermal measurement techniques there is no probe in physical contact with the DUT. This eliminates the heat spreading problem. There are a number of non-contact thermal measurement techniques and these can be broken down into further subcategories; (i) electrical thermal measurement and (ii) optical thermal measurement.

Electrical thermal measurements

Electrical measurement techniques utilise the thermal dependence of an electrical parameter in an electronic device, for instance the change in electrical conductance of a semiconductor with temperature. The electrical methods can only observe the average temperature change of the whole structure, and will be unable to resolve hot areas of the structure or an individual device if multiple devices are contained within a single structure.

Optical thermal measurements

Optical thermal measurement techniques are dependent on optical properties as a function of temperature (usually of a specific wavelength in the electro-magnetic spectrum) to obtain the temperature of a device. These methods can either utilise emitted or reflected radiation. Both methods have their advantages and disadvantages.
One form of optical thermal measurement, using reflected electro-magnetic radiation, is Raman thermal spectroscopy. This is widely used to thermally profile electronic devices with a thermal spatial resolution approaching 500 nm [11]. With Raman thermal spectroscopy, a source of radiation (usually a focused single-frequency laser) is shone on the point at which the temperature measurement is to be made. When the radiation is reflected off the device surface, the temperature of the device will cause a small shift in the wavelength of the radiation. The shift in wavelength can be used to calculate the temperature at the chosen point. Reflected optical thermal measurements only require an initial calibration

for a given laser source by determining the reflected wavelength shift for a given change in temperature. However, the laser source can interfere with the electrical performance of a device as some heating and free carrier generation will occur at the point of the measurement. This can be minimised by considering the laser power and by using a wavelength that is smaller than the band-gap of the semiconductor being measured. Reflected optical measurements require long periods of time to average over a number of measurements (to increase the reliability of the measurement) and they can only be performed at a single point. Therefore, to produce a detailed thermal profile of a device surface will require the focal point of the laser to be repositioned at different locations across the device surface, and a number of measurements made and averaged; this can be a very long process. Infra-red (IR) thermal microscopy is another type of non-contact, optical thermal measurement, however it does not use the reflected radiation from a laser source, like Raman spectroscopy. IR thermal microscopy is completely passive. It depends on the natural IR radiation emitted by a device, the higher the temperature of a device the more IR radiation will be emitted. It can be calibrated by comparing the emitted radiation (of an unbiased device) with the radiation of a blackbody at the same temperature. The ratio of these two quantities is the surface emissivity (ę) of the device, which can be complicated as it is dependent on the surface material, finish, and topology.

2.1.3 IR thermal microscopy

IR microscopy is a quasi-real-time measurement enabling a 2D temperature map to be produced of small electronic devices. The area that can be imaged is dependent on the magnification of the microscope objective (figure 2.2). Low magnification objectives ($\times 1$) enable thermal maps to be made over relatively large areas (a few square millimetres), while high magnification objectives ($\times 25$) enable more detailed thermal maps over smaller areas (hundreds of microns squared). The low magnification objective is ideal for locating hot surface areas on an electronic device. Higher magnification objectives can then be used to focus on the hot areas to determine a more accurate thermal map and location of hot-spots on the device surface. A medium frequency range of IR radiation (mid IR of wavelength, $\lambda = 2.5$ to 6 μm) is used in most commercial IR microscopes, giving a maximum spatial resolution of approximately 3 μm (figure 2.1). This frequency range is preferable because it has a good balance of spatial resolution (due to relatively low wavelengths) and spectral emissive power at temperatures approaching room temperature ($\sim$300 K).

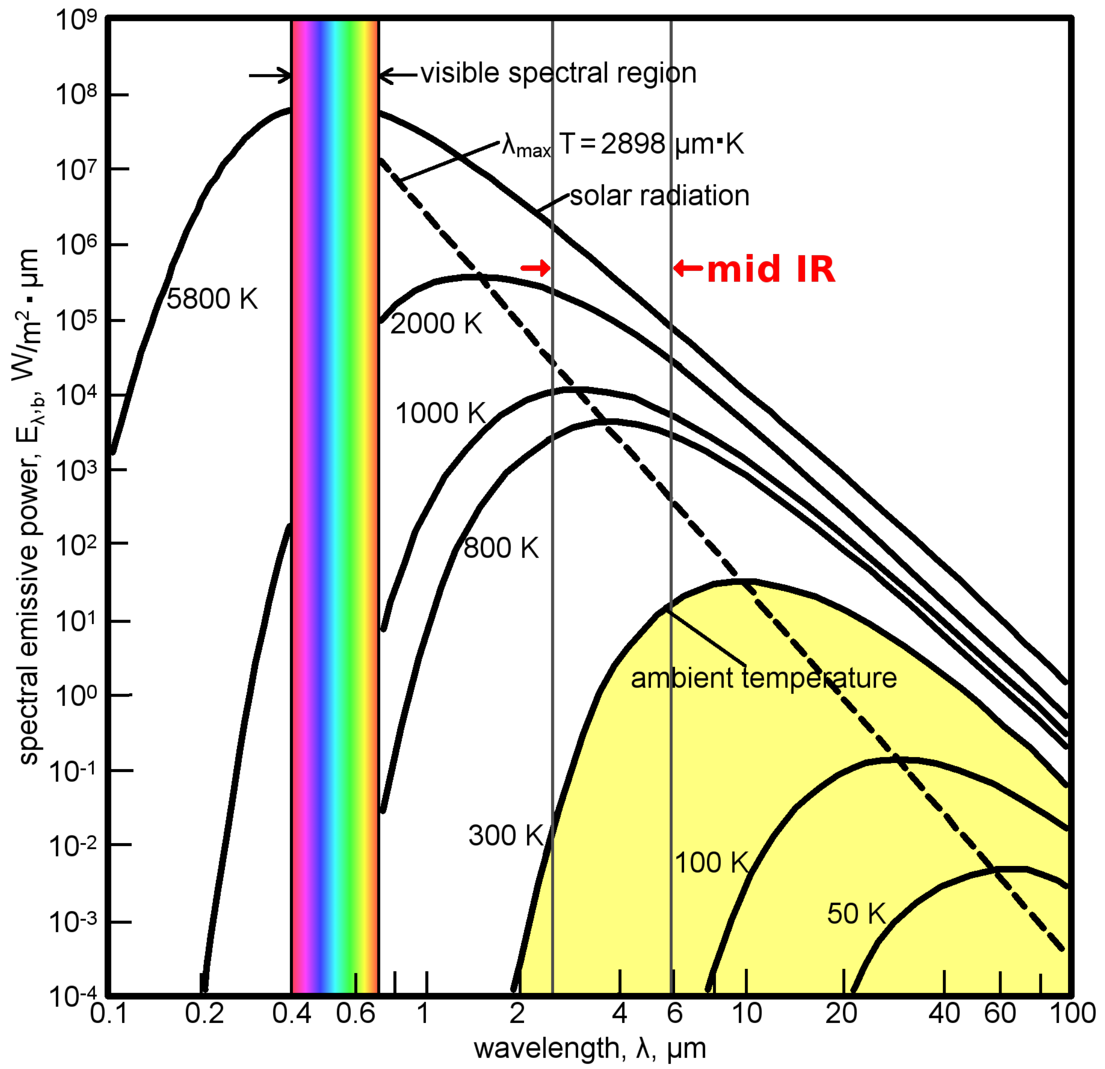

Figure 2.1: *Spectral emissive power from 50 - 5800 K [12].*

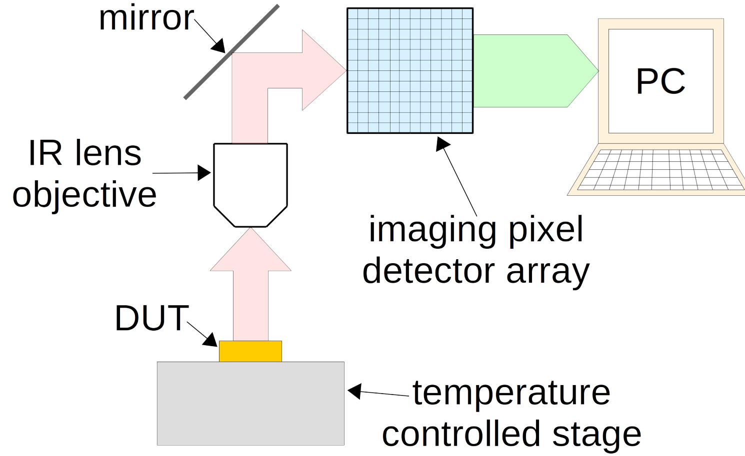

Figure 2.2: *Basic set-up of an IR thermal microscope. Including; temperature controlled stage, lens objective, and a detector array.*

To make a surface temperature map of a device, the IR microscope requires calibration against a blackbody. A blackbody is the most efficient surface radiator of IR radiation. Also, the surface emissivity of the DUT must be measured. This is fully described below.

Blackbody radiation

Blackbody radiation is the maximum level of emitted IR radiation (for a given temperature and wavelength range) and is said to be a perfect emitter of IR radiation.
The IR microscope uses a material property known as surface emissivity (ȩ) to determine the surface temperature map of a device. The surface emissivity of a material is (most simply) defined as:

$$ȩ = \frac{Ŗ}{Ŗ_{b}} \tag{2.1}$$

Where Ŗ is the emitted radiance from the device (W/sr·m^2) and $Ŗ_b$ is the emitted radiance from a blackbody (W/sr·m^2) at the same temperature and over the same wavelength range (when no background radiation is observed).

The surface emissivity is therefore calculated by comparing the level of emitted IR radiation (Ŗ) from a DUT with an ideal blackbody radiator ($Ŗ_b$) at the same temperature and range of wavelengths.

Work by P. Webb [13] included background radiation ($Ŗ_0$) in the calculation to obtain a more accurate surface emissivity, see equation (2.2).

$$ȩ = \frac{(Ŗ_{T} - Ŗ_{0T})}{(Ŗ_{bT} - Ŗ_{0T})} \quad [13] \tag{2.2}$$

Where $Ŗ_T$ is the device radiance (W/sr·m^2), $Ŗ_{0T}$ is the background radiation (W/sr·m^2), and $Ŗ_{bT}$ is the blackbody radiance (W/sr·m^2), all at the same temperature T.

By measuring the device radiance at two temperatures (T_1 and T_2) $Ŗ_{0T}$ can be removed giving a revised expression for the surface emissivity, see equation (2.3).

$$ȩ = \frac{(Ŗ_{T1} - Ŗ_{T2})}{(Ŗ_{bT1} - Ŗ_{bT2})} \quad [13] \tag{2.3}$$

Where $Ŗ_{T1}$ and $Ŗ_{T2}$ are the device radiances (W/sr·m^2) at temperatures T_1 and T_2 respectively, and $Ŗ_{bT1}$ and $Ŗ_{bT2}$ are the corresponding blackbody radiances (W/sr·m^2) at temperatures T_1 and T_2 respectively.

The IR microscope will enable a value of the device surface emissivity (ȩ) to be determined at every pixel of the IR detector array (figure 2.2), thereby producing an emissivity map across the whole area of the device surface. For a single temperature emissivity map, the radiance emitted by the unbiased device (Ŗ) is measured at a single temperature (T). In this case the background radiance ($Ŗ_0$) has to be accurately measured (equation (2.2)) to give a computed surface emissivity. Using the above 2-temperature emissivity correction (equation (2.3)) the surface of the device is heated to two temperatures (T_1 and T_2) and the surface emissivity is again computed. This is the preferred method, particularly if the surface emissivity is low (∼0.1). After a surface emissivity map has been determined the microscope system can be used to make thermal maps over the same area of the device as the emissivity map. Biasing the device will cause self-heating, measuring the emitted radiance and knowing the surface emissivity enables a temperature map of the device to be determined. As a detector array is used (enabling an area of the device surface to be imaged in real-time) a quasi-real-time thermal image can be obtained.
The stages of the measurement are as follows:

1. An emissivity map is made (comparing the radiance at each detector pixel with the radiance from a blackbody at the same temperature).

2. A reference image is made (the magnitude of radiance being emitted at each pixel, when the device is unbiased and at a known surface temperature).

3. A thermal image is made (the magnitude of radiance being emitted at each pixel, when the device is biased, enabling the surface temperature to be mapped).

All three images of a thermal measurement need to be made at a known and constant operating temperature. If the operating temperature varies, the IR microscope can compensate for this based on the trends observed from the stored data of the blackbody calibration curve and the surface emissivity map of the DUT.

Material emissivities

The accuracy of IR thermal microscopy is dependent on the computed emissivity value (at the point of the measurement) to be both accurate and sufficiently high ($\geq$0.3) to obtain a good thermal map.
When the emissivity of a material is low, $\sim$0.1, the emitted IR radiation (Ŗ) will be a similar level to the background radiation ($Ŗ_0$), therefore the temperature readings will be very noisy, significantly reducing the temperature accuracy. For example gold contacts have a very low surface emissivity ($\sim$0.02) and will give less reliable temperature measurements compared to materials with a higher surface emissivity.
Most electronic devices are fabricated on semiconductor materials that are transparent to IR radiation, this makes accurate measurement of the surface emissivity using IR very difficult, if not impossible, as the emitted IR radiation will be recorded from underlying layers as well as from the surface of the semiconductor material (figure 2.3).

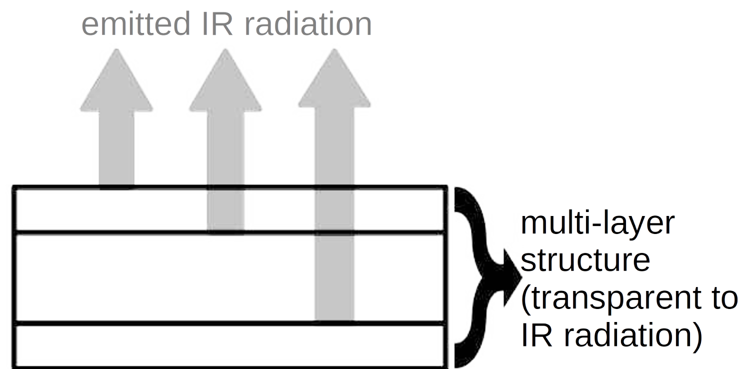

Figure 2.3: *Multi-layer IR emission of transparent materials.*

If an accurate surface emissivity cannot be obtained then neither can an accurate surface temperature. Many of the semiconductors used in electronic devices are transparent to IR radiation, for example silicon (Si), gallium arsenide (GaAs), indium phosphide (InP), and gallium nitride (GaN).

The above surface emissivity problems have traditionally been solved by painting the surface of the DUT black, to give a non-transparent surface with a high emissivity. This coating is in isothermal contact with the device surface and so will spread the heat across the coating of paint, reducing the observed peak temperatures. The paint will therefore reduce the thermal spatial resolution of the measurement. Removing this coating of paint from a device after testing is very difficult without damaging the device and therefore can only be used on sample devices, which will not be used afterwards. To overcome some of these problems an IR thermal measurement technique has been developed, which uses a high-emissivity micro-particle sensor to make more accurate point temperature measurements on any material [14; 15] (this will be discussed in detail in chapter 3).

Micro-particle sensors are very useful for making temperature measurements on semiconductors which are transparent to IR radiation (for example GaAs, InP, and GaN). Using a conventional IR thermal measurement technique will give rise to error as the surface emissivity will not be accurately known. The transparent semiconductor gives the impression of a higher surface radiance, because of the multiple layers of emitted IR radiation being detected. This in turn will increase the measured surface emissivity, thereby suppressing the measured temperature. Coating the device with a layer of black paint will allow temperature measurements to be made, however as already discussed the coating will spread the heat, thereby averaging the temperature over a much larger area and suppressing hot-spot temperatures. The surface area of the micro-particle sensor is small and so, unlike the paint coating, does not spread the heat, allowing for higher, more accurate temperature measurements. A comparison of the three techniques is shown in figure 2.4.

A comparative summary of different thermal measurement techniques is given in table 2.1.

Table 2.1: *Comparison of thermal measurement techniques.*

Thermal Measurement Technique	**Advantages**	**Disadvantages**
Conventional IR thermal microscopy	+ Measurements can be made on metals + Multiple lenses enable both large and small areas to be imaged/measured + Quasi-real-time measurement	- Spatial resolution of 3 μm, due to wavelength of IR radiation - Measurements can only be made on semiconductors if a coating is applied to the device's surface (which will cause heat spreading) - Requires high emissivity material - Comparative measurement (requires images of both unpowered and powered states)
Micro-Raman spectroscopy	+ Spatial resolution of $<$1 μm + Measurements can be made on semiconductors	- Measurements cannot be made on metals - Delayed results (not real-time) - Laser can affect device thermally and electrically
Micro-particle sensor IR thermal microscopy	+ Measurements can be made on any material + Multiple lenses enable both large and small areas to be imaged/measured + Quasi-real-time measurement + Move/reposition micro-particle sensor + Can use a variety of micro-particle sizes	- Limited micro-particle sizes (3 to 50 μm) - Heat spreading will occur through the area of the micro-particle sensor (smaller sensors, smaller heat spreading) - Comparative measurement (requires images of both unpowered and powered states)
Atomic Force Microscopy (AFM) / Scanning Thermal Microscopy (SThM)	+ Spatial resolution of $<$1 μm + Measurements can be made on any material + Real-time measurement	- Contact method; probe can affect device thermally and electrically - Good contact required between probe and device surface for accurate measurements - Measurements can only be made over small areas
Thermocouple	+ Easily obtained commercially + Real-time measurement	- Contact method; probe can affect device thermally and electrically - Can only make single point measurements - Resolution limited to the probe tip area ($\sim$200 μm)

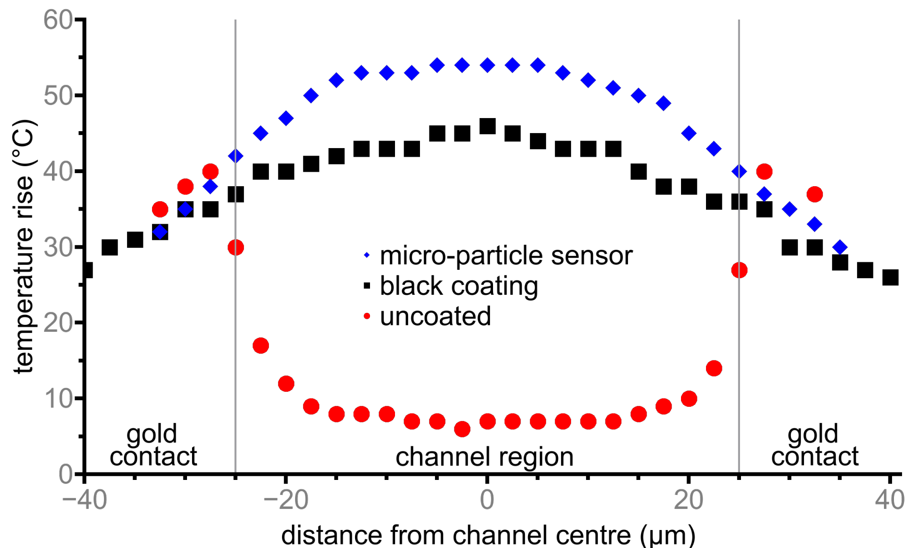

Figure 2.4: *Plot comparing the measured temperature rise of a GaN TLM structure from a conventional (uncoated) IR thermal measurement with measurements using a black paint coating and micro-particle sensors [14].*

2.2 Gunn diodes

J. B. Gunn was the first to observe the Gunn effect. While studying noise properties of GaAs under high electric fields, Gunn observed current oscillations when the electric field exceeded a certain value (35 kV/cm) [16; 17; 18]. This empirical discovery started the development of the Gunn diode. In 1961, Ridley and Watkins [19] proposed an explanation for the negative differential resistance (NDR) in semiconductors by proposing the transferred electron effect, which contained essential details towards an explanation for Gunn's observation. This behaviour is specific to the conduction band structure and electron transport properties in some III-V semiconductors, like gallium arsenide (GaAs) and indium phosphide (InP). In 1964 Kroemer finally explained that the current oscillations and apparent NDR were due to a transferred electron effect [20], which states that the specific sub-band structure found within the conduction band of III-V semiconductors enables electrons to transfer from a low-energy, high-mobility sub-band to a higher-energy, low-mobility sub-band with an increased (applied) electric field, resulting in the NDR. Experiments by Heeks in 1966 [21] substantiated Kroemer's explanation. The explanation by Kroemer and Heeks' experiments have been widely accepted as the reasoning behind the Gunn effect.
Gunn diodes are semiconductor devices that utilise the Gunn effect to provide a microwave source which converts DC (direct current) to RF (radio frequency)

power (figure 2.5). They were originally fabricated as a vertical structure (figure 2.6(a)) but recently planar Gunn diodes have been proposed [22] and fabricated [1] (figure 2.6(b)).

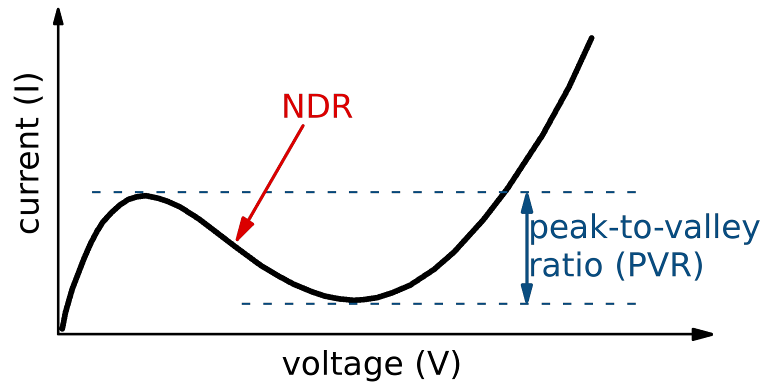

Figure 2.5: *Basic current-voltage (IV) plot for a Gunn diode, showing the NDR region [23].*

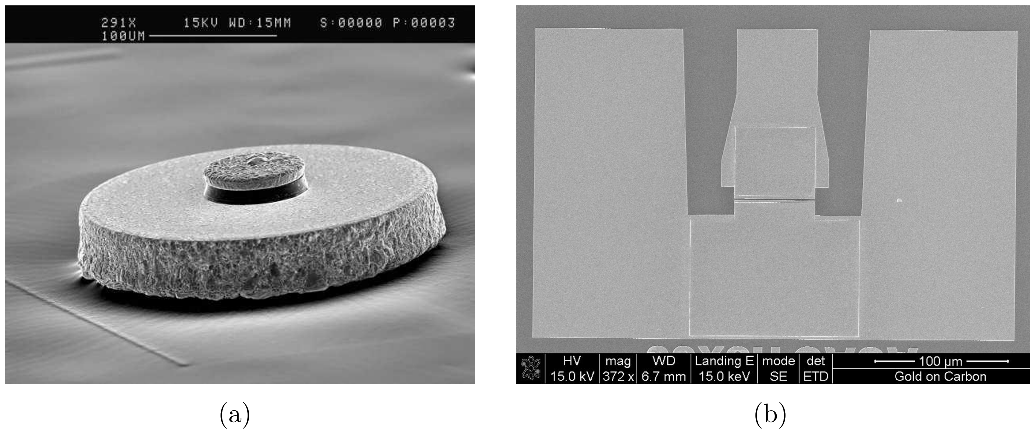

Figure 2.6: *Scanning electron microscope (SEM) images of; (a) a vertical Gunn diode [24], and (b) a planar Gunn diode [2].*

Gunn diodes are fabricated on III-V semiconductors and normally GaAs or InP are used, however other semiconductors can be used if they have the similar band structure. The Gunn diode normally consists of three semiconductor layers, two highly doped contact layers sandwiching a lower doped transit layer (figure 2.7). These layers can be grown using standard deposition techniques, such as vapour phase epitaxial growth (VPE), molecular beam epitaxy (MBE),

and metal organic chemical vapour deposition (MOCVD). The contacts are defined using standard photolithography, for example UV patterning or electron beam lithography (EBL), and etching techniques.

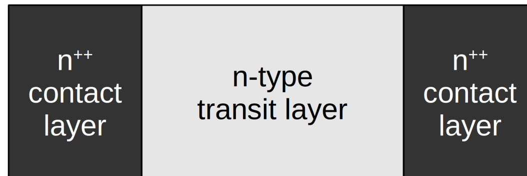

Figure 2.7: *Basic layer structure of a Gunn diode.*

The frequency of the oscillation of a Gunn diode is determined by the time it takes for the formed Gunn domains to travel across the transit layer. The Gunn domain is an oscillating electric field, induced by the NDR of a Gunn diode. The domain is formed at the edge of the cathode contact and will travel through the transit layer to the anode contact, where it will be neutralised. Once the current of the domain is neutralised, another domain will form at the cathode. This constant formation and neutralisation of Gunn domains gives rise to the observed RF oscillation (figure 2.8). Therefore, a short transit layer will result in a small transit time, which translates to a high frequency. In simple Gunn theory, the frequency can be considered inversely proportional to the anode-cathode separation (L_{ac}). This is true for both the vertical and planar Gunn diodes.
Although the planar Gunn was proposed as early as 1972 [22], contacting and lithography techniques were not precise enough to produce operational devices. It took Dunn et al.'s Monte Carlo simulations from 2005 [25] to pave the way for Khalid et al. to fabricate a working planar Gunn diode, which was shown to operate above 100 GHz [1]. There is an interest in the planar Gunn diode as a milli-metric or terahertz source (1×10^{12} to 1×10^{15} Hz).
Vertical Gunn diodes were developed from the mid 1960s and became a very widely used solid-state microwave source for defence and commercial applications. This was until the onset of the development of GaAs metal semiconductor field effect transistors (MESFETs) in planar technology, which naturally led to easier integration into monolithic microwave integrated circuits (MMICs). The microwave performance of the MESFET was also easier to RF characterise and to build computer simulation models (based on the DC & RF data) than for the Gunn diode. Both the above aspects led to a diminished Gunn diode popularity. However, it was further developed for some specialised applications, for example the 77 GHz automatic cruise control system for the automotive industry [26].

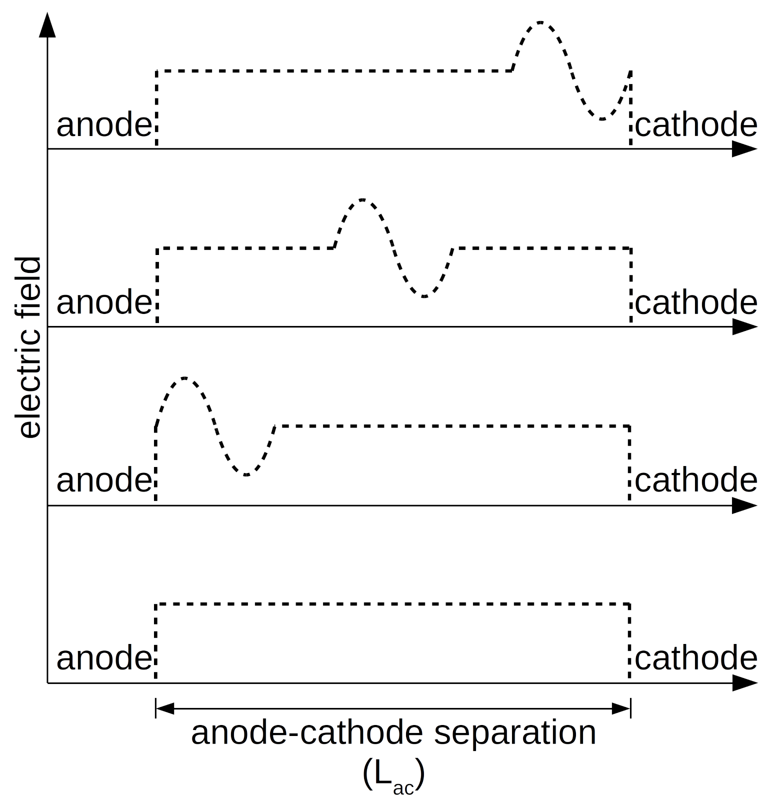

Figure 2.8: *Representation of Gunn domain formation [6].*

2.2.1 Vertical vs. planar Gunn diodes

As briefly described, the Gunn diode can be fabricated as a vertical or planar structure. The direction of the current flow through the diode, with reference to the grown semiconductor interface layers, determines whether it is thought of as a vertical or planar structure. Figure 2.9 shows the two forms of Gunn diode, with the current flowing perpendicular to the transit layer interfaces on the vertical Gunn diode (figure 2.9(a)) and with the current flowing parallel to the transit layer interfaces for the planar Gunn diode (figure 2.9(b)).

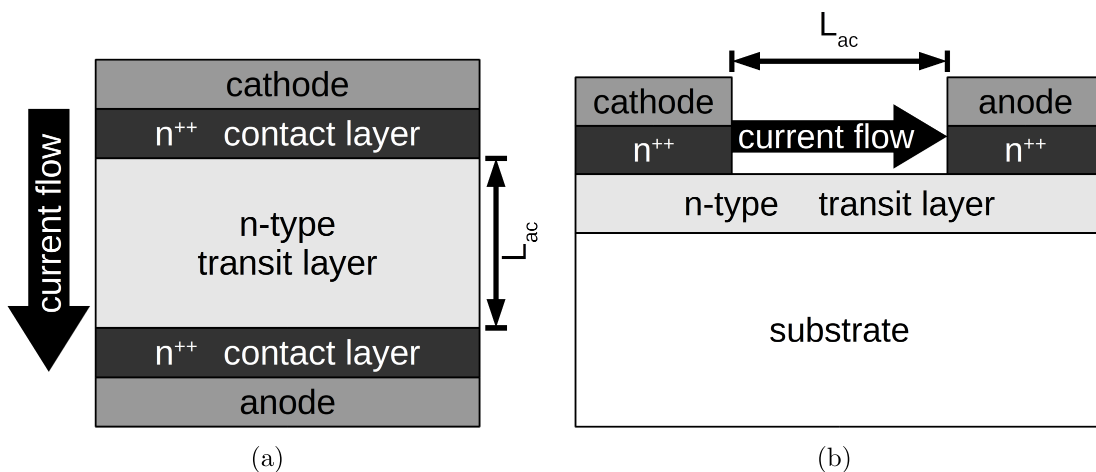

Figure 2.9: *Schematic view of Gunn layers and direction of current flow for (a) a vertical Gunn diode and (b) a planar Gunn diode.*

The practical realisation of the planar Gunn diode in 2007 [1] has paved the way to realise an RF signal source, which unlike the vertical Gunn diode can be easily integrated with MMIC technology and has the potential to operate up to terahertz frequencies [27; 28]. The prime reason for this is that the frequency of oscillation is determined by the anode-cathode contact separation. The planar contact separation is determined by photolithographic techniques and the sub-micron channel distances (required for very high frequency planar Gunn diodes) can now be well-defined using EBL technologies [5; 6; 29; 30; 31]. The contact separation of a vertical Gunn diode (and therefore the operational frequency) is determined by the thickness of the transit layer, which is limited by the layer growth technology and is more difficult to control and more expensive than photolithography. This means for the vertical Gunn diode that all the fabricated diodes from a single wafer will have the same Gunn transit operational frequency. Whereas, for the planar Gunn diode, as the contact geometry determines the operational frequency, one wafer can be used to produce Gunn diodes operating over a range

of frequencies. Planar Gunn diodes are likely to give lower RF output power as well as higher phase noise compared to vertical Gunn diodes [6; 32]. A simple comparison of vertical and planar Gunn diodes is shown in table 2.2.

Table 2.2: *Comparison between vertical and planar Gunn diodes.*

Vertical Gunn diode	**Planar Gunn diode**
Current flows vertically across layers (perpendicular to layer interfaces)	Current flows horizontally along layers (parallel to layer interface)
Only one operational frequency per wafer growth	Multiple operational frequencies can be realised from a single wafer growth
Frequency determined by active layer thickness (from wafer growth)	Frequency determined by the separation between anode and cathode electrodes
Difficult to integrate with MMICs	Easy MMIC integration
RF output power is higher than planar Gunn diodes (350 mW $\approx$ 25 dBm at 35 GHz) [33]	Low RF output power (-4 dBm $\approx$ 0.4 mW at 109 GHz) [2]
Easy and low cost discrete device fabrication	Easy and low cost fabrication and integration with MMICs

The advances in EBL [29; 30; 31] (and therefore planar Gunn diode contact fabrication) now mean that the planar Gunn diode can be fabricated with more precise and uniform contacts. The reason the planar Gunn diode can be easily integrated in MMIC technology is its planar structure matches the coplanar waveguide (CPW) format [6] (figure 2.10). The CPW was first proposed in 1969 by Wen [34]. CPW has become popular with MMIC technology because it has enabled the mounting of lumped elements in both series and parallel configurations on the front face of a substrate. CPW is advantageous to microstrip circuits as the ground contacts are located on either side of a central metallised transmission line, on a dielectric substrate (figure 2.10). While for a microstrip circuit the

ground contact is on the back face of the substrate and holes have to be drilled (known as vias) to make ground connections (for parallel components). The CPW configuration is totally planar, enabling easy connection to active devices such as MESFETs and planar Gunn diodes. The CPW structure of the planar Gunn diode is shown in figure 2.6(b).

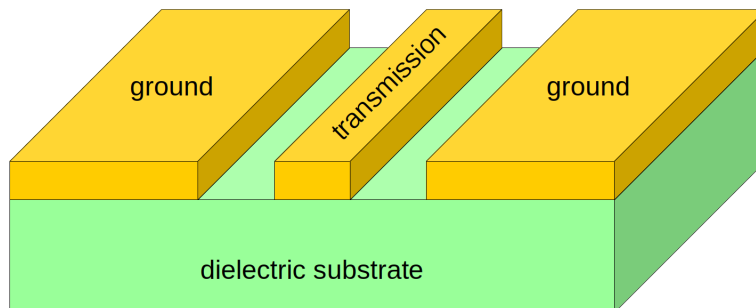

Figure 2.10: *Basic coplanar waveguide structure.*

2.3 Micro-coolers

Electronic devices are required to operate at as low temperature as possible to obtain maximum electrical/RF performance and high reliability. Traditionally, large collections of interconnected electronic devices on a semiconductor wafer have been cooled with stand-alone or fan-assisted heat-sinks (highly thermally conductive metal plates, often with a finned structure to increase the surface area). However, this technology cannot easily be scaled down to accommodate device/chip areas of approximately 0.01 mm^2 and therefore cannot effectively be used at single device level. A semiconductor integrated technology based micro-cooler would substantially improve cooling at single device level.
The need for smaller cooling devices has led to the use of micro-coolers. These devices can use a number of methods to remove excess heat and include; (i) pumping a gas/liquid [35; 36] and (ii) solid-state devices that use an electrical current flow to draw heat from one side of the cooler to the other [37]. Gas/liquid coolers require piping and a micro-pump to move the coolant around the cooling circuit. This requires external connections and equipment, rendering them a bulky and expensive option. Solid-state coolers have no moving parts, and therefore will be less complicated to realise and potentially more reliable. These devices are referred to as Peltier or thermoelectric coolers (TECs) and have shown potential for being scaled down to small area devices [38]. TECs convert an electrical po-

tential difference into a temperature difference (thermoelectric effect) across two device contacts, i.e. the anode and cathode contacts.

2.3.1 Thermoelectric effect

The thermoelectric effect is a relatively new term to describe the conversion of a temperature difference to a potential difference or vice versa. It is a general term used to identify the same fundamental phenomenon described by three effects, which were separately observed in the 19th century:

1. The Seebeck effect,
2. The Peltier effect, and
3. The Thomson effect

Seebeck effect

The Seebeck effect is the conversion of a temperature difference to a potential difference. It was first experimentally observed by Thomas Johann Seebeck in 1821 [39]. In the experiment Seebeck observed the deflection of a compass needle when one junction (in a closed loop) made of two dissimilar metals was heated. The reason for this was the flow of electrical current giving rise to a magnetic field that deflected the compass needle. The amplitude of this deflection was increased as the temperature difference was increased. The Seebeck effect is seen with all materials that can conduct electricity, both metals and semiconductors. Seebeck also tested many materials and organised them into the Seebeck series (very similar to the more familiar thermoelectric series). The Seebeck coefficient (S) gives a direct indication of the magnitude of the potential difference (for a given temperature) between different combinations of materials.

Peltier effect

The Peltier effect is the conversion of a potential difference to a temperature difference. It was first experimentally observed by Jean Charles Peltier in 1833 [40]. Peltier observed a temperature difference between metal junctions (made by a closed loop of two dissimilar metals) when a current was passed through them. Changing the polarity of the current applied to the loop would switch which junction was heated and which was cooled. At the time no correlation between Peltier's and Seebeck's findings was made, and Peltier was unable to explain the

fundamental reason for the effect he observed. In 1838, Heinrich Lenz experimentally demonstrated Peltier's findings by placing a drop of water onto one of these junctions, he applied a current to freeze the drop of water, and then reversed the current to melt the ice.

Thomson effect

The Thomson effect describes the findings made by William Thomson (later to become Lord Kelvin) in 1851. Thomson noted the correlation between the Seebeck and Peltier effects and paved the way to increase the power generation from a closed loop of two dissimilar metals. Single thermoelectric elements produce very little power (of the order of μW), while modern thermoelectric generators use multiple sets of junctions to increase the output power (to W).

2.3.2 Thermoelectric cooling

The same fundamental phenomenon can be applied to all three effects (Seebeck, Peltier, and Thomson), therefore a general term has now been coined: the thermoelectric effect. The use of the thermoelectric effect for cooling purposes, using electrons (e^-) as the charge carrier, is described in detail. The description equally applies to holes (h^+) in a semiconductor, but to simplify the description only electrons will be considered here.
The flow of heat from one junction (X) to another (Y) is described and focuses on the cooling of junction X. However, if the current direction is reversed heating will be observed at junction X instead. The ability to adjust the current magnitude also enables a temperature to be maintained at junction X. Reversing the process, by heating junction Y, enables the same system to be used for power generation, i.e. converting a temperature difference (between junctions X and Y) to a potential difference. It should be noted that thermoelectric cooling will always transfer heat between two junctions, this will be discussed further in section 2.3.3.
In the case of a simple TEC, made of two dissimilar conductive materials (A and B) in a closed loop (figure 2.11). Heat is transferred from one junction (X) to the other (Y), as an electron current (I) flows around the loop. If material A has a lower energy level for its conduction band than material B, then as the electron current approaches junction X, it will reach a barrier between the low energy conduction band of material A and the higher energy conduction band of material B. Some electrons will have less energy than required to flow across the barrier into material B, hence, these electrons absorb heat energy from junction

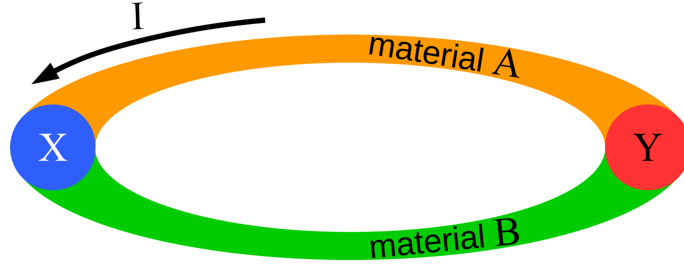

Figure 2.11: *Closed loop made of two dissimilar materials (A and B) with electron current flow (I).*

X to cross the barrier into material B. As these hot electrons then exit junction X and flow through material B, they take this heat energy with them. Upon reaching junction Y the electrons will face a further energy barrier. However, this barrier will involve an energy drop, as less energy is required by material A's conduction band. Therefore, the electrons can pass the extra energy into the ambient environment of junction Y, thereby raising its temperature. This process leads to a temperature reduction at junction X and a temperature rise at junction Y. The temperature difference (ΔT) is observed between junction Y (T_h) and X (T_c), equation (2.4). A constant current (I) maintains the temperature difference, however the existence of this temperature difference will cause a reverse flow of electrons trying to reach a thermal equilibrium. This attempt to reach a thermal equilibrium will cause electrons to absorb energy from junction Y and flow towards the colder junction X. This flow of electrons is a flow-back current, which restricts ΔT and is taken into account by including the thermal impedance (Θ) of the micro-cooler. The higher the thermal impedance, the higher ΔT. Equation (2.5) describes this process [41; 42; 43], where SIT is the cooling power of the TEC, Θ determines the flow-back heat, and RI^2 is the Joule heating (or self-heating) power inside the TEC.

$$\Delta T = T_h - T_c \tag{2.4}$$

$$\Delta T = \Theta(SIT - RI^2) \tag{2.5}$$

Where ΔT is the temperature difference across the TEC (K), T_h is the TEC's hot-side temperature (K), T_c is the TEC's cold-side temperature (K), Θ is the TEC's thermal impedance (K/W), S is the Seebeck coefficient (V/K), I is the current flow within the TEC (A), T is the ambient temperature (K), and R is the electrical resistance of the TEC (Ω).

Single thermoelectric elements, as in figure 2.11, have a very low efficiency, they require very high input powers to produce a large temperature differences. Metals

will only give small temperature differences as the Seebeck coefficient for a metal is small, in the range of -70 to $+50$ μV/K. Whereas the Seebeck coefficient is larger for doped semiconductors, in the range of $\pm$2,000 μV/K. The Seebeck coefficient (S) used in equation (2.5) is the difference in Seebeck coefficient of the two materials used to make a thermoelectric element, therefore if two materials have a large difference in Seebeck coefficients, it will give rise to a high ΔT. For this reason, semiconductor materials have been used to form the junctions with metals and have been found to be more efficient than junctions of two dissimilar metals, due to the large difference in Seebeck coefficients. If material B (figure 2.11) is a semiconductor, it will have a higher energy level conduction band than a metal material A. Therefore, any set of metal-semiconductor-metal junctions have the same thermoelectric process as described above (where the electrons travel from material A to material B and back into material A), figure 2.12, however a higher ΔT is obtained.

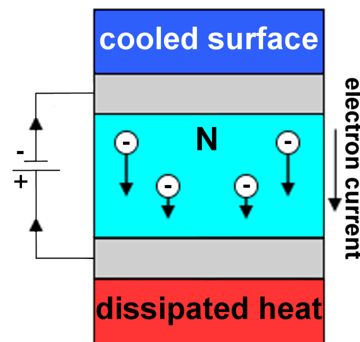

Figure 2.12: *Basic thermoelectric cooler (TEC), using an n-type semiconductor and two junctions (with metals), where heat is transferred with electron current flow.*

Semiconductors can be n-type doped (excess of electrons, e^-) or p-type doped (excess of holes, h^+) to utilise both e^- and h^+ as the majority charge carriers. With n-type semiconductors (e^- is the majority charge carrier) thermoelectric heat flow is with electron current, and with p-type semiconductors (h^+ is the majority charge carrier) thermoelectric heat flow is in the opposite direction to electron current. Therefore, pairing p-type and n-type semiconductors (with metal interconnects) enables coolers to be designed with multiple junctions. Figure 2.13 shows a four junction TEC increasing the magnitude of ΔT. The design allows the cooler to be electrically in series but thermally in parallel. As the majority charge carriers in the p-type semiconductor are holes (h^+), the transferred temperature flows against the electron current. Therefore, in both semiconductors the heat is flowing from the top to the bottom of the cooler (figure 2.13).

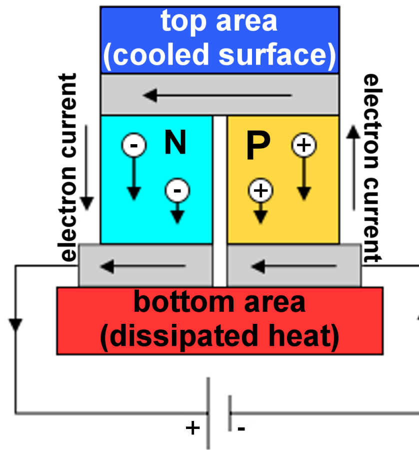

Figure 2.13: *Basic semiconductor thermoelectric cooler (TEC), using both n-type and p-type materials [44], showing both electron current flow around the circuit and hot charge carrier flow.*

Increasing the number of semiconductor elements within a TEC increases the thermal output power. The majority of commercially available TECs (often referred to as Peltier coolers) have the same basic structure (figure 2.13). The PN pairs are connected electrically in series and thermally in parallel using the metal interconnections (figure 2.14). Once again, heat is carried from the top to the bottom of every semiconductor element within the TEC. Thermally conductive ceramic plates are used on both the top and bottom of the TEC, sandwiching all the semiconductor elements and allowing the heat in the top and bottom ceramic plates to spread across the whole of the TEC's top and bottom areas (figure 2.14). Using multiple PN semiconductor pairs enables more efficient TECs to be manufactured, however, more PN pairs will result in a larger overall size and higher TEC operating current.

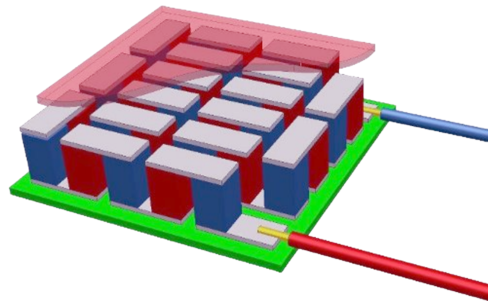

Figure 2.14: *Electrical interconnections between many PN semiconductor pairs in a TEC, so they are electrically in series but thermally in parallel [45].*

If large values of ΔT are required, then multi-stage, paralleled, TECs can be used. A three stage TEC is shown in figure 2.15, where the total ΔT (ΔT_{tot}) is the summation of ΔT from the 1st (ΔT_1), 2nd (ΔT_2), and 3rd (ΔT_3) stages, equation (2.6).

$$\Delta T_{tot} = \Delta T_1 + \Delta T_2 + \Delta T_3 \tag{2.6}$$

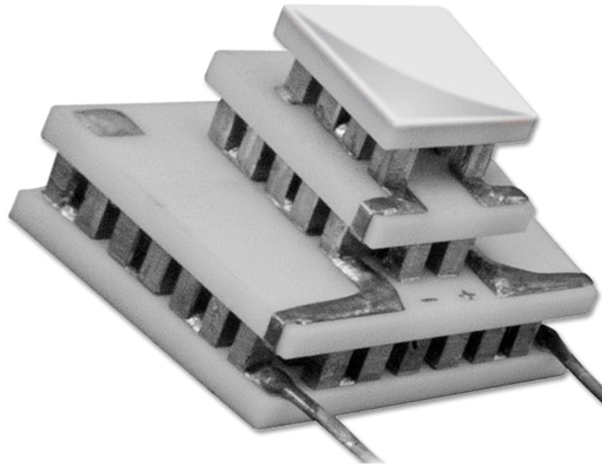

Figure 2.15: *Multi-stage TEC [46].*

Note that the T_h of the 1st stage is the same as the T_c of the 2nd stage, and the T_h of the 2nd stage is the same as the T_c of the 3rd stage (where the first stage is on the top and the 3rd stage is on the bottom of the TEC). The structures are in parallel, but the thermal parameters are in series. Therefore, ΔT_{tot} is the temperature difference between T_h of the 3rd stage and T_c of the 1st stage. This style of TEC is commercially available, however, the size of these TECs are large, with typical device widths ranging from about 5 to 60 mm, with single stage coolers having a thickness of about 3 to 5 mm.

Although these coolers can be made smaller (approximately 5×5×3 mm) and have good potential for use with electrical devices (that range from a few to tens of millimetres) or for cooling areas of larger scale circuits they would be too bulky for cooling individual devices. Especially when looking at cooling high frequency solid-state sources for milli-metric and terahertz operation. There would be significant benefits if a micron-scale micro-cooler could be developed and directly integrated with an active device, for example the planar Gunn diode. This approach requires a cooler of similar area to the planar Gunn diode and will eliminate the adhesive layer (required to bond current coolers with active devices), which would act as a thermal barrier between the planar Gunn diode

and micro-cooler. The research work would be novel and offer real advantages to improving the thermal and electrical performance of the planar Gunn diode.

2.3.3 Miniaturisation of coolers

There have been numerous publications regarding the development and potential uses for micro-coolers [41; 47; 48]. A variety of materials have been reported, with the best recorded performance from silicon-germanium [43; 49; 50] and bismuth-telluride devices [38]. However, these could not be integrated (at a wafer level) with the GaAs based planar Gunn diode. The need for integrated coolers that can be manufactured from bulk semiconductors has led to suggestions that although the thermoelectric effect occurs within these very small scale devices, most of the cooling may be because of the so called thermionic effect.

Thermionic effect

Research papers have been published [51; 52; 53] describing the thermionic effect as the main cooling process in semiconductor micro-coolers. However, the effect is very similar to the thermoelectric effect [54; 55].
The term thermionic cooling is applied to micro-coolers where the electron flow is said to be ballistic (no electron scattering is occurring) through the barrier. This occurs when the barrier lengths are short, tens of nanometres, and so similar to the mean-free path (the average distance between electron collisions). Therefore, only the most energetic (hot) electrons freely travel from one side of the junction to the other. Hence, when a bias is applied to the micro-cooler, the electron flow crosses the barrier and the hot electrons are moved from one side of the junction to the other, resulting in cooling the side of the junction from which the hot electrons flow. As electrons continue to flow through the circuit they loose energy, and so cooler electrons flow back (to maintain a neutral total charge) while creating a temperature gradient. This is unlike thermoelectric cooling, where the barrier lengths are usually several hundreds of nanometres in length and electrons flow by diffusion across the junction.
Thermoelectric cooling provides a temperature difference between the junctions of a closed loop (ΔT), while thermionic cooling provides a temperature difference between either side of a junction (δT). Thermionic emission has the highest efficiency when the barrier thickness (d_B) is smaller than the mean-free path of the electrons, as the electrons are then able to pass through the barrier without scattering. As the temperature difference (δT) across the barrier is very small, to

increase the temperature difference, a number of barriers can be grown in series forming what is known as a superlattice.

Superlattice

A superlattice is a man-made material that is constructed from periodic layers of two semiconductor materials (figure 2.16). The materials have different electrical and thermal properties (from each other) and their combination forms a

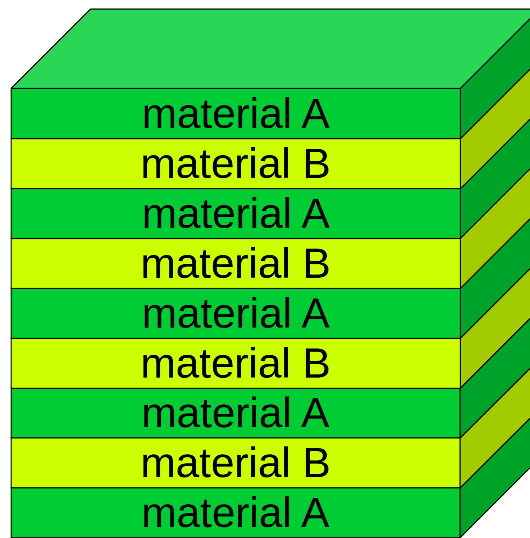

Figure 2.16: *Basic superlattice structure.*

superlattice with uniquely different electrical and thermal properties from either of the materials it is fabricated from. Changing the layer thicknesses allows for the properties of the superlattice to be tuned appropriately, for example; giving a high electrical conductivity with a low thermal conductivity [41; 56; 57]. The thermal conductivity of a superlattice can be made approximately 10 times smaller than that of the thermal conductivity of the individual materials making up the superlattice [58]. This approach enables superlattice materials to be fabricated with an electrically induced temperature difference across them, but with a low thermal conductivity (κ), which will inhibit the natural flow-back of heat. Many authors have reported on thermionic superlattice structured micro-coolers [47; 59; 60; 61; 62].

2.3.4 Integration

Micro-coolers are commercially available and can be used in thermal management of electronic circuits by bonding the electronic circuit to the cold plate of the cooler. However, this is not the most efficient arrangement as it will cool the whole circuit rather than a specific device within the circuit. The research work in this thesis concentrates on the research/development of a micro-cooler, which is directly integrated to the active device. The active device chosen will be the planar Gunn diode, as the power density produced by these devices is many kW/cm^2.This research work, to the author's knowledge, is novel as there has been no published work where an electronic device has been directly integrated with a micro-cooler within the fabrication process. If successful the research could lead to the direct integration of micro-coolers to other devices, for example high electron mobility transistors (HEMTs) and monolithic microwave integrated circuits (MMICs).

The research work was carried out in collaboration with the University of Glasgow, University of Bristol, and University of Aberdeen as part of a collaborative EPSRC (Engineering and Physical Sciences Research Council) grant. The fabrication work of both the planar Gunn diode and micro-cooler structures were carried out by the University of Glasgow.

Chapter 3

Infra-red thermal measurement

Infra-red (IR) thermal microscopy techniques have been developed at De Montfort University to thermally profile electronic devices. Benefits of this measurement technique include; (i) a non-contact measurement, (ii) good thermal resolution ($\sim$3 μm), and (iii) a quasi-real-time measurement. Further detail of the benefits of IR thermal microscopy were given in section 2.1.
The IR microscope at De Montfort University is an InfraScope II manufactured by QFI (Quantum Focus Instruments, USA). Figure 3.1 shows an image of the microscope with supporting equipment and computers, which have been identified by number.
The numbered items in figure 3.1 are as follows:

1. Anti-vibration table.

2. DC/RF probe table.

3. Adjustable xy stage mount, with controls to adjust the stage position alone the x and y-axes, as well as 90° of stage rotation (along this plane).

4. Temperature controlled stage (for heating the DUT). The heating is provided by a thermoelectric heater. Operating temperatures between 25 and 130 °C (±0.5 °C) can be set. Additionally, a thermocouple has been embedded into the aluminium heated stage, this is used to measure the operating temperature (±0.1 °C).

5. Four Wentworth Laboratories PVX400 probes. Each probe has a magnetic base to hold it in position, while having controls to adjust the probe tip along the x, y, and z-axes. For standard DC probing, four probes with DC tips are used, however two probes can be fitted with RF probe tips.

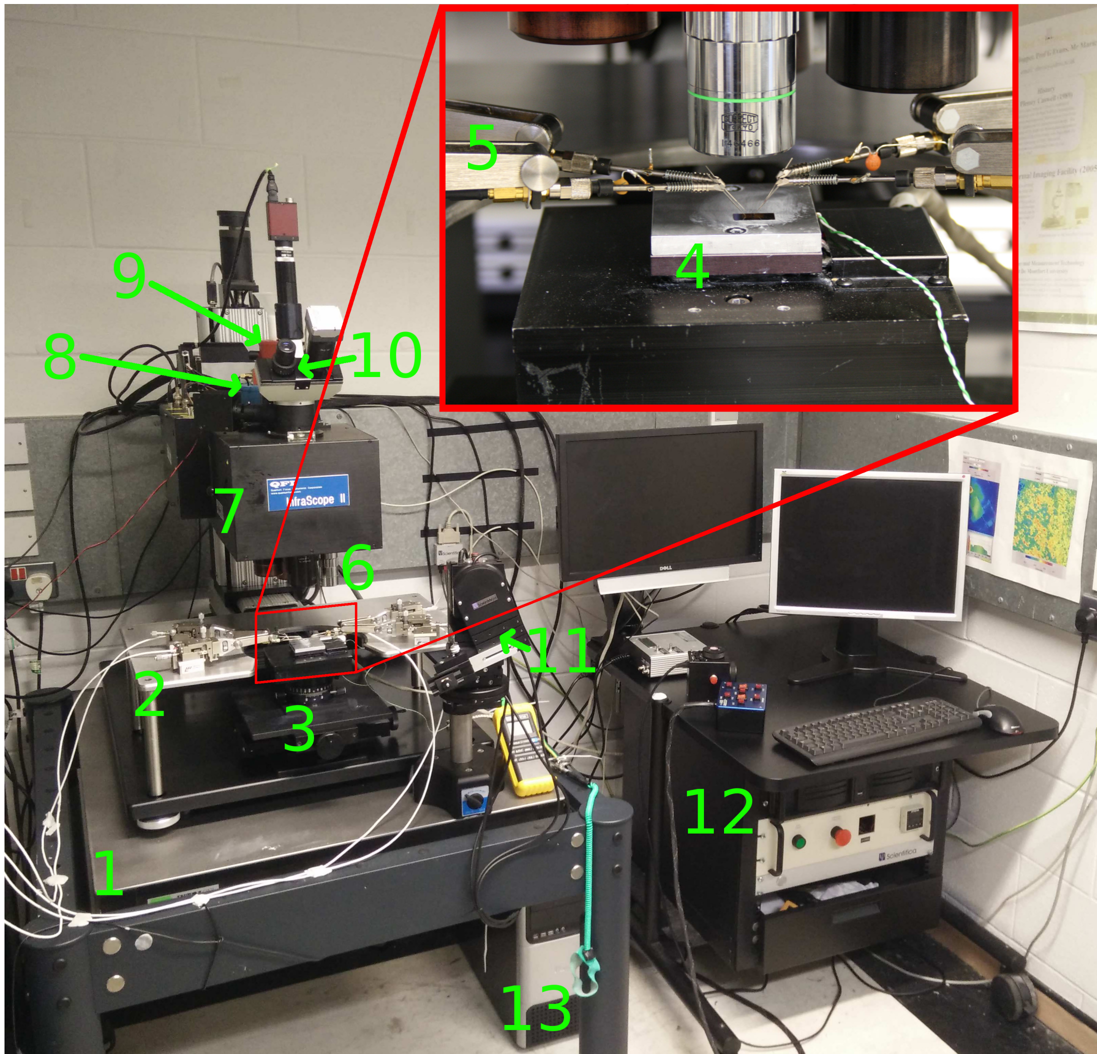

Figure 3.1: *De Montfort University's IR microscope set-up using an InfraScope II from QFI (details of numbered items to be found in the description).*

6. Rotational lens selector with three IR lenses ($\times1$, $\times5$, and $\times25$ objectives) and one $\times25$ optical lens installed. The IR objectives will provide a field of view of 10$\times$10 mm, 2.3$\times$2.3 mm, and 464$\times$464 μm and a thermal spatial resolution of $\sim$50 μm, $\sim$10 μm, and $\sim$3 μm respectively.
7. Adjustable microscope head. 3-axes of motion, operated by three separate linear motors, controlled by either a controller box or QFI's ThermalMap software installed on the master PC. The head also includes two mirrors, both with two positions of operation. The first mirror switches the lenses view between the two IR detectors and the optical turret, and the second mirror selects either the imaging IR detector array or the transient IR single element detector, to record thermal changes with time.
8. Imaging IR detector (containing a 512$\times$512 pixel array).
9. Transient IR detector (containing a single detector element feeding a high gain bandwidth amplifier).
10. The optical turret, which contains two optical cameras. The first optical camera is a Moticam 2300 from Motic, with their commercially available imaging software for quick imaging on the same PC operating the QFI software and microscope. The second optical camera is a Stingray from Allied Vision Technologies with bespoke software (developed at De Montfort University), which has been designed to aid the positioning of micro-particle sensors (for advanced IR thermal measurements). The second camera is operated from a dedicated PC.
11. PatchStar micro-manipulator from Scientifica. This is used for positioning the carbon micro-particle sensors for the advanced IR thermal measurement technique.
12. PC desk with integrated rack with the following equipment installed:
    - The master PC supplied by QFI, containing all of their software for controlling the InfraScope II and making array and transient IR thermal measurements. The Motic's imaging and Scientifica's micro-manipulator software have also been installed on this PC.
    - QFI's power controller (with manual force-off safety switch). This supplies all the required AC and/or DC power and sends all requests to the InfraScope II (based on the request sent from the master PC). This includes control for the linear motors to position the microscope head, as well as the temperature controlled stage.
    - Scientifica's power controller for the micro-manipulator.

13. A dedicated PC for operating Allied Vision Technologies' camera and using De Montfort University's imaging software for micro-particle positioning.

3.1 Operation of the IR microscope

The following needs to be taken into account when using the IR microscope; as the objective magnification increases, the field of view reduces, as does the distance between the objective lens and the device surface. Therefore, the positioning of the lens is critical to keep the device surface in focus. For example, when using the $\times 25$ lens, small vertical changes (± 1 μm) will take the images out of focus, whereas, the $\times 1$ lens (which is further away in distance from the device surface) is less susceptible to small vertical changes. The microscope has been mounted on an anti-vibration table to minimise device movement due to environmental parameters (low-frequency sound, high levels of foot traffic, and/or slamming of doors).
To overcome some limitations faced by IR thermal microscopy (discussed in section 2.1.3), an IR thermal measurement technique using a carbon micro-particle sensor has been developed previously at De Montfort University [15]. The micro-particle sensor has been fabricated from materials that give a consistently high surface emissivity, allowing thermal measurements to be made on any material surface on which the sensor has been positioned [14; 15].

3.2 Micro-particle sensor

IR thermal point measurements have been developed at De Montfort University, using a carbon micro-particle sensor [14; 15]. The micro-particle is fabricated from a high emissivity material with a range of diameters. De Montfort University has used micro-particles in the range of 2 to 50 μm, however, most measurements use particles with diameters between 3 and 20 μm. The emissivity of these micro-particle sensors have been measured and used to determine the temperature of the surface with which it is in isothermal contact. As the micro-particle sensor is in isothermal contact with the device, a thermal equilibrium will be reached between the particle and the device surface. The small scale of the micro-particle means that the heat drawn away from the device is negligible and equilibrium can be reached quickly (if a large probe with a larger thermal mass was used then significant heat will be drawn away from the device and thermal equilibrium will take longer to be reached). The temperature of the micro-particle sensor can be

measured by recording the emitted radiance, which has already been calibrated against a blackbody as shown in figure 3.2. As the micro-particle sensor is used for measurements where accurate point measurements are required, most of these measurements are made using the $\times 25$ IR objective and a 2-temperature emissivity correction. Micro-particle sensors as small as 3 μm in diameter are used for thermal measurements. This diameter is used as it matches the spatial resolution of the QFI InfraScope II (when using the $\times 25$ objective lens).

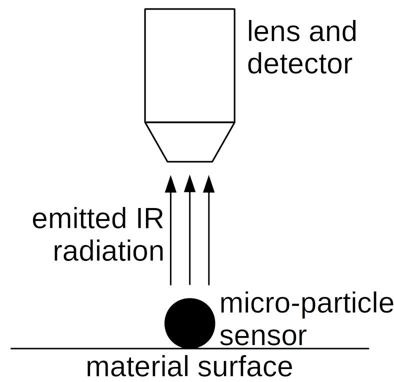

Figure 3.2: *Emitted IR radiation from a micro-particle sensor.*

The micro-particle sensor can be placed on any material (metal or semiconductor) and on any structure that is at least the size of the micro-particle diameter. Micro-particles once placed can be manipulated and repositioned as required, however this is ongoing research. The micro-particle can also be removed from a device without causing damage to the device.
The micro-particle sensors in this research were spherical in shape, this was beneficial for a number of reasons:

- The shape is well-balanced and so, once positioned, the particle is stable.
- It provides a point contact with the DUT. This minimises the van der Waals forces holding the particle in place (if these were too great then particle repositioning may become difficult) and it may enable smaller point measurement areas to be analysed (this would require additional research).

For example, conical particles could be used to enable a point thermal measurement, however these are unlikely to be stable without a support structure, while cuboid particles would be stable, but would have a larger contacting area with the DUT.

3.3 Micro-particle emissivity

The surface emissivity of a micro-particle sensor is measured using the 2-temperature emissivity correction technique described in chapter 2. The change in measured radiance from the micro-particle sensor at two known operating temperatures is compared with the change in the radiance of a blackbody at the same two temperatures. The QFI InfraScope II takes the blackbody radiance values from a stored blackbody calibration (recalibrated on an annual basis).
This is a difficult measurement for a number of reasons:

- There will be background radiation from the surface of the material that the micro-particle has been placed on, this will be discussed later in this section.
- Any small movement that puts the surface of the micro-particle out of focus.
- To measure the surface emissivity of the micro-particle the 2-temperature emissivity correction technique requires the operating temperatures of the micro-particle to be significantly different. The large difference in operating temperatures will lead to small stage movements due to thermal expansion. This can be corrected for by repositioning the microscope head to realign the image at the two operating temperatures.

Once the surface emissivity of the micro-particle has been measured, the InfraScope can be used to measure the radiance emitted by the micro-particle and the temperature of the micro-particle can be calculated.

3.4 Micro-particle characterisation

The QFI InfraScope II observes IR radiation with wavelengths between 2.5 and 6 μm (figure 2.1) and therefore has a minimum spatial resolution limit of $\sim$3 μm (the diffraction limit of the IR radiation wavelength), which is achieved with the $\times$25 objective lens. Therefore, it is difficult to obtain an accurate temperature measurement for features smaller than 3 μm. The Sparrow criteria (3.1) can be used to define the height of the objective lens above the sample [14].

$$\mathrm{D} = \frac{0.47 \cdot \lambda}{\mathrm{NA}} \tag{3.1}$$

Where D is the separation distance between the focal plane and objective lens (m), λ is the wavelength (m), and NA is the numerical aperture.

A set of experiments were carried out to check whether the micro-particle sensor will enhance or degrade the thermal spatial resolution of the InfraScope II and to look at the effect background radiation has on the measurement. This experiment involved looking at different diameter micro-particle sensors (between 2 and 8 μm) to determine the effect the particle diameter has on the measured temperature. The results were obtained by heating the micro-particles to different operating temperatures (from approximately 50 to 130 °C) using the InfraScope's thermoelectric temperature controlled stage. To include the effect of the background surface emissivity, the micro-particle sensors were placed on both low (gold, ȩ $\approx$ 0.1) and medium (aluminium stage, ȩ $\approx$ 0.3) surface emissivity backgrounds. The results are summarised in tables 3.1 & 3.2. The tables give an indication of the error in the temperature measurement when comparing the measured IR micro-particle sensor temperature with the controlled stage (operating) temperature. Each measurement within the tables is colour coded to show whether a measured temperature was colder (blue cell), hotter (red cell), or within a $\pm$0.5 °C margin of error (green cell) of the set operating temperature (stage temperature).

Table 3.1: *Measurement accuracy for micro-particle diameters (between 2 and 8 μm) over a number of stage temperatures on a gold background (ȩ $\approx$ 0.1).*

Diameter (μm) $\pm$0.2 / Stage temp (°C) $\pm$0.8	**2.0**	**3.0**	**3.5**	**3.6**	**3.6**	**4.9**	**5.8**	**6.3**	**7.7**
50	-4.1	0.0	-2.4	-5.3	-0.7	0.0	-0.6	-0.8	-0.4
60	-0.1	-2.2	-0.8	-0.6	-0.5	-0.1	$+0.8$	$+0.6$	$+0.2$
70	-2.0	-1.1	-1.7	-1.7	-3.4	-1.8	-0.6	-0.7	-0.5
80	-0.5	-0.8	-1.1	$+0.1$	-0.1	-0.2	-0.6	0.0	-0.3
90	-0.3	$+0.2$	$+0.4$	-1.2	$+0.3$	-0.1	-0.3	-0.2	-0.4
100	-0.2	-0.6	-0.4	-0.5	-0.8	-0.4	-0.4	-0.2	$+0.3$
110	-0.2	-0.2	-0.7	-0.3	0.0	-0.4	-0.3	$+0.1$	$+0.5$
120	-1.5	-0.8	-0.7	-0.2	-0.3	-1.1	-0.7	-0.3	-0.3
130	0.0	$+0.2$	$+0.4$	$+0.5$	-0.1	0.0	0.0	-0.1	$+0.3$

The experiment showed the particle diameter had only a small effect on the accuracy of the measured temperature, when compared directly with the stage temperature. From both tables it is clear that the stage temperature is the most important parameter, the lower the stage temperature then the larger the error. At elevated temperatures materials will emit higher levels of IR radiance, making the level of the background radiance less important. However, as the stage

temperature is reduced towards room temperature then the amount of emitted IR radiance is reduced, bringing it closer to the background radiance and so increasing the amount of observed noise within the measurement.

Table 3.2: *Measurement accuracy for micro-particle diameters (between 2 and 8 μm) over a number of stage temperatures on an aluminium background ($\varepsilon \approx 0.3$).*

Stage temp (°C) ±0.6 \ Diameter (μm) ±0.2	**2.0**	**3.0**	**3.5**	**3.6**	**3.6**	**4.9**	**5.8**	**6.3**	**7.7**
50	−0.7	−2.7	−1.8	−2.5	−1.9	−2.9	−2.1	−0.3	+0.3
60	−0.9	−1.7	−2.6	−2.3	−2.1	−2.0	−1.5	−0.6	+0.4
70	+0.9	−0.8	+0.1	−0.9	−0.4	−0.4	−0.8	+0.5	+1.0
80	+0.1	−0.7	−0.4	−0.6	−0.5	−0.6	−0.3	0.0	+0.4
90	+0.2	−0.3	0.0	+0.2	−0.1	−0.6	−0.2	+0.5	+0.7
100	+1.9	+0.1	+0.2	−0.7	+0.2	+0.2	0.0	+0.7	+0.7
110	+0.9	−0.1	+0.7	−0.1	+0.1	0.0	+0.1	+0.5	+0.6
120	+0.5	−0.1	−0.3	−0.3	+0.1	0.0	−0.2	+0.4	+0.4
130	+0.2	−1.7	−0.7	−0.2	−0.5	−0.8	−0.5	0.0	+0.2

It is interesting to note that in table 3.1 (with the very low surface emissivity background material), at the highest stage temperature, there is little effect on the temperature measurement due to the micro-particle diameter. However, as the stage temperature decreases the smaller particles appear to give a less accurate measurement when compared to the larger diameter particles. This behaviour becomes less noticeable when the surface emissivity of the background material is slightly higher (as in table 3.2), the error looking to be less dependent on either particle diameter or stage temperature. This is an important observation when calibrating the micro-particle sensors (section 3.3).
An explanation for the different behaviours in the temperature results between the two tables (3.1 & 3.2) is thought to be due to the different background emissivities. As the IR microscope system tries to produce a smooth image by comparing and averaging the measured value of each pixel with its neighbouring pixels, the radiance from an area greater than 9 μm^2 (approximately 81 μm^2, as radiance from 9 pixels is considered, rather than one) will have some effect on the temperature measured at the micro-particle position. Therefore, the level of background IR radiance around the micro-particle will affect the measured temperature. Very low emissivity materials (like the gold background from table 3.1) will emit a very small amount of background IR radiance, therefore the radiance of

the micro-particle sensor will be far greater than the background radiance, which can then be neglected. Higher emissivity background materials will emit more background IR radiance and will have a greater effect on the recorded radiance from the micro-particle giving rise to a larger error in the measured temperature. Figure 3.3 shows that micro-particles with a diameter greater than 10 μm have similar radiance levels (0.4 to 0.5 mW/sr·cm^2), for a given ambient temperature. However, once the particle diameter is less than 10 μm the radiance starts to decrease as the radiation is being detected over an area larger than the particle diameter and therefore the amount of background radiance becomes increasingly important.

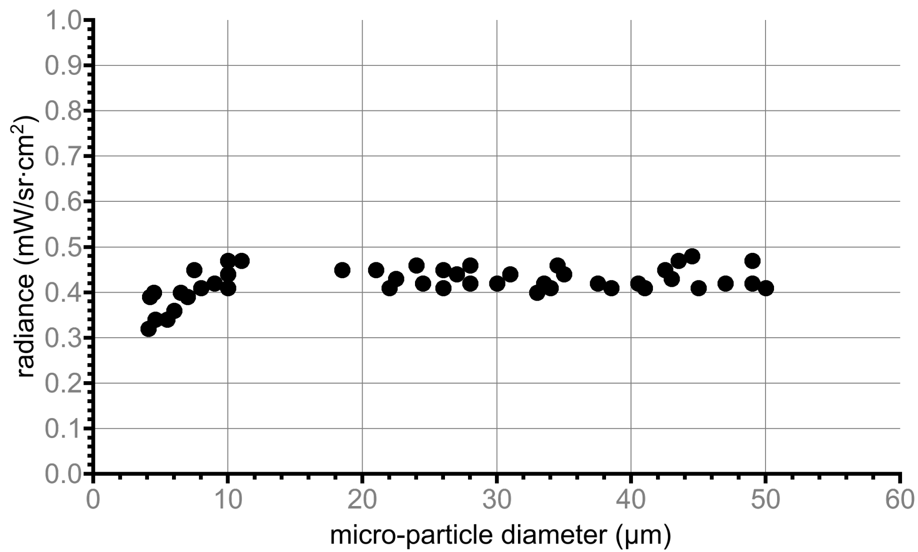

Figure 3.3: *Plot comparing the level of IR radiation detected (radiance) as a function of the diameter of the micro-particle sensor.*

3.5 Micro-particle measurement techniques

The micro-particle sensors can be used in a number of different ways to make surface temperature measurements. The easiest method is to scatter a collection of micro-particles (with an appropriate range of diameters) over the whole surface of the DUT. This method allows for a quick thermal profile to be built-up, however the micro-particle positions are random and so of little use for detailed measurements at a specific location, for example at a hot-spot. However, the method will give detailed thermal profiles across devices with well behaved thermal characteristics. An example is a micro-heater [63].

The preferred use of the micro-particle sensor approach is to use a calibrated single micro-particle placed on the location of a hot-spot. The hot-spot can first be identified using the conventional IR thermal measurement. The micro-particle can then be used to obtain a more accurate peak surface temperature, particularly if the device being measured is fabricated on a semiconductor material where the surface emissivity can not be determined accurately. This method ideally requires an exact positioning technology, work has been carried out using Scientifica's PatchStar precision micro-manipulator [15]. This will be further described in section 3.6.
The micro-particle sensors used in this work are carbon-based particles, purchased from commercial suppliers. The particles are supplied as a powder containing a variety of particle diameters, as already discussed. Two diameter ranges are used at De Montfort University; small scale particles (2 to 12 μm) and larger scale particles (20 to 50 μm).

3.6 Micro-particle manipulation

A dedicated micro-manipulator from Scientifica (figure 3.4) has been fitted to the QFI InfraScope II (figure 3.1) for the placement and manipulation of micro-particle sensors. The author believes this is an innovative combination of the two instruments.

Figure 3.4: *Scientifica micro-manipulator [64].*

A process for locating and manipulating the micro-particles has been developed within this research work and described below.

The micro-particle sensors are held in place, both on the probe tip of the Scientifica manipulator and on the surface of the material to be thermally characterised, by electrostatic and van der Waals forces [65]. The Scientifica manipulator uses very fine probe tips, ∼15 μm in diameter (figure 3.5), and these can be used to manipulate micro-particle sensors along 2-axes (x and y). The Scientifica

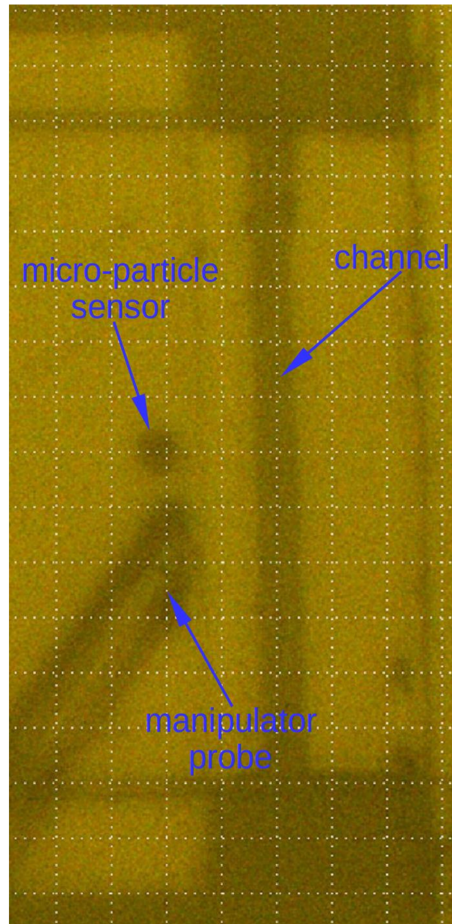

Figure 3.5: *Optical image of micro-particle sensor and manipulator probe.*

manipulator was used to position the micro-particle anywhere on the surface of the material for thermal characterisation. The control of the manipulator was carried out using Scientifica's dedicated controller (figure 3.6(a)). Scientifica's control software (LinLab) enables positioning of the micro-manipulator probe to the nearest micrometer (figure 3.6(b)). LinLab also enables accurate distance measurement from one probe position to the next. However, the software does not take into account the actual position of the micro-particle, as it may move slightly after positioning on the surface of the device to be thermally characterised. Also, if the probe tip is forced to bend slightly, by an artefact on the

device surface, the software will still continue to measure the position and movement of the probe, rather than the micro-particle. Therefore, a technique was required to measure both position and movement of the micro-particle sensor on the surface of a device, which will have surface topology.

(a) (b)

Figure 3.6: *(a) Scientifica's micro-manipulator controller and (b) Scientifica's LinLab software [64].*

The measurement technique developed in this research project consisted of an optical grid, which could be superimposed onto a still frame of the surface of the device to be measured. The method is only applicable to device surfaces where surface topology and/or contacts can be clearly identified by the optical microscope system as a surface feature on the device is needed as a measurement reference point.

3.6.1 Optical grid for particle manipulation

The optical grid (figure 3.7) is a static optical overlay, which can be positioned on an image of the surface of the device to be measured. The dimensions of the grid matrix can be changed to enable different diameter micro-particles to fit inside a grid window. In essence the positioning of the micro-particle can be undertaken by moving the micro-particle from one grid window to the next. The position of the micro-particle can be determined by knowing the dimensions of the grid matrix and placing the side of the grid against a known and measurable point on the surface of the device. For example the edge of a device contact.
For the particular set-up at De Montfort University the grid was calibrated so that a given number of pixels on the optical video feed was equal to a known distance. As already stated, the grid was positioned to align with an edge of the device to

be measured and therefore the distance from that edge was known. The grid was calibrated against a structure with accurately known dimensions (length and/or width). The grid operates on a pixel by pixel basis and so a known distance is converted into a given number of pixels (specific to the camera mounting and lens configuration being used with the microscope). The grid can be used to measure a distance with a ± 2 μm accuracy, which is sufficient when considering the maximum thermal spatial resolution of the IR microscope is approximately 3 μm.

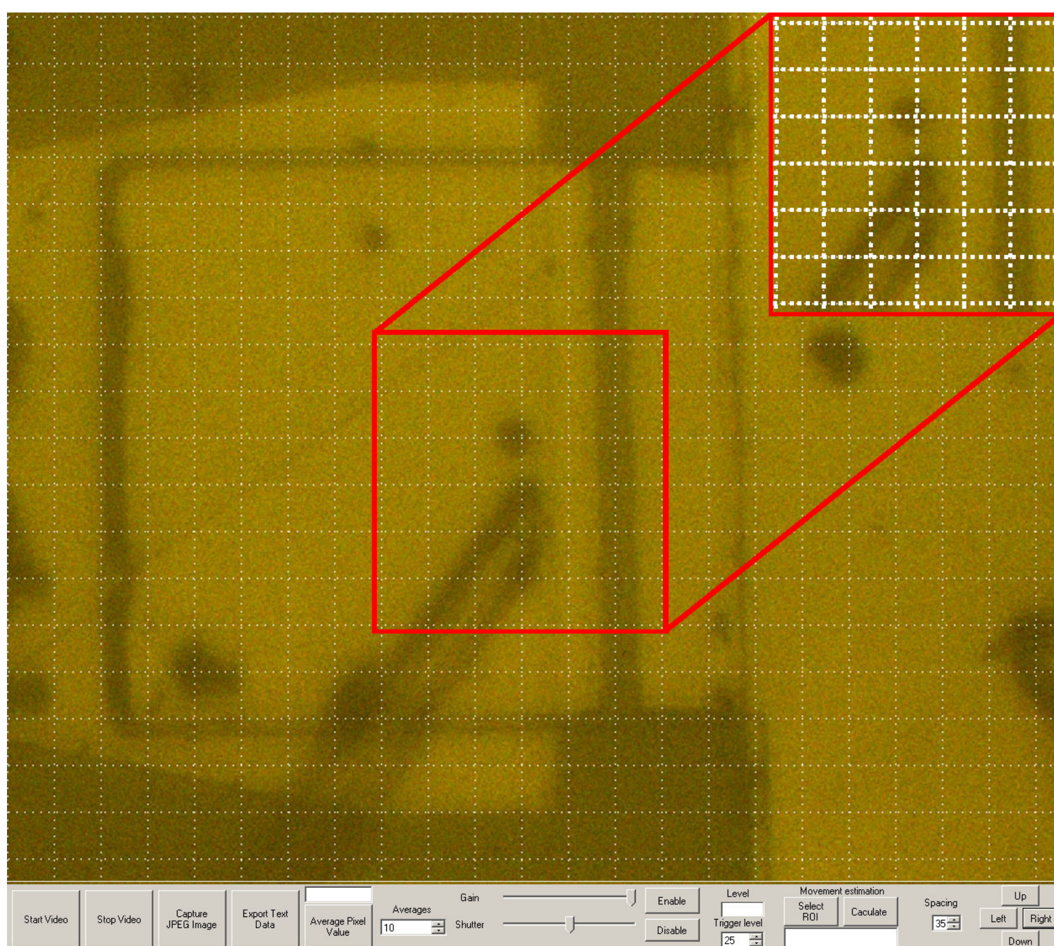

Figure 3.7: *Optical grid, the window matrix dimensions can be changed to enable different diameter micro-particles to be used. An enhanced grid is shown in the insert.*

Chapter 4

Planar Gunn diodes

This chapter describes both the electrical and thermal characterisations made on planar Gunn diodes, which were introduced in section 2.2.
The Gunn diode generates RF/microwave energy from the application of a DC voltage by utilising the Gunn effect (discovered by J. B. Gunn in the 1960s [16; 17; 18]). Planar Gunn diodes were first considered in the 1970s [22], however the required fabrication technology was not available to realise the narrow channels. The University of Aberdeen reintroduced the idea of the planar Gunn diode in 2001 [66] and they collaborated with the University of Glasgow to design and fabricate a planar Gunn diode using GaAs as a base material [1]. In recent years, the University of Glasgow has been able to increase the fundamental frequency of the Gunn oscillations as the fabrication techniques have been developed. Glasgow have also fabricated planar Gunn diodes using an InP based material and have reported a maximum fundamental Gunn oscillation frequency of 164 GHz [5].
A number of electrical (RF and DC) and thermal tests can be performed on a Gunn diode to check, for example; fundamental oscillation frequency, the IV characteristic, and thermal profile. The RF tests (performed at the University of Glasgow) verified the fundamental frequency of operation and output power of the Gunn diode. Basic descriptions of these techniques will be described below. The DC IV electrical tests (to check for an NDR), and thermal measurements (to observe how the heat is distributed across the diode) were performed at De Montfort University. These techniques will be fully described in this chapter. As the RF and DC measurement procedures are well documented [6; 32], minimal descriptions and results will be given.
A number of planar Gunn diode wafers were tested with different channel dimensions and contact metallurgies. All the tested devices showed a similar behaviour, in that when a bias voltage was applied and a current flowed through the channel,

the channel heated up. The path of the current through the channel enabled it to spread at the edges of the anode and cathode contacts (figure 4.1). However, within the centre region of the channel there was less free space for current to spread, therefore, the current was forced to crowd into a smaller space, this current crowding led to high temperatures. All IR measured thermal maps of planar Gunn diodes indicated the coldest temperatures around the channel edges and the highest temperatures around the centre of the channel region. Interestingly, the experimental measurements suggested that the highest temperature of the planar Gunn diode was not always exactly in the centre of the channel.

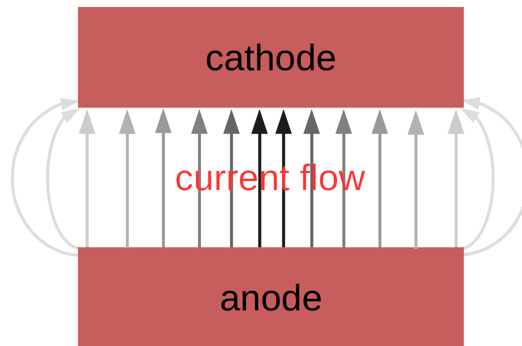

Figure 4.1: *Current flow between anode and cathode contacts of a planar Gunn diode, showing the current spreading at the contact edges.*

4.1 Understanding Gunn diode notations

The planar Gunn diodes used for these measurements had many variations, including; different contact structures, channel lengths, and channel widths. The device labelling showed which fabrication/geometry variations were included. The labels were in the form; "$xxxxy \times z$", where "$xxxx$" was a series of four letters to describe the contact structure, "y" was the channel length, and "z" was the channel width. Descriptions of the contact structures are given in table 4.1, the channel lengths were 1.0, 1.3, 1.5, 2.0, 3.0, or 4.0 μm, and the channel widths were either 60 or 120 μm. There were 5 variations of contact structures, 6 channel lengths, and 2 channel widths, this gave a total of 60 variations of planar Gunn diode available for testing.

Table 4.1: *List of Gunn diode contact structures.*

Contact structure label	**Description**
ACAO	Anode Cathode All Ohmic Figure 4.2(a)
SLAO	Single Low overlap All Ohmic Figure 4.2(b) (Anode has a 0.3 μm Schottky overlap)
SHAO	Single High overlap All Ohmic Figure 4.2(c) (Anode has a 0.5 μm Schottky overlap)
DLAO	Double Low overlap All Ohmic Figure 4.2(d) (Anode and cathode have a 0.3 μm Schottky overlap)
DHAO	Double High overlap All Ohmic Figure 4.2(e) (Anode and cathode have a 0.5 μm Schottky overlap)

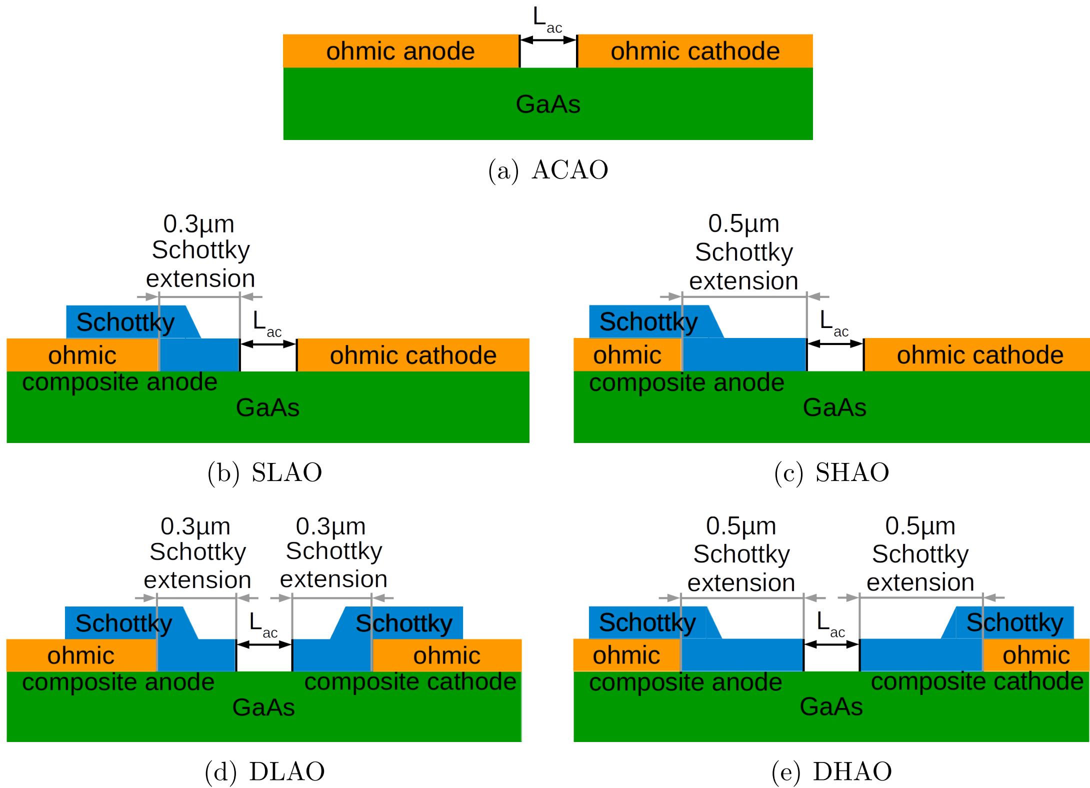

Figure 4.2: *Schematics of planar Gunn diode contact structures.*

4.2 RF measurements

The RF performance of the Gunn diodes were RF characterised using both a vector network analyser (VNA) and a spectrum analyser.

4.2.1 VNA measurements

A VNA can measure the small signal S-parameter of any biased RF device or component using the VNA built-in bias tee. In a two terminal device, S-parameters can be easily used to observe the performance at the input and output port, for example an amplifier. In essence the input S-parameters will give an indication of the input match and forward gain, while the output S-parameters will give an indication of the output match and reverse gain or isolation.
For a 2-port network, there are 4 measurable S-parameters (figure 4.3):

- S_{11} - Input reflection coefficient (match) of port 1 (usually the DUT's input port when under normal signal transmission)
- S_{21} - Forward transmission gain (input at port 1 and output at port 2)
- S_{12} - Reverse transmission gain (input at port 2 and output at port 1)
- S_{22} - Output reflection coefficient (match) of port 2 (usually the DUT's output port when under normal signal transmission)

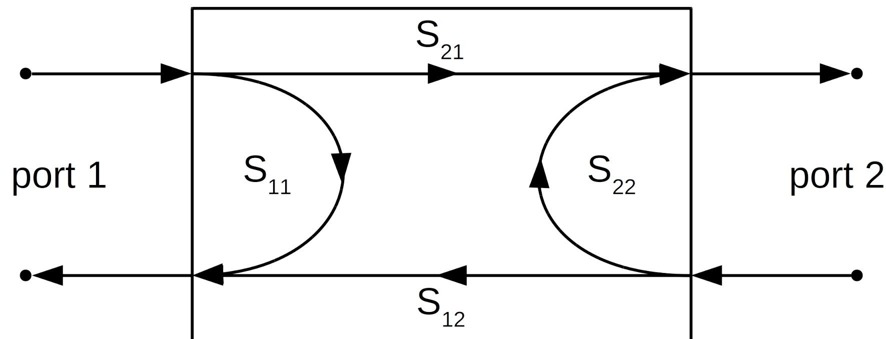

Figure 4.3: *Basic representation of S-parameter pairs for a 2-port network, arrows show direction of signal transmission.*

The planar Gunn diodes from the University of Glasgow are 1-port devices and so only S_{11} was available for measurement. However, S_{11} analyses the input

requirements for the Gunn diode, enabling the design of a matching circuit to utilise the planar Gunn diode efficiently [6; 32].

4.2.2 Spectrum analyser measurements

A spectrum analyser measures the frequency response of the device. With reference to the biased planar Gunn diode it enabled measurement of the fundamental frequency of oscillation and harmonic components. It was also used to give an indication of the power output at the fundamental frequency and the harmonics. Figure 4.4 shows a typical experimental set-up for measuring a Gunn diode using a spectrum analyser. In the experimental set-up, the DUT is connected to a bias tee. The bias tee enabled the DUT to be DC biased while receiving an RF signal from the DUT along the same cable/connection. RF isolation from DC was needed as the spectrum analyser can not handle the DC power, which, if sufficiently high would damage the delicate mixer diodes of the spectrum analyser.

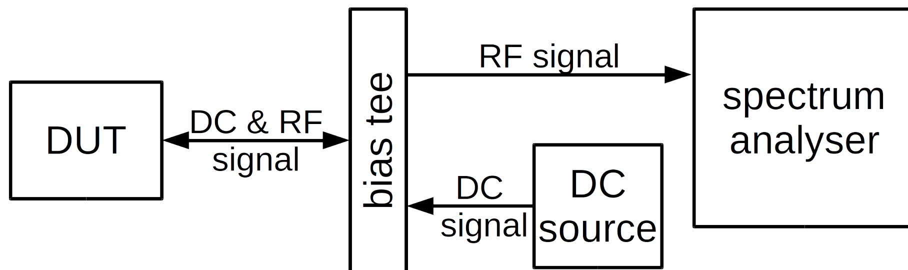

Figure 4.4: *Basic spectrum analyser set-up for devices.*

A spectrum analyser separates each frequency found within the input RF signal. Therefore, it displays which frequencies were in the output (from the DUT) and gives an indication of the magnitude of the respective harmonic powers. In the case of the Gunn diode, normally, the lowest frequency (and highest power) observed will be the fundamental oscillation frequency of the Gunn diode.

4.3 DC measurements

This research has focussed on measurements used to characterise the DC and thermal performance of a device. One of the simplest, but most useful, DC tests is the measurement of the IV characteristic. To measure the IV characteristic of a planar Gunn diode, a voltage step is applied to the Gunn diode and the current

drawn by the diode is measured. De Montfort University has set-up a semi-automated 4-probe IV measurement system. The system is semi-automatic as the DC probes have to be manually positioned. Manual probes allow for probing of a large variety of devices, even with unusual contact geometries or when anodes and cathodes are at different heights, for example when one contact is on mesa and the other is off mesa. Once the probes are in position the IV measurement system software sets the voltage of the power supply and then measures the current and voltage, for each voltage step. From this data the software generates the device IV characteristic.

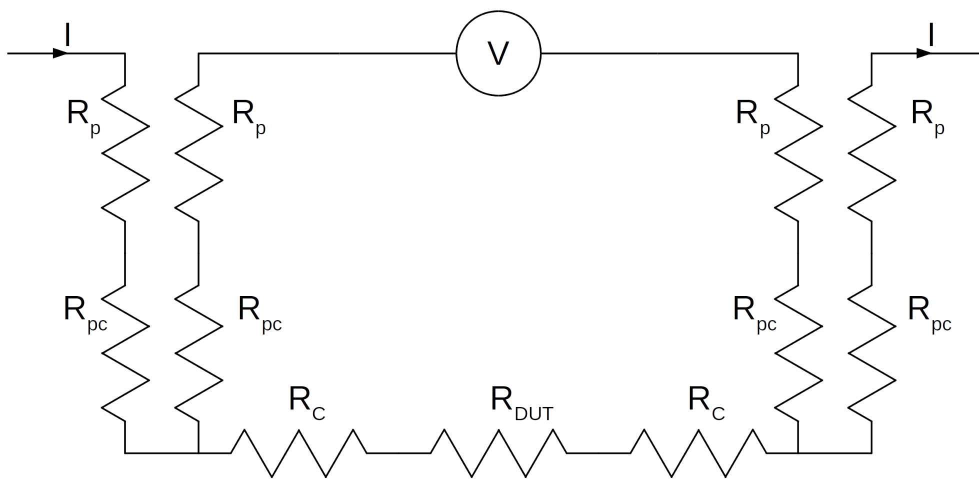

Figure 4.5: *Schematic showing the resistances involved with probing a DUT. Where R_{p} is the resistance of the probe, R_{pc} is the contact resistance between the probe and the DUT's contacts, R_{C} is the contact resistance between the DUT's metal contacts and the semiconductor, and R_{DUT} is the resistance due to the DUT itself.*

A 4-probe measurement method was used to improve the accuracy of the IV measurement. If the voltage was measured directly from the power supply, the value may not be accurate. This occurs as the power supply has a low resistance to allow the DUT to draw the full current required. Thus, if the current or probe resistance was high, there would be a small but non-negligible voltage drop across the resistances associated with the probe set-up (figure 4.5) giving an incorrectly measured bias voltage across the DUT. However, using four probes and connecting a voltmeter across the device via two of the probes enables the voltage supplied to the DUT to be measured. Note a voltmeter has a very high resistance ($\sim$40 MΩ). The high resistance of the voltmeter provides a high, total resistance in the voltage sense loop, therefore there is a negligible current flow in the loop, making the voltage drop across the measurement probes negligible.

The voltage measured using a 4-probe measurement will always be less than the voltage applied by the power supply.

4.3.1 Semi-automatic IV measurement system

The De Montfort University semi-automatic IV measurement system was originally developed as part of a Masters (MSc) project [67], but has been updated and developed to make IV measurements on most electronic devices, including Gunn diodes. The system utilises a PL303QMD-P power supply from Aim-TTi to supply the voltage to the DUT and to measure the current drawn, and a 34405A multimeter from Agilent to measure the voltage from the additional voltage sense probes. The 4-probe (figure 4.6) set-up uses Wentworth probe manipulators, mounted on an anti-vibration microscope table, which is part of the IR and optical microscope set-up (figure 4.7).

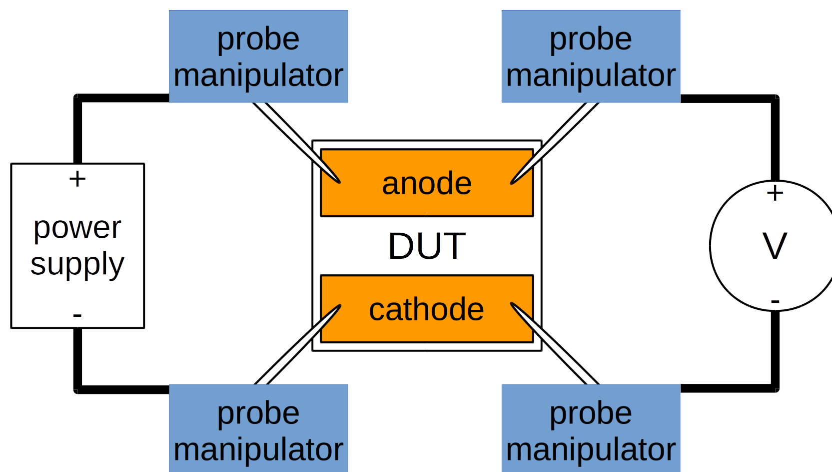

Figure 4.6: *Basic set-up for 4-probe IV measurements.*

The control software for the IV measurement system increases the power supply output voltage (starting from 0 V) in steps of 0.01 V. The software (figure 4.8) allows for three user-defined variables to be set; the maximum voltage, the maximum current, and the delay for the system to wait before implementing the next voltage step. The IV measurement is complete when; either the maximum voltage or maximum current is reached. The measurement will also stop if a negative or no current is detected. The delay option can be used to enable voltage and current values to stabilise before making the next reading. During a measurement, real-time values are generated including an instantaneous resistance.

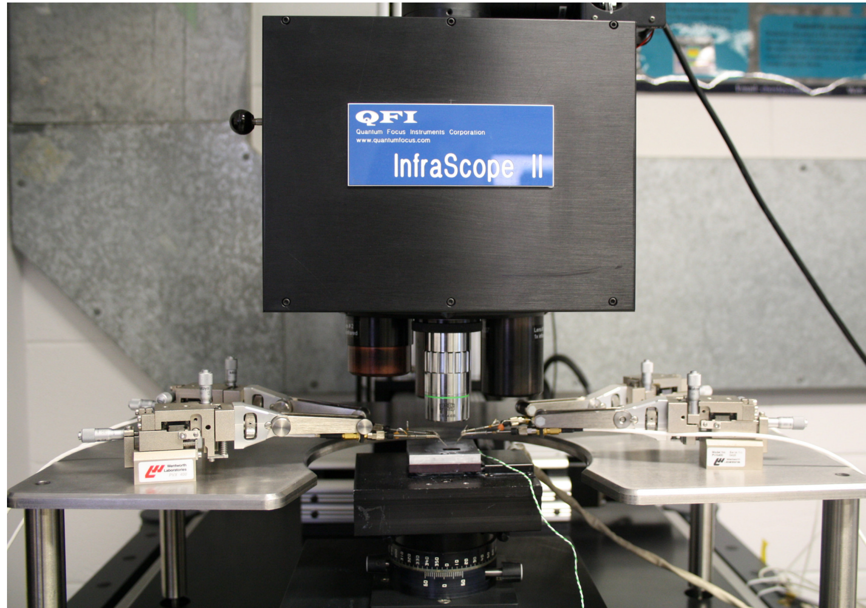

Figure 4.7: *De Montfort University's microscope table with four probes for analysing DC of on-wafer devices.*

Figure 4.8 shows a very slightly higher resistance was measured from the 2-probe measurement compared to the 4-probe measurement. Also, the voltage measured from the power supply (2-probe measurement) is not as accurate (2 decimal places) as that measured by the voltmeter (3 decimal places). The plots (figure 4.8) show a jagged IV characteristic, this is because the 1.2 kΩ test device, has a relatively high resistance, meaning that the current step measured for a 10 mV voltage increase is too small for the 100 μA (0.1 mA) resolution of the power supply, therefore, the voltage step needed to be increased, but this feature is not available in the current version of the semi-automatic IV software.
As there were a number of geometrical and contact variations of planar Gunn diode to be measured, only a representative number of the IV characteristics are presented. These were all measured using the described semi-automatic IV measurement system, and the Gunn diodes showed a noticeable NDR (figure 4.9). It should be noted that not all the Gunn diodes measured on-wafer were functional, the IV characterisation was primarily used to select Gunn diodes for thermal characterisation.
Figure 4.9 shows the IV characteristics for three different Gunn diodes, all with different contact structures. Both of the devices with 2×60 μm channels showed a very similar IV characteristic, regardless of the different contact structures. The linear region (before the NDR) of the Gunn diode with the 120 μm wide channel showed a higher resistance than the two Gunn diodes with 60 μm wide channels.

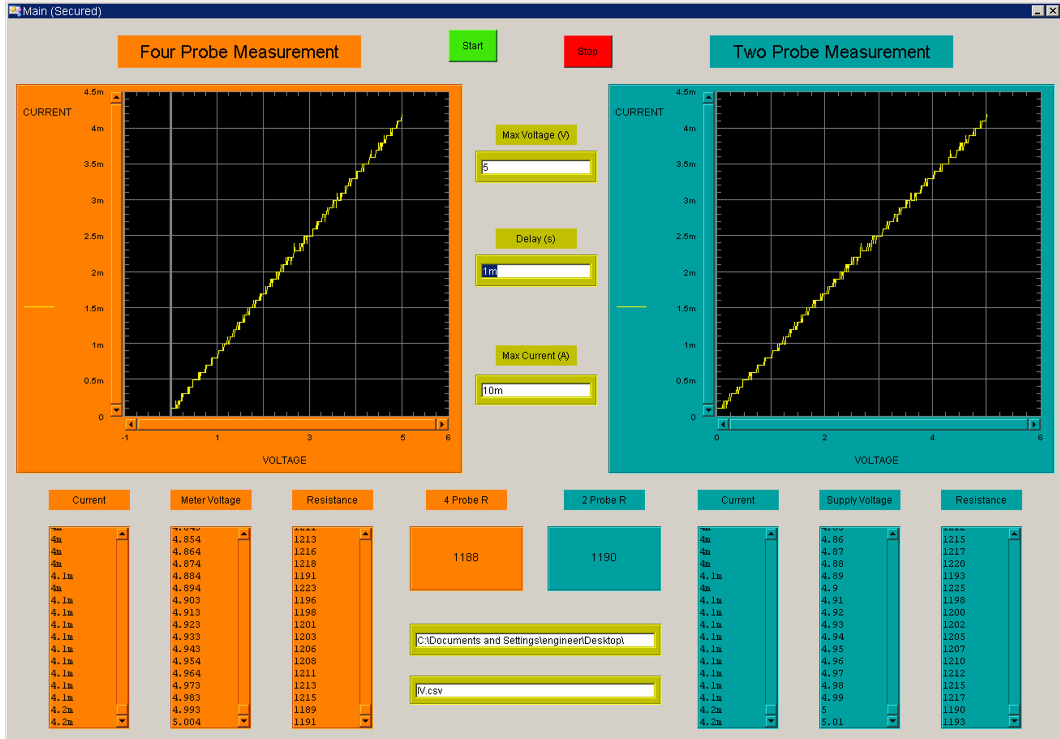

Figure 4.8: *Screenshot of De Montfort University's semi-automatic IV measurement software, after having performed a measurement on a 1.2 kΩ resistor.*

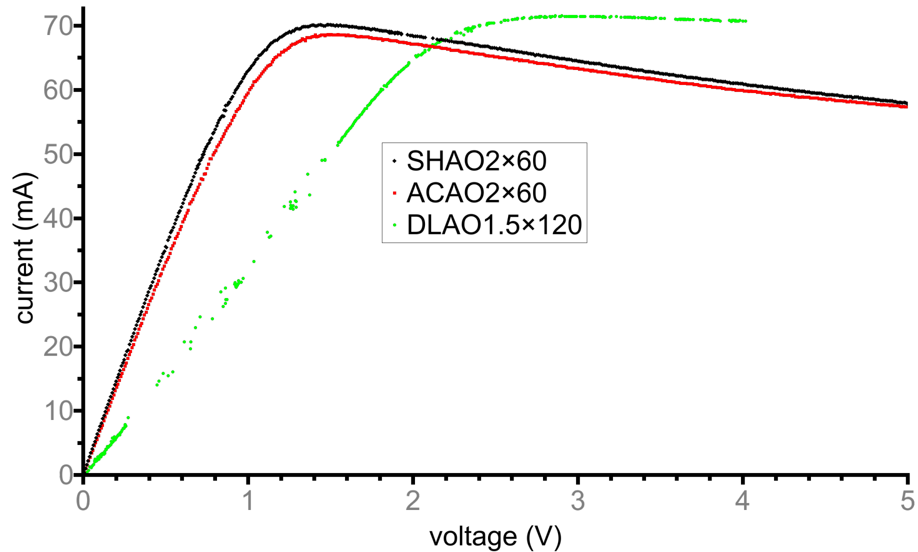

Figure 4.9: *IV characteristic of three planar Gunn diodes, two with 2×60 μm channels, and one with a 1.5×120 μm channel, all with different contact structures.*

4.4 Thermal measurement techniques

IR thermal microscopy measurements of the planar Gunn diode will give the maximum temperature and thermal distribution within the device channel. It can also identify faults associated with the manufacturing process, for example a hot-spot due to current crowding from irregular edges of the metallised contacts. Thermal profiles were measured for each Gunn diode fabrication run to investigate if there were improvements in the thermal behaviour as the Gunn diode fabrication process was developed. The measurement was also used to identify any problems in the fabrication run, for example irregular metallisation of the metal contacts. A detailed description of the thermal microscopy measurement technique was described in chapters 2 (section 2.1) and 3. There were two main thermal measurement techniques used on the planar Gunn diodes:

1. Conventional IR thermal measurements; to profile the temperature distribution and measure the temperature of the Gunn diode metal contacts.
2. Micro-particle thermal profiles (by manipulating a micro-particle into multiple positions along/across the channel of the planar Gunn diode); to measure in-channel temperatures more accurately.

4.4.1 Conventional IR thermal measurements

Conventional IR thermal measurements were utilised to perform quick thermal profiles to show the thermal distribution within the channel region as well as the location of hot-spots. Conventional IR thermal measurements also enabled temperatures to be measured at the metallised contacts where a reliable (but low) surface emissivity (∼0.1) was obtained.

The conventional IR thermal profile of a planar Gunn diode showed the temperature distribution, however without using a micro-particle sensor accurate in-channel temperatures could not be measured. This was due to poor values of surface emissivities being recorded from the semiconductor region of the channel (section 2.1.3). The micro-particle sensor technique was also used to measure the temperature of any located hot-spot.

Below is a sample of thermal measurements from early wafers of planar Gunn diodes. A selection of channel sizes, contact structures, bias conditions, and operating temperatures have been included. A summary of the measured planar Gunn diodes is shown in table 4.2.

Table 4.2: *Planar Gunn diodes measured by conventional IR thermal microscopy.*

Figure number	**Device notation**	**Bias conditions**	**Operating temperature**	**Reason for inclusion**
4.10	SLAO1×60	1.50 V 20.0 mA	109.5 °C	60 μm wide channel
4.11	SHAO1.5×120	2.10 V 50.0 mA	109.5 °C	sub-3 μm channel length
4.12	ACAO1×120	2.50 V 50.0 mA	109.5 °C	in-channel hot-spot
4.13	ACAO3×120	3.51 V 55.9 mA	49.3 °C	low operating temperature

Figures 4.10 to 4.13 show measurements made on planar Gunn diodes and all have differing thermal profiles. However, the basic behaviours were similar. The channel edges were coolest and the central channel region was hottest. Exact contact edge temperatures differed due to the different bias conditions and it should be remembered that the surface emissivity of the contacts was low (∼0.1).
SLAO1×60 (figure 4.10) was the only included planar Gunn diode with a 60 μm wide channel. The peak temperature was not as high as the measured Gunn diodes with 120 μm wide channels.
SHAO1.5×120 (figure 4.11) was an example of a planar Gunn diode that could only be thermally profiled using conventional IR thermal microscopy because the sub-3 μm channel length (1.5 μm) was unable to accommodate the smallest available 2 μm diameter micro-particle sensor. The channel was also shorter than the thermal spatial resolution of the IR microscope, and so the IR microscope will measure IR radiation from both sides of the channel.
ACAO1×120 (figure 4.12) had a significant hot-spot in the channel (left of the channel centre). However, this was not clearly identified using the conventional IR thermal profile of the metallised cathode edge (bottom left corner of the figure). This was not unexpected as the channel length of the device was 1 μm.
ACAO3×120 (figure 4.13) appeared to have a very noisy thermal profile, with lots of temperature variations along the width of the active region. This was due to the low operating temperature (49.3 °C) of the measurement and shows that thermal measurements need to be made at higher operating temperatures.

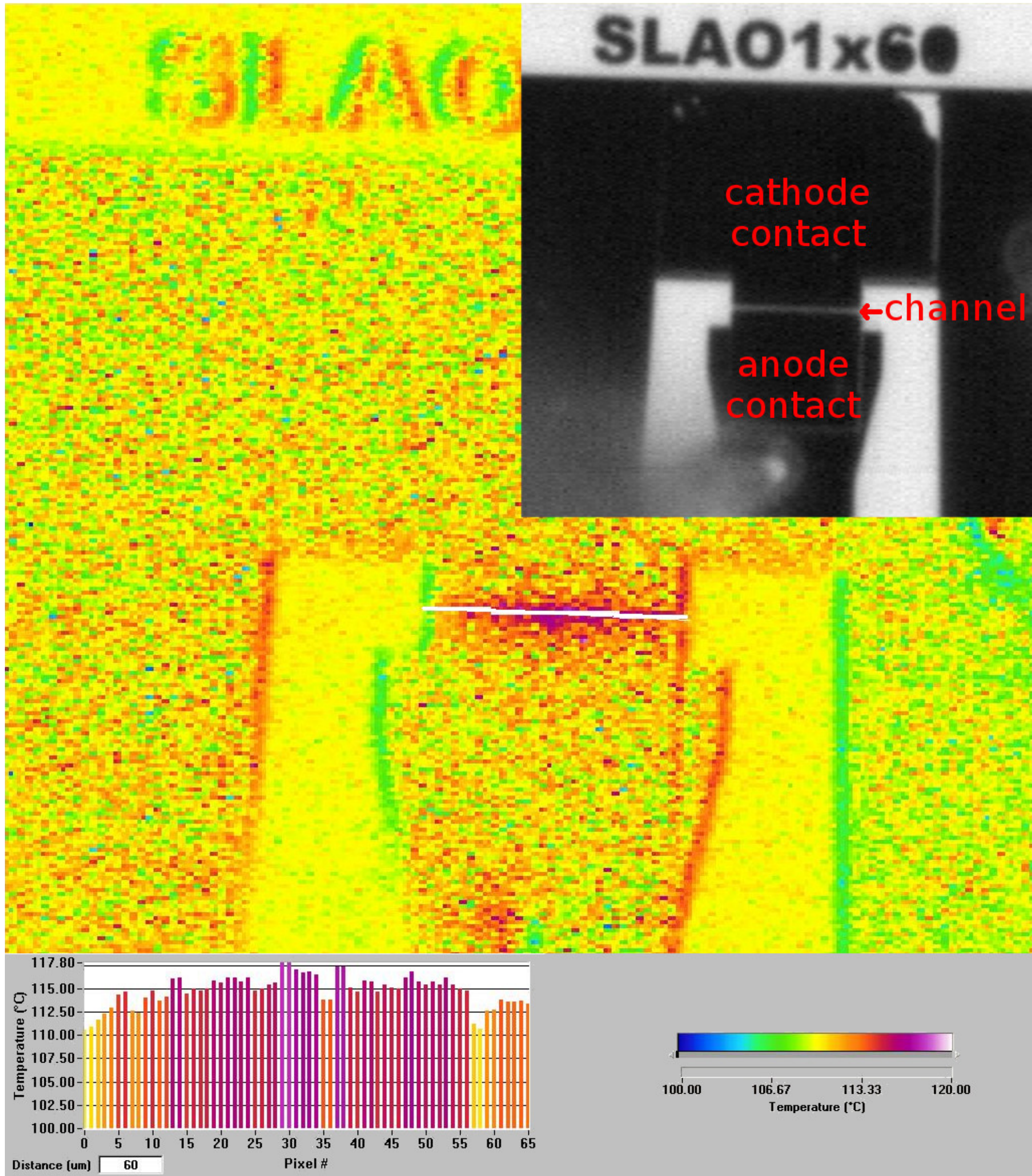

Figure 4.10: *Conventional IR thermal measurement on a SLAO1×60 Gunn diode (reference image, top right). Biased to 1.50 V and 20.0 mA (30 mW) at an operating temperature of 109.5 °C. With thermal profile (bottom left corner) taken along the cathode edge (white line in thermal image).*

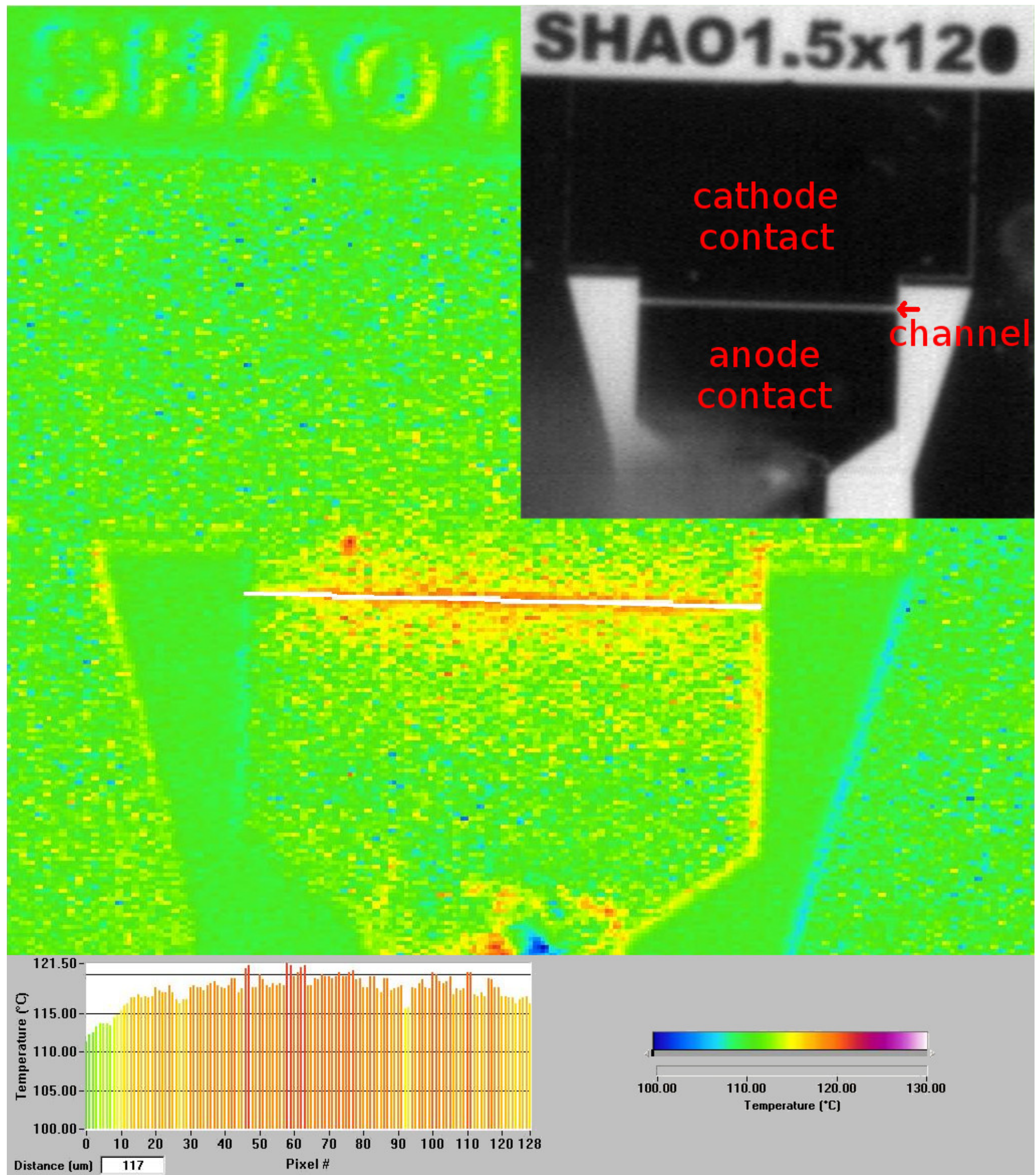

Figure 4.11: *Conventional IR thermal measurement on a SHAO1.5×120 Gunn diode (reference image, top right). Biased to 2.10 V and 50.0 mA (105 mW) at an operating temperature of 109.5 °C. With thermal profile (bottom left corner) taken along the cathode edge (white line in thermal image).*

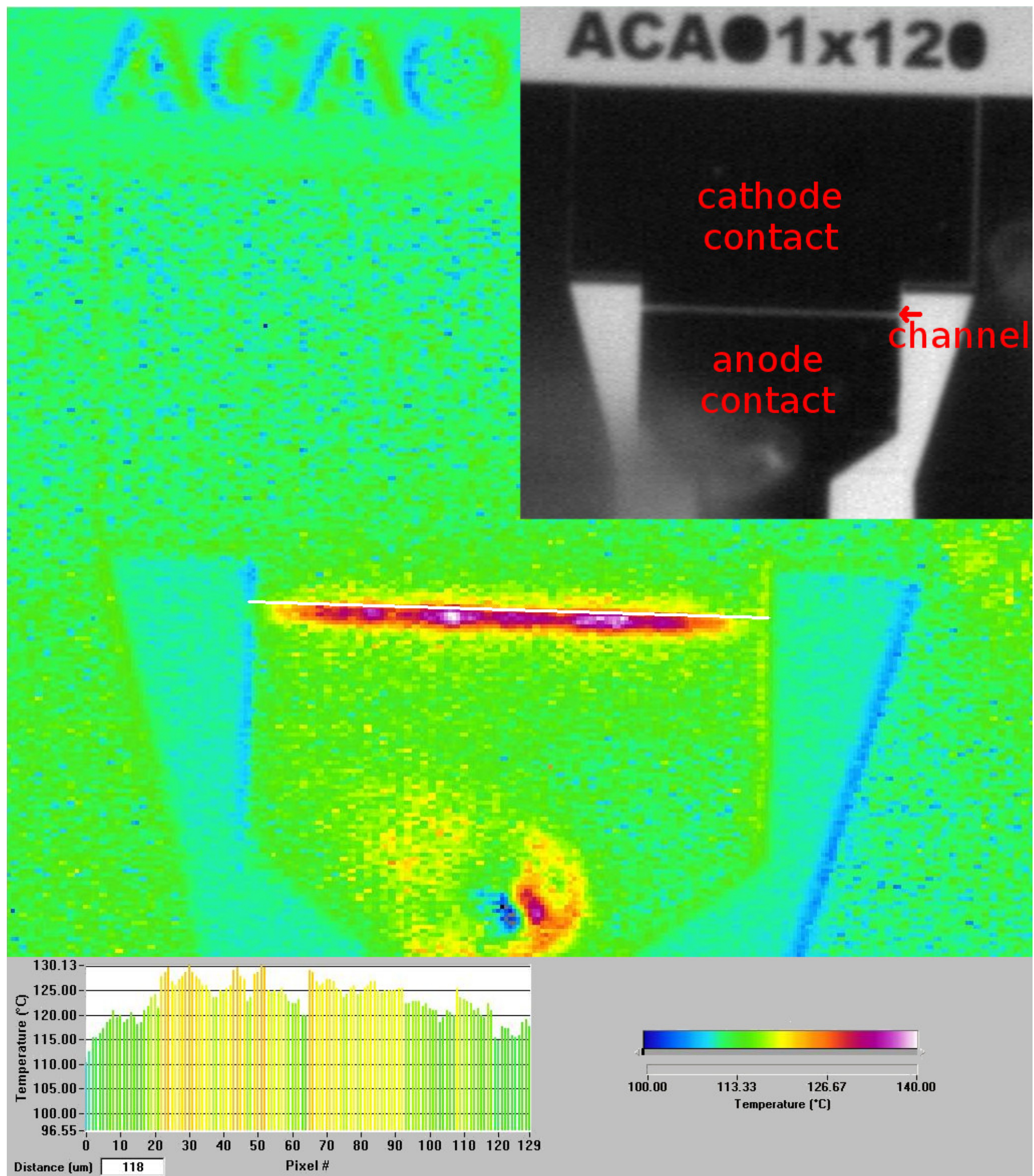

Figure 4.12: *Conventional IR thermal measurement on an ACAO1×120 Gunn diode (reference image, top right). Biased to 2.50 V and 50.0 mA (125 mW) at an operating temperature of 109.5 °C. With thermal profile (bottom left corner) taken along the cathode edge (white line in thermal image).*

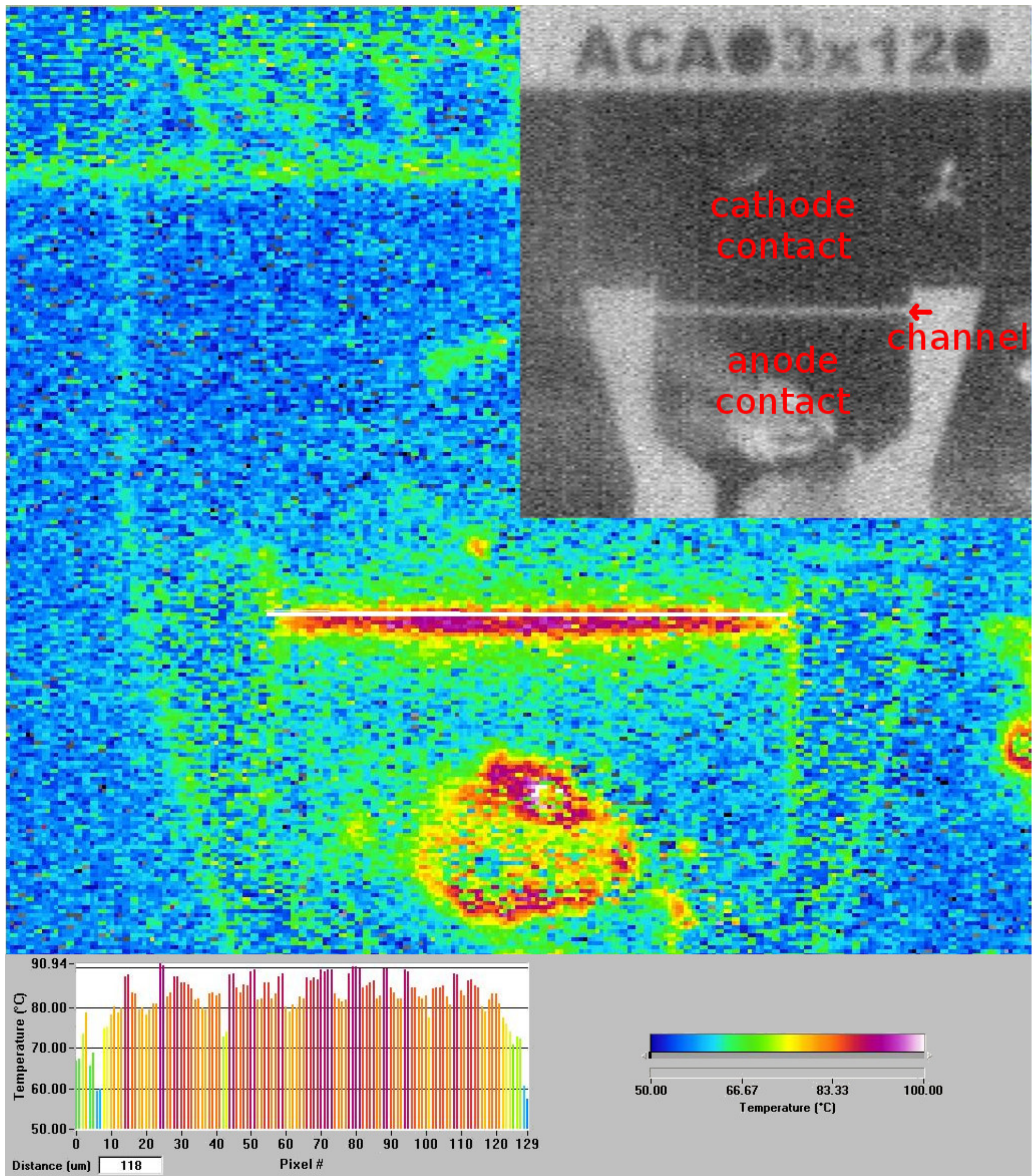

Figure 4.13: *Conventional IR thermal measurement on an ACAO3×120 Gunn diode (reference image, top right). Biased to 3.51 V and 55.8 mA (195.9 mW) at an operating temperature of 49.3 °C. With thermal profile (bottom left corner) taken along the cathode edge (white line in thermal image).*

4.4.2 Micro-particle IR thermal profile measurements

The novel use of the micro-particle sensor, micro-manipulator, and optical grid enabled the development of a more accurate point to point thermal measurement along the channel of a planar Gunn diode using the QFI InfraScope II. The technique was not dependent on the surface emissivity of the material being measured, but only on the surface emissivity of the micro-particle, which was calibrated before the measurement. The micro-particle sensor was positioned using the micro-manipulator and optical grid giving a relatively high degree of accuracy.

The measurement technique developed and used on the planar Gunn diode enabled thermal profiles to be plotted inside the channel region. This was achieved by placing a micro-particle into the first of a number of predefined locations. The planar Gunn diode was then biased and the micro-particle temperature measured. The micro-particle was then repositioned at the next location and the bias repeated (carefully ensuring the same bias voltage and current). This process was repeated until all the required locations had been measured. Small changes in the bias condition had a negligible effect on the results. However, variation in bias conditions occurred due to the removal of the bias probes to enable repositioning of the micro-particle sensor. Repositioning the bias probes scratched and damaged the contacts slightly, thereby changing the contact resistance. Only using one particle and manipulating it into many positions ensured only one emissivity calibration was needed, as it was assumed the emissivity of the particle would not vary between measurements.

The planar Gunn diode measurements showed the channel temperature was surprisingly low when the diode was biased at voltages just below the NDR region (NDR of most 3×120 μm channel planar Gunn diodes occurred between 3.5 and 5.0 V). The temperature increased as the bias voltage and diode current increased. The single micro-particle sensor also minimised thermal loading of the Gunn diode (section 2.1.1).

The thermal profiles were measured both across the channel of a Gunn diode (going from metal anode, through the GaAs based channel, to the metal cathode contact), figure 4.14, and along the channel width of a Gunn diode (going from the left to right channel edge), figure 4.15.

This technique enabled the measurement of the thermal profiles of many planar Gunn diodes, however due to the IR spatial resolution of the InfraScope II being limited to $\sim$3 μm, only channel lengths of $\geq$3 μm were profiled with a micro-particle sensor of diameter approximately equal to the channel length.

An example of a micro-particle sensor thermal profile across the channel of a planar Gunn diode is shown in figure 4.16. The measured temperature rise above operating temperature was plotted for each micro-particle position, building up

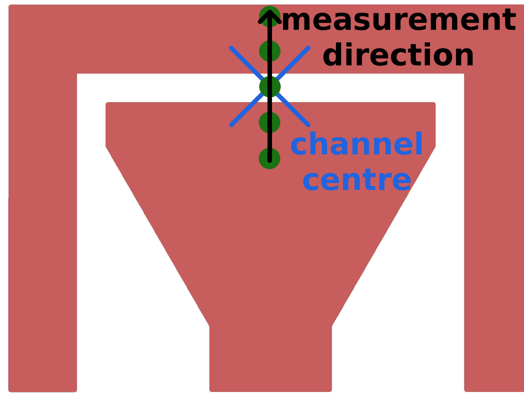

Figure 4.14: *Schematic showing measurement direction in relation to Gunn contacts for thermal profiles made with a micro-particle sensor manipulated across the channel of a planar Gunn diode.*

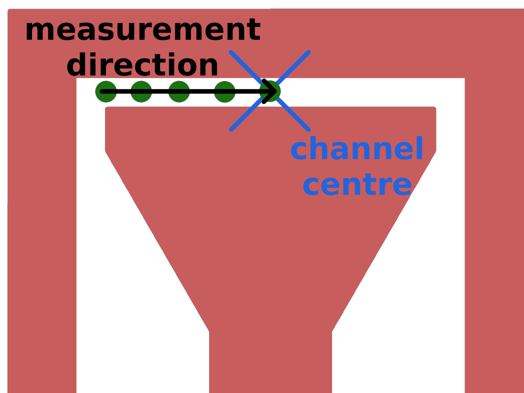

Figure 4.15: *Schematic showing measurement direction in relation to Gunn contacts for thermal profiles made with a micro-particle sensor manipulated along the channel of a planar Gunn diode.*

the thermal profile. In this experiment, a single micro-particle sensor was manipulated across an ACAO3×120 device (from anode to cathode contacts), the thermal measurement was made at nine positions. Figure 4.16 shows how the temperature was distributed through the metal contacts and into the channel region. At each of the nine micro-particle locations, the thermal measurement was made at four bias voltages (2.0, 2.5, 3.0, and 3.5 V, ±0.02 V), with the equivalent average input powers of 70, 110, 155, and 195 mW respectively. The average input power was computed by taking the average of all nine bias conditions, representing each micro-particle position. The NDR for the ACAO3×120 Gunn diode was approximately 4.0 V.

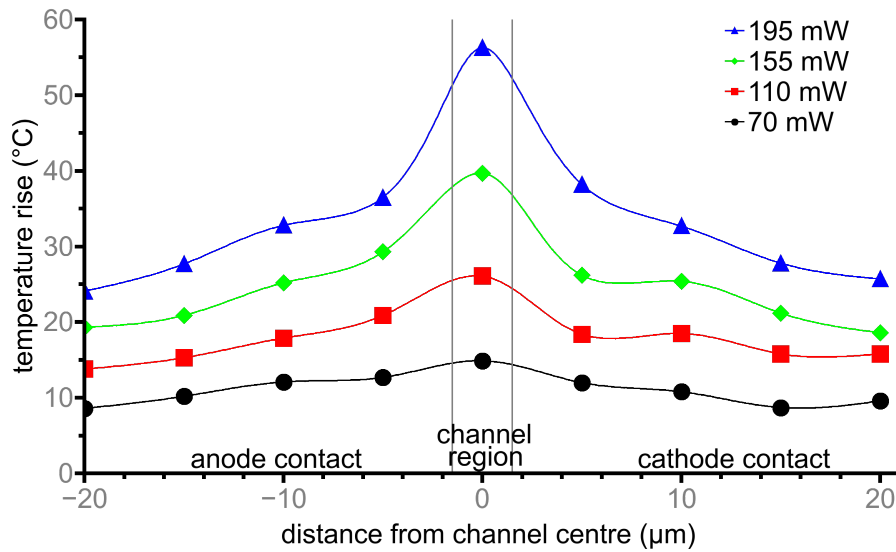

Figure 4.16: *An ACAO3×120 profiled across the channel, at 9 positions (from anode to cathode) and four bias conditions (2.0, 2.5, 3.0, and 3.5 V) at an operating temperature of 49.3 °C.*

The measured thermal profile across the channel of the device was well behaved and showed a similar trend for all the measured planar Gunn variants. As the bias voltage was increased, the peak central temperature increased faster than the temperature of the metal electrodes. This measurement is not possible using Raman thermal spectroscopy, as the Raman signal would not be detected in the metallised contact regions. However, Raman would give an improved thermal resolution for the temperatures in the channel. The combination of more than one thermal measurement technique shows the advantage of obtaining more complete thermal maps and profiles (high channel resolution and a thermal map across the metal contacts).

Figures 4.17 & 4.19 are examples of a micro-particle sensor thermal profiles along the channel width of a planar Gunn diode. Again, the temperature rise was plotted above operating temperature for each micro-particle position and a single micro-particle sensor was manipulated. The micro-particle was positioned along the channel of both planar Gunn diodes, from left to right channel edge (for a device imaged in the same orientation as in figure 4.15). The thermal profiles show how the temperature was distributed through the channel width of the devices for different DC bias levels.

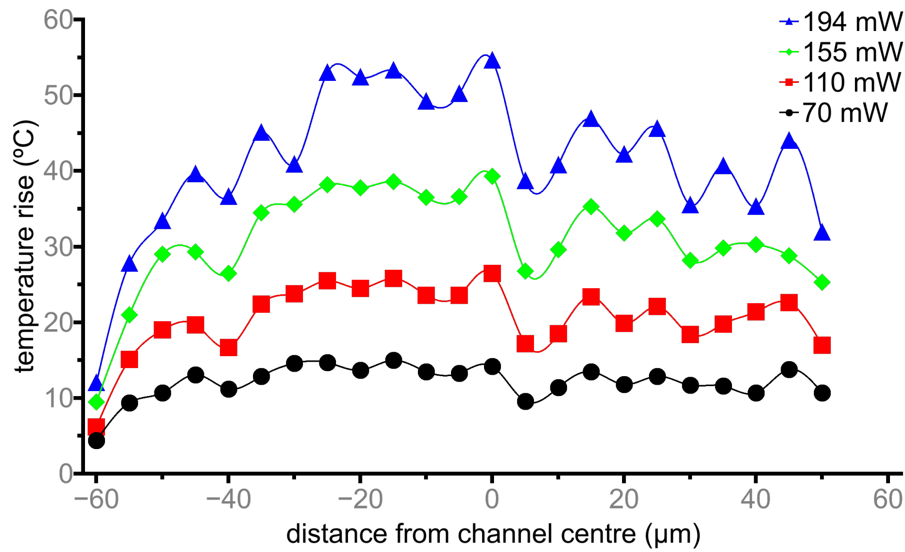

Figure 4.17: *An ACAO4×120 profiled along the channel, at 23 positions (from left to right channel edge) and four bias conditions (2.0, 2.5, 3.0, and 3.5 V) at an operating temperature of 79.2 °C.*

In figure 4.17, a thermal measurement was made for each micro-particle location (23 in total) at four bias voltages (2.0, 2.5, 3.0, and 3.5 V, ±0.01 V), representing equivalent average input powers of 70, 110, 155, and 194 mW respectively. Again, the input power was averaged for all 23 bias conditions, representing each micro-particle position. Only 110 μm of the 120 μm channel width was profiled. This was because repositioning the micro-particle sensor required the movement of the DC probes, which led to damage to the contacts of the Gunn diode. Figure 4.17 shows that ACAO4×120 had a non-uniform temperature distribution. A possible explanation can be offered by assuming:

(i) The current distribution is uniform.

(ii) The thermal impedance is uniform.

If the current distribution is uniform, then the thermal impedance must be changing across the channel width and if the thermal impedance is uniform, then the current distribution must be changing across the channel width. Both of these scenarios could occur due to material defects and/or non-uniform doping in the semiconductor layers. The current distribution will also be effected by geometry and irregular edges on the metallised contacts. Non-uniform current distribution is the most likely reason for the temperature distribution in the channel. The current (I) in the channel could be approximated as:

$$\mathrm{I} = \frac{\mathrm{T_{rise}}}{\Theta \cdot \mathrm{V}} \tag{4.1}$$

Where $\mathrm{T_{rise}}$ is the channel temperature rise (°C), Θ is the thermal impedance (°C/W), and V is the bias voltage (V).

To a further approximation the device thermal resistance (Θ) can be assumed constant and as the measured anode and cathode contacts are relatively narrow (120 μm) the bias voltage (V) variation along their width can be considered as constant. Therefore, the current (I) in the channel can be considered as proportional to the temperature rise ($\mathrm{T_{rise}}$). This enables an estimate of current distribution along the channel, as shown in figure 4.18.

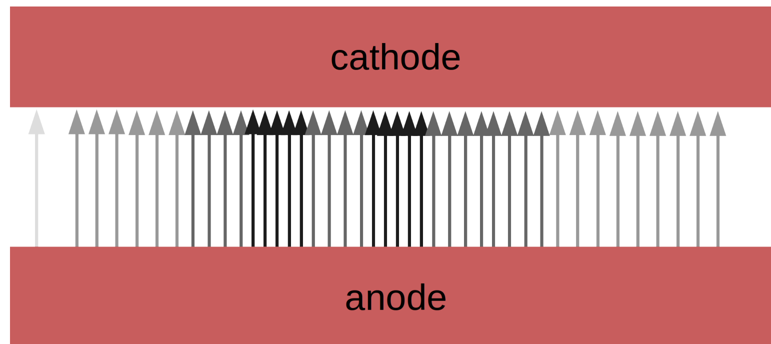

Figure 4.18: *Current distribution along ACAO4×120 channel. Showing the highest current density towards the channel centre and lowest current density around the channel edges, as described in figure 4.1.*

It was interesting to note that the temperature started to fall significantly in the last 10 to 20 μm before the edge of the channel width was reached. This behaviour can also be seen in figure 4.19. This effect can be explained by non-uniform current distribution (figures 4.1 & 4.18). There was also a good correlation in the central peak temperature for measurements both across (figure 4.16) and along (figure 4.17) the channel. It should be noted the Gunn diode in figure 4.16 (ACAO3×120) had a 3 μm long channel, while the Gunn diode in figure 4.17

(ACAO4×120) had a 4 μm long channel, both had ohmic contacts with a 120 μm wide channel.
Further comparisons with figures 4.16 & 4.17 can be made with a thermal profile along the channel made on Gunn diode ACAO3×120 (figure 4.19).

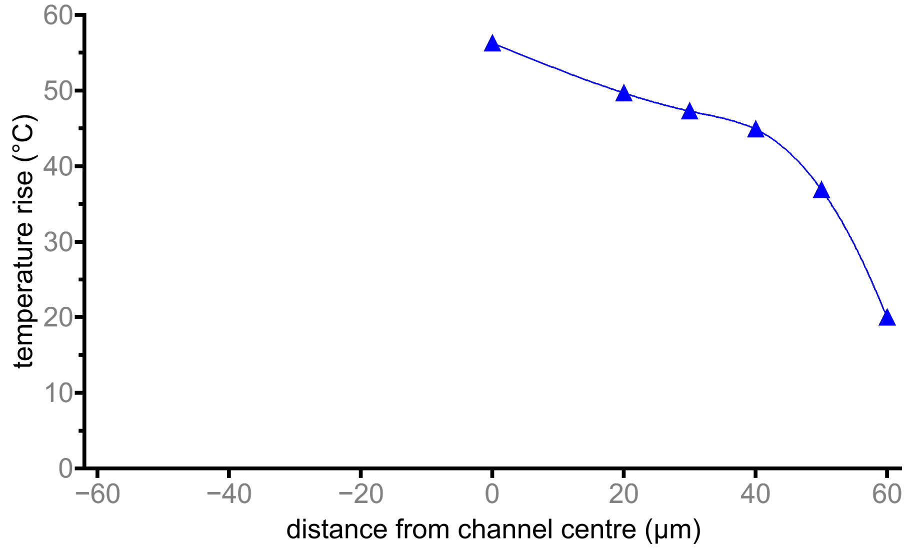

Figure 4.19: *An ACAO3×120 profiled along the channel, at 6 positions (from channel centre to right edge) at a single bias condition (3.5 V) at an operating temperature of 49.3 °C.*

In figure 4.19, the thermal measurement was made for each micro-particle location (6 in total) at a single bias voltage (3.5 V, ±0.01 V), which represented an equivalent average input power of 195 mW. Only 60 μm (the right half) of the 120 μm channel width was profiled. As with the ACAO4×120 device (from figure 4.17), repositioning the micro-particle sensor and the DC probes numerous times led to damage of the device metallised contacts. It is interesting to note that the temperature at the right channel edge (60 μm from the channel centre), measured in figure 4.19, was cooler than the centre of either the anode or cathode contact, up to 20 μm from the channel centre (measured in figure 4.16) for the same bias voltage.
A significant problem was encountered when manipulating a single micro-particle sensor along the channel width of a planar Gunn diode, this was damage caused to the metal contacts by having to move the DC bias probes for each repositioning of the micro-particle. This led to an attempt at thermally profiling along the channel width of a planar Gunn diode using multiple micro-particle sensors. The micro-particles were all placed within the channel of a single planar Gunn diode (at 10 μm intervals), as shown in figure 4.20.

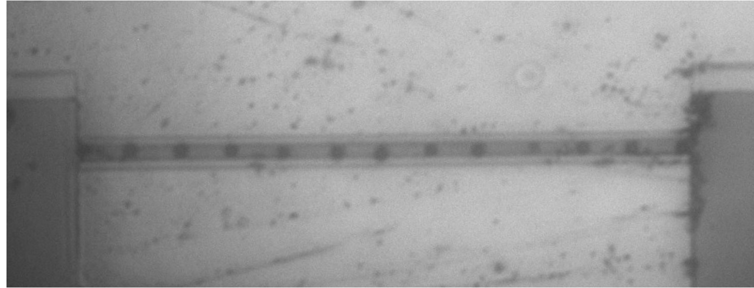

Figure 4.20: *13 micro-particle sensors placed within the channel of an ACAO3×120 planar Gunn diode.*

Using multiple micro-particle sensors in a single Gunn channel allowed the whole channel to be profiled using a single thermal measurement. This meant that the device only needed to be biased once to achieve the thermal profile. Therefore, it was easier to test the device under many bias conditions and to repeat the device thermal measurement. As the micro-particle diameters were very small (∼3 μm) and spaced at 10 μm intervals, it was assumed that the thermal loading was minimal on the planar Gunn diode.
Figure 4.21 shows the measured temperatures for 13 micro-particle sensors, located along the channel width for ACAO3×120, using a single IR thermal measurement. To obtain an indication of the expected error, the measurement was repeated three times for each bias voltage. The device was biased at eight different bias voltages (0.5, 1.0, 1.5, 2.0, 2.5, 3.0, 3.5, and 4.0 V, ±0.01 V), which represented average input powers of 4, 16, 37, 67, 104, 142, 173, and 202 mW respectively. The temperatures and input powers represent the average of the three repeated measurement sets. From the measurements, the average error was ±0.5 °C, however one point (power input 141 mW, at position +30 μm) had an error of ±2.5 °C.
Figure 4.21 shows a complete thermal profile along the whole channel width of a planar Gunn diode. The measurements were made a number of times with the same set of bias voltages (enabling average measurement values to be used). The thermal distribution clearly shows that the channel edges were much cooler than the central channel region and the hottest region was around the channel centre. However, the left side of the channel (negative distances on the x-axis) showed higher temperatures than the right. This was possibly due to an irregularity in the deposition of the metallised contacts.
Figures 4.19 & 4.21 both show thermal profiles along the channel of ACAO3×120. A complete comparison between the single micro-particle and multiple micro-particle IR thermal measurements can not be made, as figure 4.19 is not a complete thermal profile. However, a basic comparison between figures 4.19 & 4.21

can be made as both show results at a 3.5 V bias voltage. A similar thermal behaviour is observed from both measurements (only on the right-hand side of the Gunn channel), with a slight difference in temperature. The differences may be due to the multiple micro-particle sensors slightly thermally loading the channel, so modifying the current distribution. The micro-particle manipulation process is still ongoing research, with an aim of not requiring the removal of bias probes to manipulate a micro-particle sensor in the channel of a DUT.

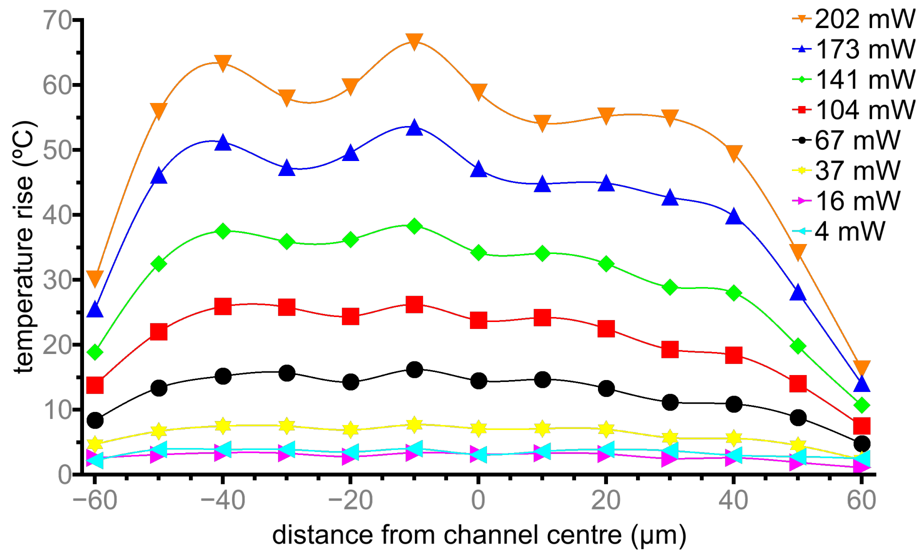

Figure 4.21: *An ACAO3×120 profiled along the channel, by 13 micro-particle sensors, positioned from the left to the right edge of the channel at the same time, at 8 bias conditions (0.5, 1.0, 1.5, 2.0, 2.5, 3.0, 3.5, and 4.0 V) at an operating temperature of 98.8 °C.*

4.5 Summary

This chapter showed:

- A novel single IR micro-particle sensor measurement technique, which has enabled thermal profiling of the channel in a planar Gunn diode, has been described.
- Multiple micro-particle sensors were used to perform in-channel thermal profiles using a single thermal measurement. However, further research is required to understand possible electrical/thermal loading due to the number of micro-particles.

Chapter 5

Micro-coolers

Micro-coolers are devices that can be used to transfer heat from an active device or heated region. Micro-cooler is a term used to describe any small-scale cooling device, however within the context of this thesis the dimensions of the coolers will be of the order of hundreds of microns. Therefore, as sub-millimetre coolers are being considered, the conventional PN thermoelectric cooler is not a solution (too large) and a superlattice micro-cooler was researched. Within this research work a planar Gunn diode is used as the active device to be cooled. The research goal was to directly integrate the planar Gunn diode with a micro-cooler. This approach required wafer level integration and hence compatible III-V semiconductor technologies for the fabrication of both devices.

5.1 Design

All device (micro-cooler) wafers measured at De Montfort University were fabricated with the same wafer growth specification. The wafer specification was based on the work of Zhang [48]. The wafer material was grown using molecular beam epitaxy (MBE) by IQE and the material specification is given in table 5.1. The top highly doped GaAs contact layer and the aluminium gallium arsenide (AlGaAs) layers (graded layers and superlattice) made up the mesa for the micro-coolers. The metallised cathode contact was placed on top of the mesa, while the metallised anode contact was on top of the lower highly doped contact layer beside the mesa, as shown in figure 5.1. The micro-coolers were fabricated at the University of Glasgow and the main changes to the coolers were geometry (shape, dimensions, contact layout) and metallisation schemes.

Table 5.1: *Micro-cooler wafer specification used by the University of Glasgow (grown by IQE).*

Material	**Doping level**	**Thickness**	**Notes**
GaAs	8×10^{18} cm^{-3}	300 nm	Contact layer
AlGaAs (Al=0.2-0)	8×10^{18} cm^{-3}	50 nm	
AlGaAs (Al=0.1)	2×10^{18} cm^{-3}	10 nm	Superlattice
AlGaAs (Al=0.2)	2×10^{18} cm^{-3}	10 nm	(100 periods of this)
AlGaAs (Al=0-0.2)	8×10^{18} cm^{-3}	50 nm	
GaAs	8×10^{18} cm^{-3}	300 nm	Contact layer
GaAs	Undoped	100 nm	Buffer layer
GaAs	Semi-insulating	620 μm	Substrate

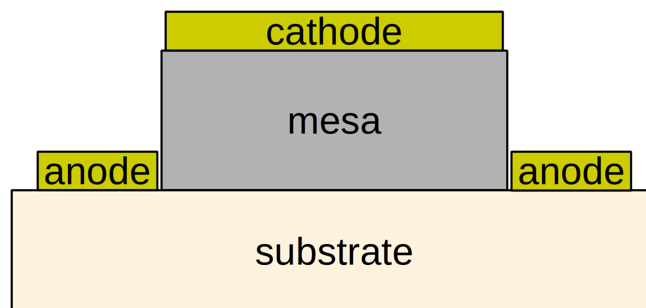

Figure 5.1: *Basic cooler structure, showing cathode contact on top of the mesa and anode contacts off-mesa, to the sides of the mesa.*

The GaAs based wafer was grown using the AlGaAs superlattice to assist in the isolation between the thermal and electrical circuits of the micro-cooler. A GaAs based cooler was required to match the base material for the planar Gunn diode [1; 2] enabling an effective wafer-level integration between the micro-cooler and planar Gunn diode. The most common III-V based semiconductors for fabrication of the planar Gunn diode are GaAs and InP based materials [3; 68; 69; 70]. Glasgow has fabricated a number of iterations of GaAs based planar Gunn diodes [1; 2; 4] and has a well established GaAs based fabrication process. Therefore, GaAs was chosen as the best option base material for a proof-of-concept when considering an integrated micro-cooler. InP based planar Gunn diodes have been fabricated at the University of Glasgow [5], however at the start of this research, the fabrication process for InP based Gunn diodes was not as well established.
The work used a superlattice micro-cooler structure as it provided a number of advantages including, as already stated; acting as a thermal barrier (preventing the flow-back of heat between the heated anode and cooled cathode contacts) and increasing the thermionic cooling (due to the many barriers that the current flow would traverse). Details on the use of a superlattice to aid cooling can be seen in section 2.3.3.

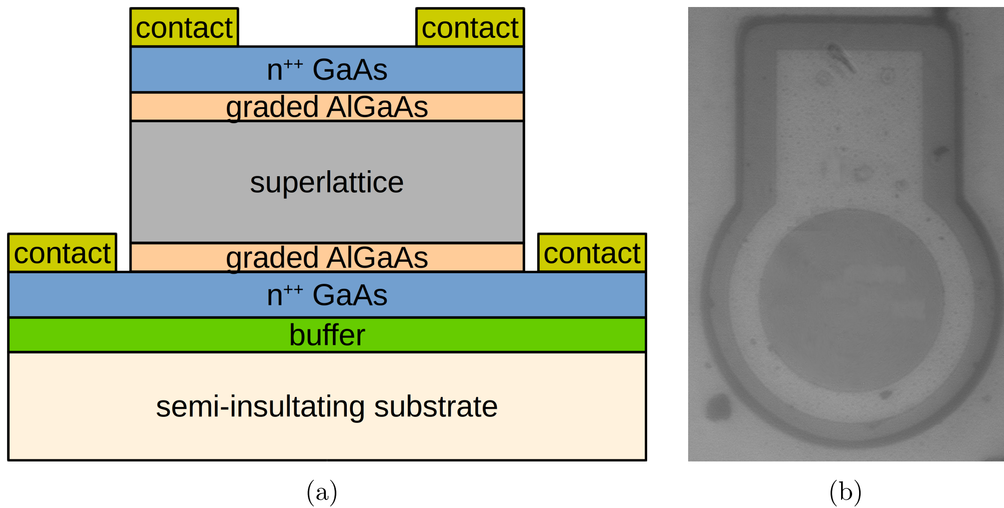

Figure 5.2: *(a) Cross-sectional schematic of the contact geometry (as in table 5.1) and wafer layers for the micro-cooler wafers. (b) Plan-view image of micro-cooler with a round structure and ring-like top contact.*

To enable an active device (for example a planar Gunn diode) to be integrated on top of the micro-cooler, the top layer of the cooler cannot be fully metallised. Therefore, initial micro-cooler designs used a highly doped (8×10^{18} cm^{-3}) GaAs

contact layer and assumed the current will spread uniformly within it before travelling through the cooling layers. It was argued that this would result in uniform cooling across the whole of the top surface of the micro-cooler. For these micro-coolers, the current was fed into the structure via a metallised ring contact (see the schematic and photo in figure 5.2). The unmetallised cathode area, which in future will include the wafer layers required to make up the planar Gunn diode enabling the planar Gunn diode to be integrated with the micro-cooler.

5.2 Electrical measurement techniques

5.2.1 IV characterisation

The IV characteristics of the micro-coolers were measured using the 4-probe technique connected to the semi-automatic IV system described in section 4.3.1. The measured micro-cooler IV characteristic was useful as it gave an indication of the total resistance (R_{tot}) of the cooler, which is needed to estimate the amount of Joule heating (self-heating) within the cooler.
A micro-cooler will generate self-heating in different parts of its structure, for example the electrical contacts and bulk semiconductor regions. To understand this more fully it was necessary to measure the resistance of the electrical contacts. This was undertaken by including structures for the transmission line method (TLM), section 5.2.2, on the wafer to enable an estimation of the specific contact resistivity (ρ_C). The anode and cathode contact resistances were calculated knowing the respective physical contact geometries. Once the contact resistances (R_C) were determined, the bulk resistance of the cooler (R_{SL}) could be calculated by subtracting the bottom anode (R_{BC}) and top cathode (R_{TC}) contact resistances from the measured total cooler resistance (R_{tot}).
A number of micro-coolers with different areas and geometries were measured giving rise to a large variety of observed IV characteristics. Therefore, micro-coolers with both large (6 Ω) and small (0.6 Ω) total resistances (R_{tot}) were measured. The resistance of a device is proportional to the device resistivity (ρ), length (L), and area (A) (equation (5.1)). All the micro-coolers were fabricated on a wafer with the same wafer specification (ρ and L were consistent), enabling the total resistance (R_{tot}) of the micro-coolers to be plotted against device area (figure 5.3). As it was unknown whether the area was defined by either the mesa geometry area (figure 5.3(a)) or the cathode contact metallisation area (figure 5.3(b)), R_{tot} was plotted against both. Similar behaviours can be seen in both plot (a) and (b), showing the expected inversely proportional relationship.

$$R = \frac{\rho L}{A} \tag{5.1}$$

Where R is resistance (Ω), ρ is the resistivity (Ω·m), L is the length (m), and A is the area (m^2) of the material that the current flows through.

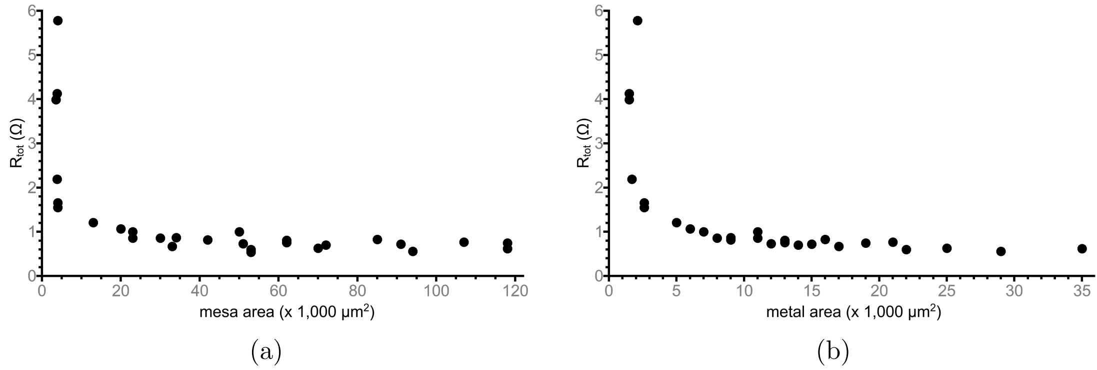

Figure 5.3: *Measured R_{tot} of micro-coolers against; (a) mesa area, and (b) cathode metallisation area.*

5.2.2 TLM measurements

The TLM measurement technique was first reported in 1964 and is based on work performed by W. Shockley [71]. Shockley proposed an experiment where the total resistance (R_{tot}) could be measured between two ohmic contacts (of width, W and length, d) with a gap of ℓ between them. This measurement was repeated a number of times for different gap lengths between the pads, i.e. ℓ_1, ℓ_2, etc. (figure 5.4). The measured total resistance, R_{tot}, is then plotted against ℓ (figure 5.5). The total resistance (R_{tot}) will increase as the gap length (ℓ) increases.

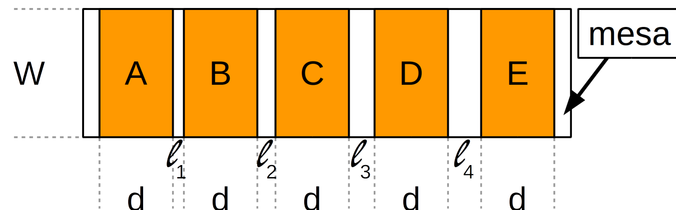

Figure 5.4: *Example TLM contact layout on top of the same mesa as the active device (for contact resistance analysis).*

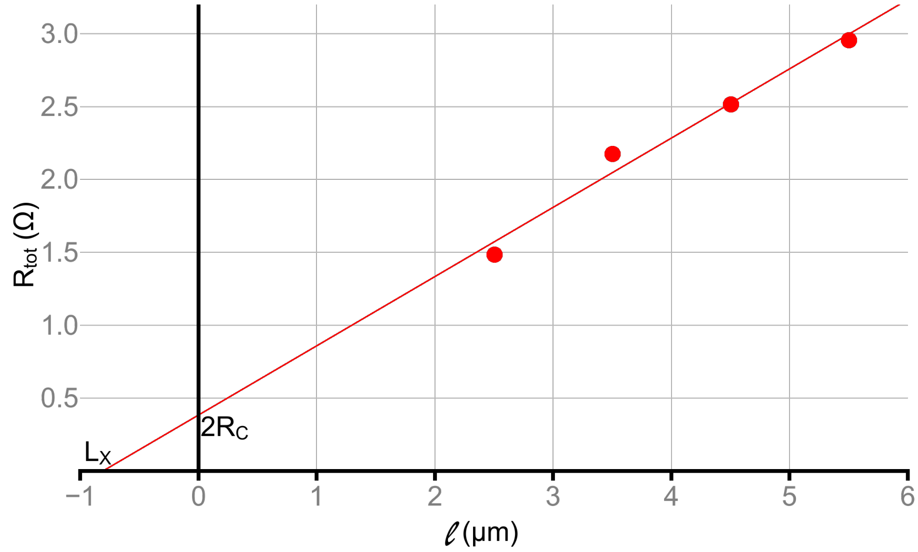

Figure 5.5: *Plot from TLM measurements, showing where the linear relationship intersects the y-axis (2R_C) and the x-axis (L_X).*

As seen from equation (5.1), the resistance ($R = R_{tot}$) is proportional to the length ($L = \ell$) and if the resistivity (ρ) and area (A) are not changing then this will show a linear relationship (as in figure 5.5). Equation (5.1) indicates that when $\ell = 0$, R will also be zero, however, this is not seen in figure 5.5. Therefore, there is additional resistance that is not effected by the gap distance (ℓ). This additional resistance is due to the contact resistance (R_C) of the metallised TLM contacts. As each measured TLM structure contains two contacts, with identical geometries, the total contact resistance will be $2R_C$, as shown in figure 5.5. The point where the trend line intersects the y-axis (when $\ell = 0$) there is no internal resistance (only the two contact resistances, i.e. $2R_C$).

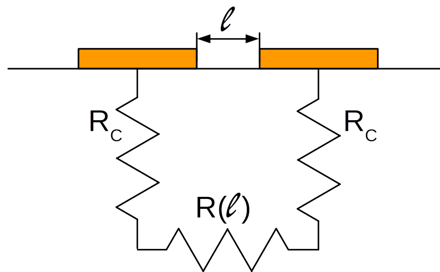

Figure 5.6: *Basic representation of the resistances involved when a current flows between two ohmic contacts.*

Figure 5.6 simplifies the resistances as vertical (contact) and lateral (semiconductor resistance) components. Here it is clear to see that only the lateral resistance, $R(\ell)$, is a function of the gap length, ℓ.
Based on the work from Shockley [71], the product of the resistance (R_C), width (W), and transfer length (L_T) of a contact is the specific contact resistivity (ρ_C), as in equation (5.2).

$$\rho_C = R_C \cdot W \cdot L_T \tag{5.2}$$

Where it is assumed that ρ_C is the inverse of the specific contact conductivity ($\sigma_C = \frac{1}{\rho_C}$) referred to by Shockley [71].

Therefore, to calculate ρ_C the transfer length (L_T) needs to be known. Using the conventional TLM described above, L_T can also be read from the plot of R_{tot} against ℓ (figure 5.5) as $L_X = 2L_T$, where L_X is the point the trend line intersects the x-axis. According to Reeves & Harrison [72], this is due to the sheet resistance of the bulk semiconductor being consistent at different (vertical) distances from the metal contacts (figure 5.7). The sheet resistance (R_{SH}) is the resistance per square ($\Omega/\square$) section of a material, it relates to resistivity of the material as; $R_{SH} = \frac{\rho}{t}$ (where t is the thickness of the material).

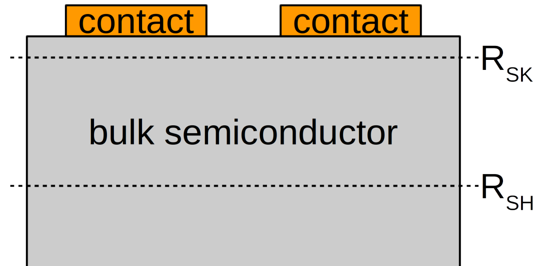

Figure 5.7: *Simple bulk semiconductor structure with two sheet resistances; R_{SH} (sheet resistance deep within the bulk semiconductor) and R_{SK} (sheet resistance directly underneath the contacts).*

Reeves & Harrison state that $L_X = \frac{2R_{SK} \cdot L_T}{R_{SH}}$ [72], so $L_X = 2L_T$ only when $R_{SH} = R_{SK}$. Therefore, with a variation in the sheet resistance with depth (where $R_{SH} \neq R_{SK}$) $L_X \neq 2L_T$.
Applying the TLM to micro-coolers is complicated as the coolers are often fabricated as a superlattice structure. This will give rise to potentially large variations in sheet resistance with depth because of the large number of layers of different materials within a wafer (table 5.1). Therefore, as the thickness of the material changes, the average resistive properties of the material change. Meaning that $R_{SH} \neq R_{SK}$ and so the conventional TLM measurement may not give an accurate ρ_C. Reeves & Harrison [72] reported an alternative TLM for materials where $R_{SH} \neq R_{SK}$ in 1982.

TLM measurement based on Reeves & Harrison's work

Reeves & Harrison [72] showed a different way to calculate L_T regardless of whether $R_{SH} = R_{SK}$, equation (5.3).

$$L_T = \frac{d}{\ln(\Re + \sqrt{\Re + 1}\sqrt{\Re - 1})} \; [72] \tag{5.3}$$

$$\Re = \frac{R_C}{R_E}$$

Where d is the length of the TLM contact (as seen in figure 5.4) (m), R_C is the contact resistance (of each TLM contact) (Ω), and R_E is the contact end resistance (Ω) (as named by Reeves & Harrison [72]).

To be able to calculate L_T, R_E needs to be known. This can be obtained by taking an additional set of measurements as well as the conventional TLM measurements.

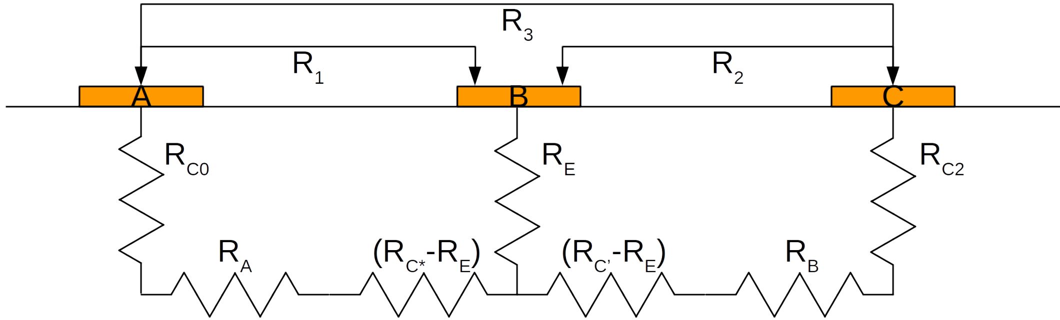

Figure 5.8: *Representation of the resistances involved when a current flows between two ohmic contacts, showing the additional* R_E *[72].*

Figure 5.8 shows a more complex electrical resistance model [72]. Conventional TLM measurements can be used to measure the resistance between neighbouring contacts (with a known gap between them), such as the resistances between contacts A & B (R_1) and B & C (R_2) in figure 5.8. The equations below show how measuring an additional resistance (between contacts A & C), R_3, enables the calculation of R_E.

$$R_1 = R_{C0} + R_A + R_{C*} \tag{5.4}$$

$$R_2 = R_{C'} + R_B + R_{C2} \tag{5.5}$$

$$R_3 = R_{C0} + R_A + R_{C*} + R_{C'} - 2R_E + R_B + R_{C2} \tag{5.6}$$

and therefore:

$$R_E = \tfrac{1}{2}(R_1 + R_2 - R_3) \; [72] \tag{5.7}$$

R_{C0}, R_{C*}, R_E, $R_{C'}$, and R_{C2} are components of contact resistance and if $R_{SH} = R_{SK}$ then all 5 should be equal to the R_C measured using the conventional TLM. However, if $R_{SH} \neq R_{SK}$ then the calculated R_E (and R_C from the conventional TLM) can be used with equation (5.3) to calculate L_T. Hence, equation (5.8) can be used to calculate ρ_C.

$$\rho_C = R_E \cdot W \cdot L_T \cdot \sinh\left(\frac{d}{L_T}\right) \quad [72] \tag{5.8}$$

Results

All the grown wafers for the fabrication of micro-coolers were analysed using the transmission line method (TLM) and two (5th and 6th micro-cooler fabrication iterations) were analysed using the Reeves & Harrison TLM. A comparative plot is shown in figure 5.9.

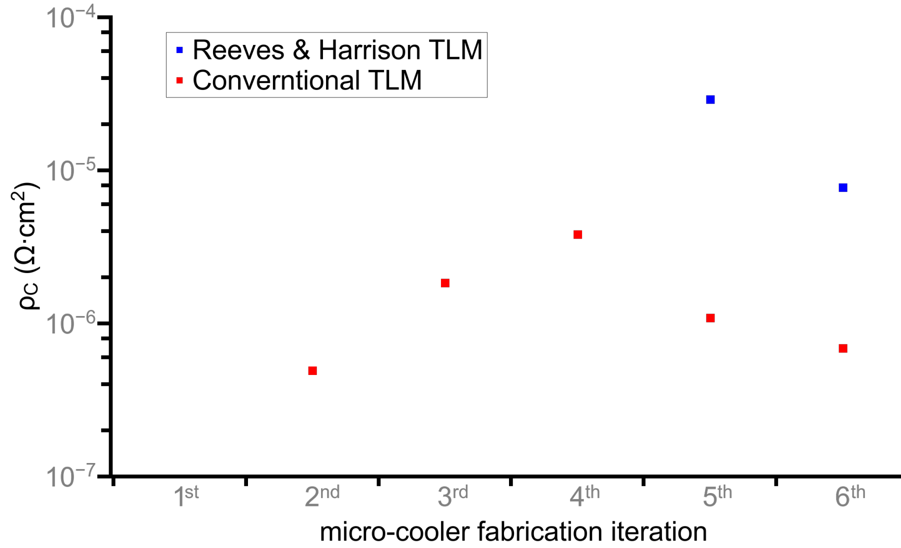

Figure 5.9: *Comparison of specific contact resistivity (ρ_C) for all 6 micro-cooler fabrication iterations analysed at De Montfort University, including conventional and Reeves & Harrison TLM comparisons on the later wafers (1st iteration was discounted due to Schottky contacts, figure 5.10).*

Figure 5.9 shows the specific contact resistivities (ρ_C) using the conventional TLM were in the region of 0.5 to 6 $\times 10^{-6}$ $\Omega\cdot cm^2$, while analyses using the Reeves & Harrison TLM (only the 5th and 6th wafer iterations) show ρ_C between 1 & 3 $\times 10^{-5}$ $\Omega\cdot cm^2$. The results indicate that the Reeves & Harrison TLM

gave a specific contact resistivity around 10 to 30 times greater than the conventional TLM. If contact resistances were calculated using the conventional TLM, they would be small and most of the total resistance (R_{tot}) of the micro-cooler would be from the bulk semiconductor region (R_{SL}). While contact resistances calculated using the Reeves & Harrison TLM would be far greater, reducing the resistance associated with the bulk semiconductor region (R_{SL}).
It should be noted that there is no ρ_C for the 1st micro-cooler fabrication iteration in figure 5.9. This is because the contacts on this micro-cooler fabrication iteration appeared to be Schottky contacts rather than ohmic contacts. Using the TLM measurement ohmic contacts will give a linear response enabling the contact resistance value (R_C) to be obtained. Whereas a Schottky contact will provide a non-linear response. Figure 5.10 shows the IV characteristic for all four TLM contact separations (ℓ) measured on the 1st micro-cooler wafer iteration.

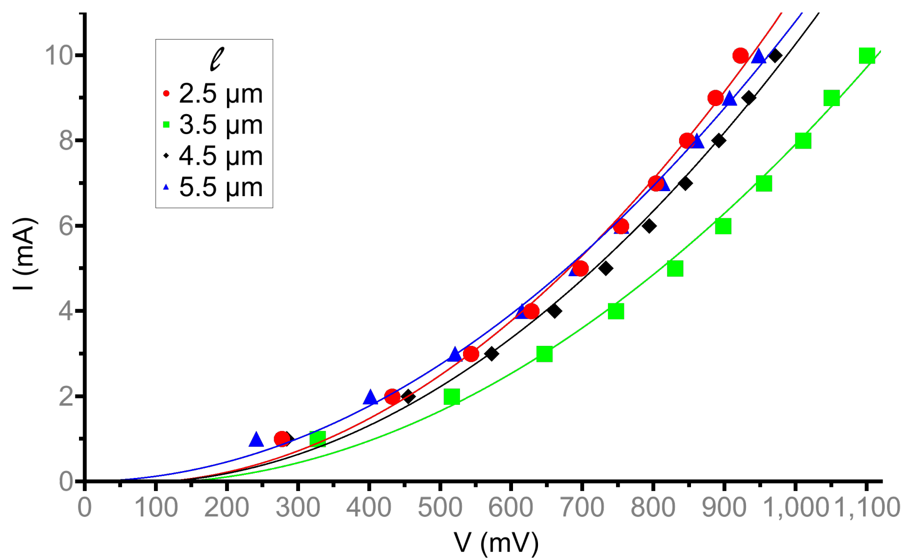

Figure 5.10: *IV characteristics, showing Schottky contact behaviour. For four TLM pad separation distances (ℓ) measured on the* 1st *micro-cooler wafer iteration.*

It was assumed that the specific contact resistivity (ρ_C) from the Reeves & Harrison TLM will give a more accurate representation for the micro-cooler wafers, as the method takes into account the layered semiconductor structure. Therefore, the range of ρ_C (1 to 3 $\times 10^{-5}$ $\Omega{\cdot}cm^2$) was used to estimate the contact resistances (R_{TC} & R_{BC}) and bulk semiconductor resistance (R_{SL}) of the micro-coolers. These resistances were used to model the self-heating effects in the micro-cooler. The effects include separate regions of self-heating in the contacts and bulk semiconductor regions. More details on computer simulations carried out on the micro-coolers will follow in chapter 6.

5.3 Thermal measurement techniques

Micro-coolers are devices with small total areas (the order of 10,000 μm^2) and operate with large thermal power densities (the order of 800 W/m^2). This will result, for a GaAs based micro-cooler, in a small temperature difference between the anode and cathode contacts (∼1 °C). Therefore, accurate temperature measurements will be required to observe the temperature difference (ΔT) between the anode (T_h) and cathode (T_c) contacts. As there will be a very small ΔT, both anode and cathode temperatures need to be measured under exactly the same micro-cooler bias conditions. Therefore, both anode and cathode contact temperatures need to be measured at the same time. The requirement to measure the temperature of both the anode and cathode at the same time, as well as having good measurement accuracy led to using the high emissivity micro-particle sensor technique, as described in chapters 2 (section 2.1) and 3. The technique requires a micro-particle to be placed on both the anode and cathode contacts and for both micro-particles to be imaged simultaneously using the QFI IR thermal microscope. This requirement put a restriction on the separation between the micro-particles and therefore the separation of the anode and cathode electrodes to around 500 μm, the maximum field of view of the QFI InfraScope using the ×25 objective lens.

As already described (in chapter 3) the micro-particle sensor, micro-manipulator, and optical grid have been combined to enable more accurate thermal measurements to be made using the QFI IR thermal microscope. The micro-particle technique is not dependent on the surface emissivity of the material, but only on the surface emissivity of the micro-particle. The micro-particles are calibrated before the measurement by measuring the emitted radiance as a function of their surface temperature.

Micro-particle sensors were needed for making a temperature measurement on the micro-cooler contacts because the gold contacts have a very low surface emissivity (∼0.1). If conventional IR measurements were used, the low emissivity contacts would give a noisy radiance signal, making it difficult to get an accurate temperature measurement. The high emissivity of the micro-particle (∼0.6) will enable more accurate temperature measurements to be made. Calculations and subsequent measurements suggested that temperature differences between the anode and cathode contacts could be as small as 0.1 °C. Figure 5.11 shows an example of the thermal measurement technique, showing both the temperature and the radiance plots for micro-particles placed next to the metallisation edge of both the cathode (T_c) and anode (T_h) regions.

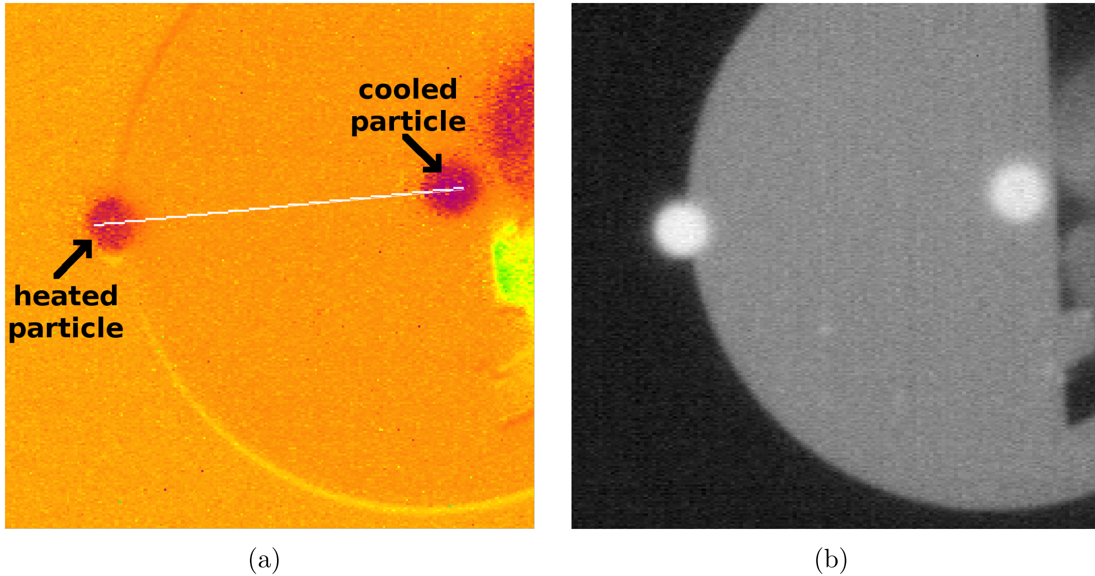

Figure 5.11: *Temperature comparison between two micro-particle sensors, on different device contacts ((a) temperature plot and (b) radiance plot).*

As the micro-particle sensor enabled IR thermal measurements to be made regardless of the emissivity of the material upon which it was placed, the micro-particle sensor can also be used to make temperature measurements on the semiconductor regions of the micro-cooler where the surface emissivity can not be characterised, due to the transparency of the semiconductor (GaAs) to IR radiation (section 2.1.3).
A number of micro-coolers with different geometries and contact metallisation schemes were measured. The micro-cooler variations included the cathode, mesa, and anode geometries, as well as the use of semi-insulating and conductive substrates. These are schematically summarised in table 5.2 (coolers on a conductive substrate had no metallised anode contact as this was located on the backside of the wafer). A colour-coded legend can be seen at the bottom of the table. It was very difficult to make a good electrical contact to the anode contact when a conductive substrate was used. For this reason all reported measurements made in this research were made on micro-coolers with semi-insulating substrates.
The micro-cooler geometrical design variations were determined by the etching and metallisation fabrication processes. Therefore, variations in anode, cathode, and mesa geometries (including variations in the percentage of the mesa covered by the cathode contact), as well as whether the cooler was grown on top of a semi-insulating or conductive substrate were available for measurement and analysis. Most published work on micro-coolers have shown a preference

Table 5.2: *Selection of micro-cooler geometries and contact metallisations.*

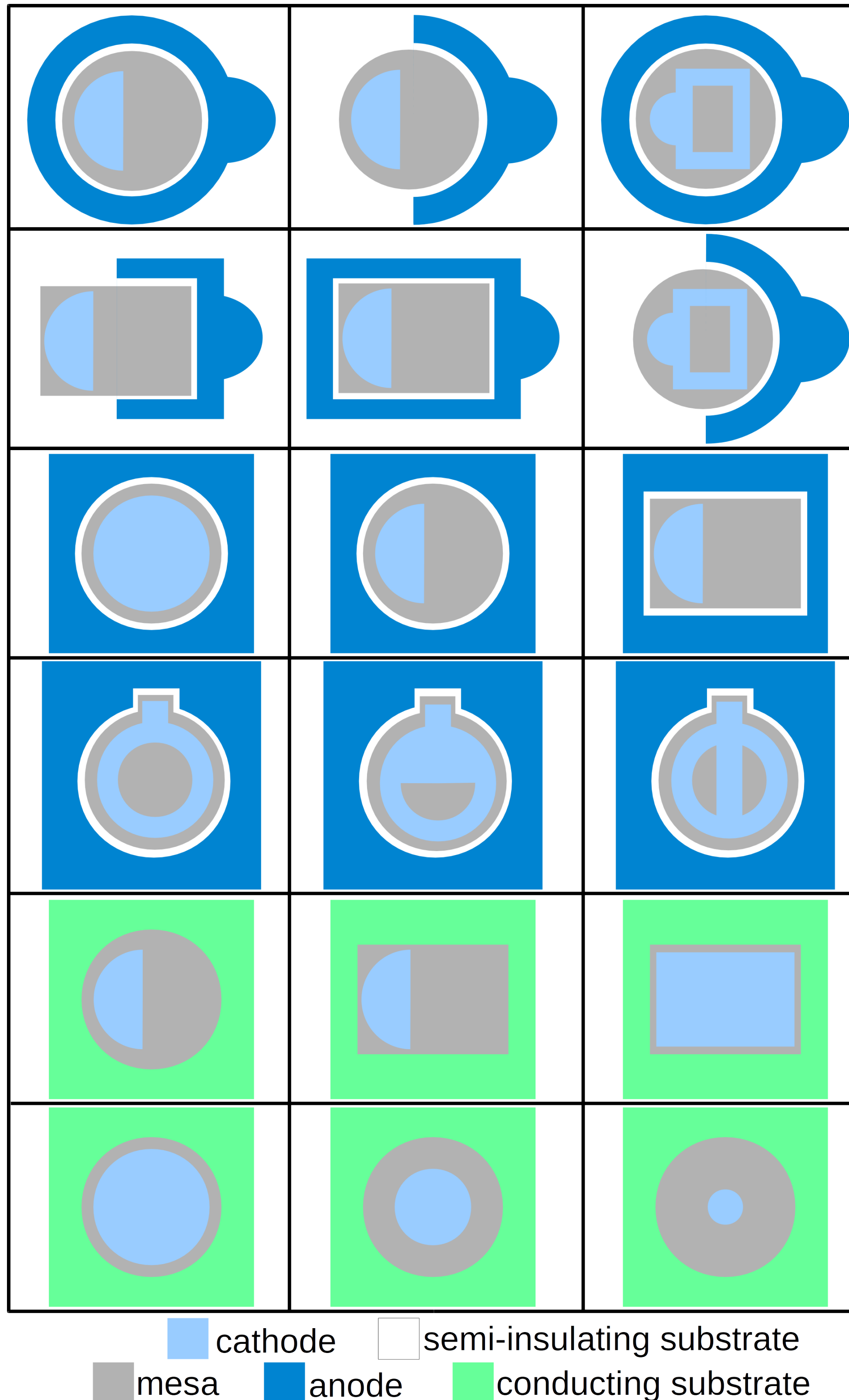

for small area devices [73; 74], with an optimal area (between 1,600 μm^2 and 6,400 μm^2) [43; 48; 75] to increase the maximum ΔT between the anode and cathode contacts. The published papers also considered a variety of different cooler materials; AlGaAs superlattice, bulk AlGaAs, InGaAs/InAlAs superlattice, InGaAs/InGaAsP superlattice, and Si/SiGe superlattice. However, all of the published coolers have had the entire mesa area metallised, therefore it was unclear if the mesa geometry or the cathode geometry was a defining factor to the cooling performance.

Cooling performance of micro-coolers can be analysed over a large range of bias conditions. Y. Zhang et al. [41] reported a maximum ΔT occurring at a bias current of 80 mA, while Litvinovitch et al. [74] reported a maximum ΔT at a bias current of over 800 mA. J. Zhang et al. [48] reported (for an AlGaAs superlattice micro-cooler) currents between 120 and 350 mA for a maximum ΔT (dependent on the cooler area). Therefore, the fabricated micro-coolers in this research were thermally analysed over a very large current range, for example device B14 (figure 5.12) was analysed from 0 to 900 mA (figure 5.13).

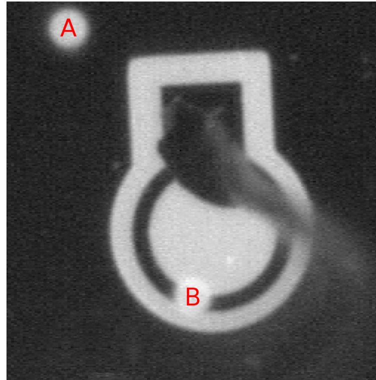

Figure 5.12: *Micro-cooler B14 with a central (ring-like) cathode and surrounding anode. Two micro-particle sensor temperatures were measured, where particle A was on the anode and B was on a metallised cathode ring.*

The micro-cooler B14 is shown in figure 5.12 along with a probing connection at the top of the cathode contact and two micro-particle sensors (A and B). The temperature difference (ΔT) was taken between the anode (T_h, particle A) and the cathode (T_c, particle B). Figure 5.13 shows very little temperature variation (between the two micro-particles) at low bias conditions and high self-heating at high bias conditions.

The ΔT behaviour observed for cooler B14 (figure 5.13) suggested the micro-coolers only need to be observed at relatively low current conditions (up to 300 mA). This enabled small variations in ΔT to be more easily resolved. Figure 5.14(b) shows a micro-cooler (B9) with a cathode area (the right of the

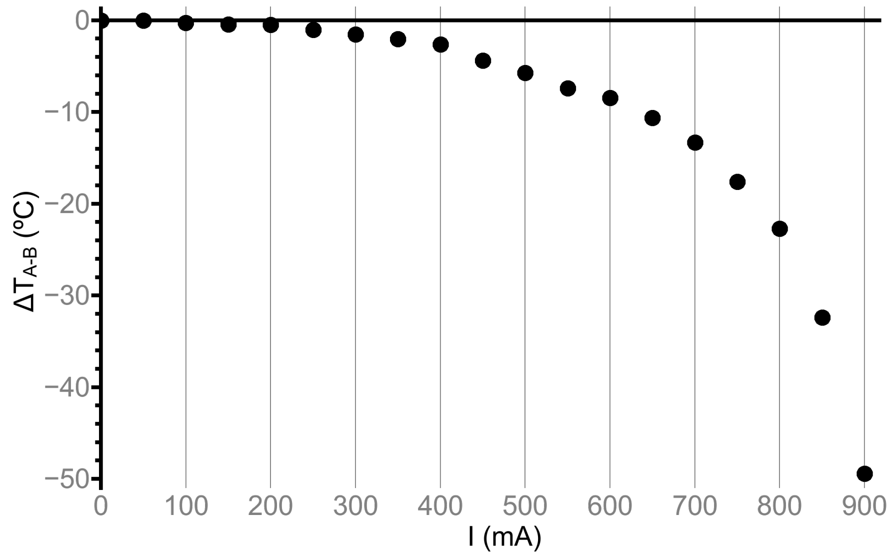

Figure 5.13: *Thermal analysis of B14 (figure 5.12), considering ΔT between particles A and B.*

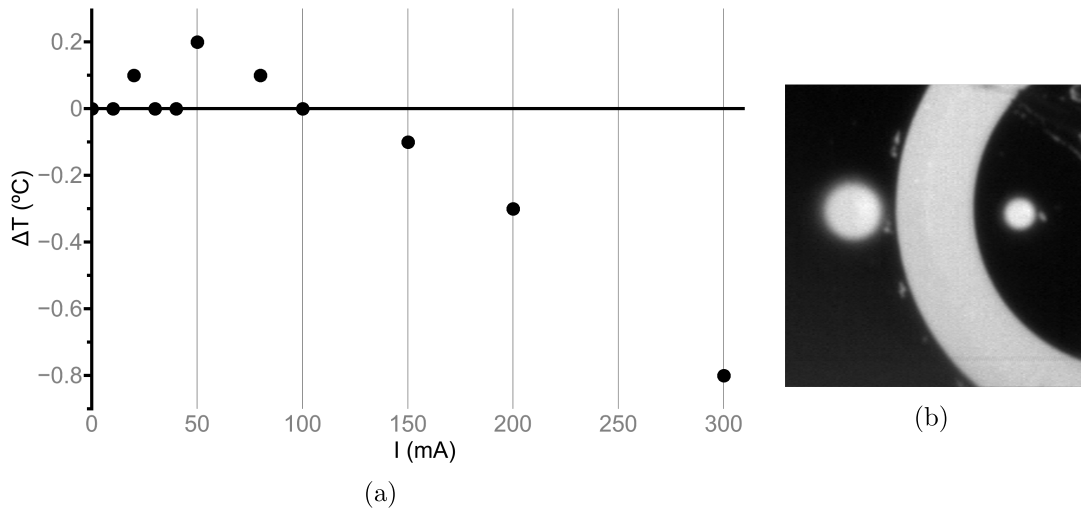

Figure 5.14: *(a) Thermal analysis of ΔT between the micro-particle sensors on the anode and cathode contacts of cooler B9, seen in insert (b).*

image), which was greater in area than the field of view available by the QFI InfraScope II with the ×25 objective. As micro-cooler B9 showed small signs of cooling (figure 5.14(a)) and published literature suggested that smaller devices will outperform large area devices [48; 73; 75], a micro-cooler smaller than B9 was tested.

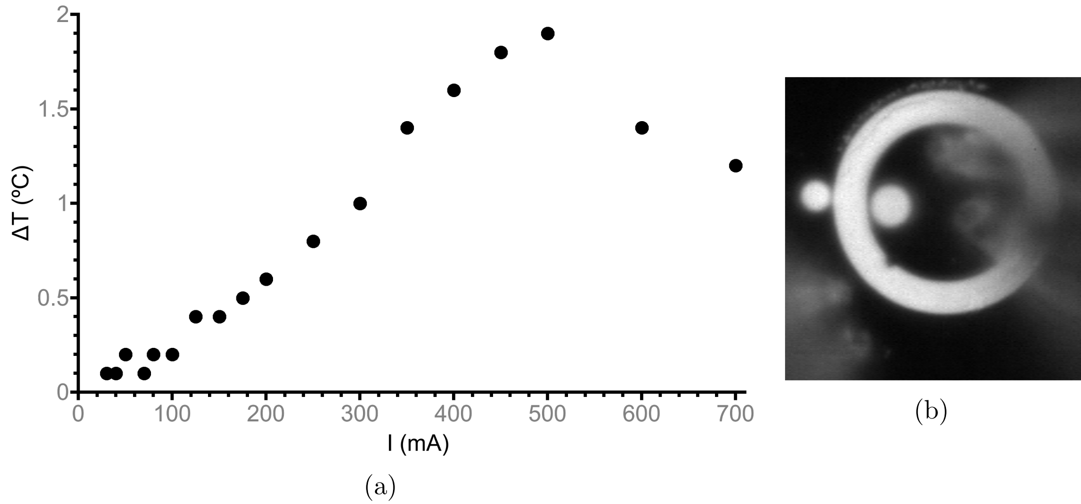

Figure 5.15: *(a) Thermal analysis of ΔT between the micro-particle sensors on the anode and cathode contacts of cooler A9, seen in insert (b).*

In figure 5.15(a), the micro-cooler A9 with a smaller area (metallised cathode area, ~12,300 μm^2) showed cooling. The micro-cooler was measured to higher current bias conditions to ascertain the point when the cooling performance would start to reduce. It appeared the optimum cooling performance (ΔT) was almost 2 °C at 500 mA. This level of cooling was 100% higher than reported in the published literature for a similar GaAs based micro-cooler with an AlGaAs superlattice [48], in which the author published a maximum ΔT of 0.8 °C at 200 mA. The above experimental results suggested that an improved cooling performance had been obtained or the experiment was giving an anomalously high ΔT. One possibility was thermal loading from the bias probes; as the micro-cooler was small and the bias probes were in very close proximity to the micro-particle sensors. It is well known that there is a resistance between the probe tip and the micro-cooler metallised contact, giving rise to extra self-heating at this interface and contributing to the hot anode contact. This could give an anomalous ΔT result. Experimental methods were developed to test the hypothesis.

5.3.1 Thermal analysis of thermal loading

An experiment was devised to look at the temperature difference between the two contacts (anode and cathode). It used two 10 μm diameter micro-particles positioned on the ohmic contacts of a TLM structure. However, one of the micro-particles was positioned slightly closer to the bias probe than the other. The TLM structure was used as it is a simple reciprocal structure. The TLM pads were 150×150 μm with a 2.5 μm gap between them. Figure 5.16 shows the micro-particles placed on either side of the gap, towards the top edge of the contacts.

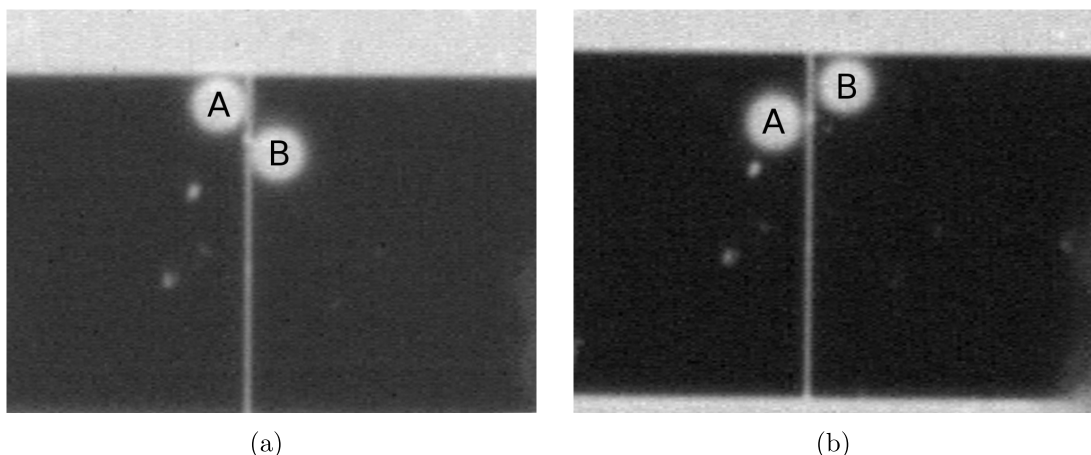

(a) (b)

Figure 5.16: *Micro-particle sensors placed on neighbouring TLM contacts to check for thermal loading from the DC probes (placed on diagonally opposite corners of the contacts), where (a) particle B is slightly closer to the probes and (b) particle A is slightly closer to the probes.*

In figures 5.16(a) & (b), it can be seen that (in each subfigure) there are two micro-particle sensors A and B on the left and right contacts respectively. Initially, micro-particle A was placed in the top-right corner of the left contact, while micro-particle B was on the left-edge, but slightly lower (~10 μm) from the top-edge of the right contact (figure 5.16(a)). The biasing probes were placed as far away from the micro-particles as possible, diagonally opposite corners of each contact (the bottom-left and bottom-right corner of the left and right contacts respectively). The device was then biased from 0 to 450 mA (in both forward and reverse bias) and the corresponding temperature difference (ΔT) between the particles was measured, figure 5.17. For the forward bias (displayed as a positive current) micro-particle A (left contact) was on the anode (T_h) and micro-particle B (right contact) was on the cathode (T_c), ΔT was calculated as $T_h - T_c$.

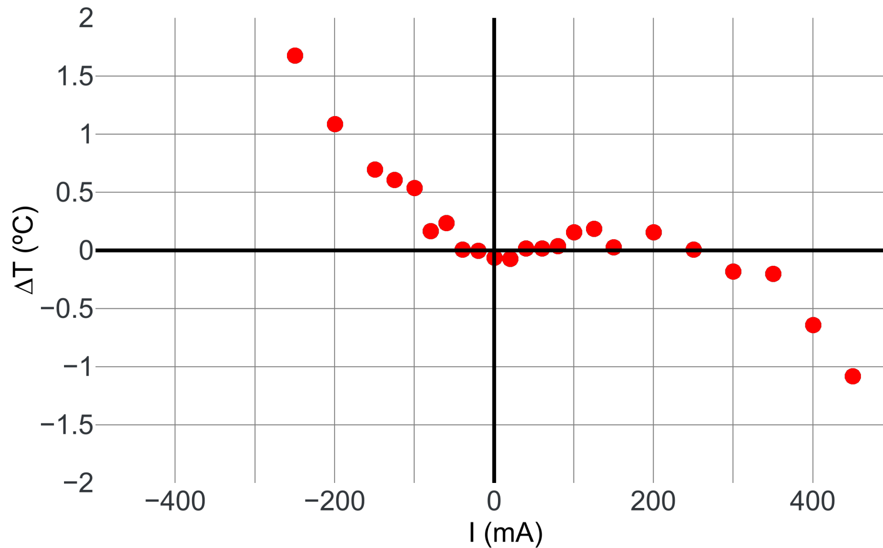

Figure 5.17: *Measured temperature difference (ΔT) against bias current when particle B was closer to the bias probes (figure 5.16(a)).*

To ascertain whether the observed ΔT was changed by the proximity of the micro-particles to the bias probes, particle A was moved closer to the probe (further down the right-edge of the left contact), while particle B was moved further from the probe (into the top-left corner of the right contact), figure 5.16(b). The device was biased as before and thermally measured, figure 5.18.
Comparing figures 5.17 & 5.18, it was found figure 5.18 was a mirror of figure 5.17. However, the current direction was kept in the same sense for both sets of tests, the only difference was which of the micro-particles was closer to the bias probes. The micro-particle closer to the bias probes was heating-up more than the micro-particle further from the bias probes. Suggesting that the probes are thermally loading the contacts of the TLM test circuit. Therefore, this simple experiment showed that the bias probes will thermally load the micro-cooler if they are too close. Thermally isolating the micro-cooler contacts will be beneficial when measuring the cooling performance of the micro-coolers.
The above experimentally confirmed that the bias probes will thermally load the micro-cooler, however it was not known whether the thermal loading of both the anode and cathode contacts of the micro-cooler will be equal or the thermal loading of one contact will dominate.

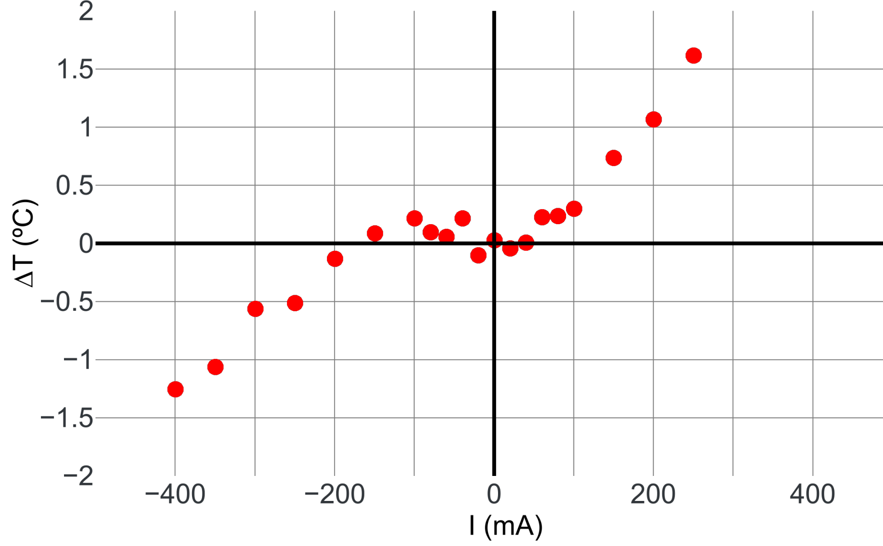

Figure 5.18: *Measured temperature difference (ΔT) against bias current when particle A was closer to the bias probes (figure 5.16(b)).*

5.3.2 Analytical analysis of thermal loading

The previous experimental work showed that the bias probes will thermally load small area contacts if the probes are positioned on those contacts. This finding was applied to the measurement and simulation of small area micro-coolers. The operation of the micro-cooler requires a current (I) to pass through the cooler to transfer heat from the cathode to anode contact. In simple terms, the amount of heat transferred is proportional to the magnitude of the current flowing. The current flow also results in self-heating within the micro-cooler structure. The self-heating is proportional to I^2 (equation (2.5)) and so micro-coolers only provide cooling (positive values of $\Delta\mathrm{T}$) when the self-heating is less than the cooling effect. This can be described using the equation below:

$$\Delta\mathrm{T} = \Theta\left(\mathrm{SIT_c} - \mathrm{RI}^2\right) \quad (2.5)$$

Where $\Theta\mathrm{SIT_c}$ is the temperature cooling component and $\Theta\mathrm{RI}^2$ is the temperature self-heating component (Θ is the thermal impedance of the cooler (K/W), S is the bulk Seebeck coefficient of the cooler materials (V/K), $\mathrm{T_c}$ is the temperature of the cooled cathode contact (K), and R is the total resistance of the cooler (Ω)).

However, in an experimental set-up there is self-heating both within the micro-cooler and the contact resistance between bias probes and cooler contacts.

The self-heating of the micro-cooler will increase the temperature of the whole micro-cooler (internal and contact temperatures). However, the self-heating due to the bias probes will only increase the temperature at the contacts (both the anode and cathode contact areas). As stated above, the self-heating within the micro-cooler is proportional to both I^2 and R (where R can be assumed as the total cooler resistance, including contact resistances), if the contact resistance of both the anode and cathode are equal, then the self-heating of both contacts will be equal. However, if the contact resistances are not equal, then the self-heating of each contact will differ. The contacts of the fabricated micro-coolers will have different contact resistances due to their different geometries, for example the additional lateral resistance of the anode contact. When the contact resistance of both the anode and cathode contacts are equal then both the anode and cathode will heat-up equally and will have a negligible effect on the observed ΔT. However, if the cathode has a greater contact resistance than the anode, the cathode will heat-up more than the anode, suppressing the observed ΔT. If the anode has a greater contact resistance than the cathode, the anode will heat-up more than the cathode, exaggerating the observed ΔT, which could be interpreted as cooling. Any of these situations may not be clearly identifiable from the thermal measurement of micro-coolers on-wafer.
Therefore, a method was developed to interpret whether ΔT was a genuine cooling result or an effect from non-uniform probe heating. Equation (2.5) was rearranged into the form of $y = mx + c$:

$$\frac{I^2}{\Delta T} = \frac{ST_c}{R} \cdot \frac{I}{\Delta T} - \frac{1}{R\Theta} \quad [8] \tag{5.9}$$

Equation (5.9) shows that the gradient (m) of a plot of $\frac{I^2}{\Delta T}$ against $\frac{I}{\Delta T}$ should equal $\frac{ST_c}{R}$. Since, S, T_c, and R can only have positive values, the gradient must also be positive (all published values for the Seebeck coefficient (S) of similar semiconductors are positive). Therefore, any micro-cooler following the behaviour described by equations (2.5) & (5.9) would show a proportional relationship between $\frac{I^2}{\Delta T}$ and $\frac{I}{\Delta T}$ [8].
The thermal measurement and analysis was applied to cooler A9 (as shown in figure 5.15(b)). Figure 5.19 shows an experimentally promising cooling result, where ΔT was greater than 1.0 °C with an applied cooler current of 300 mA. The measurement was made at an operating temperature of ~130 °C. The $\Delta T > 1$ °C cooling for the AlGaAs superlattice micro-cooler was higher than any reported measurement in the literature [48]. Further, the magnitude of ΔT showed evidence of continuing to increase with bias current.
Figure 5.15(b), shows the construction of the A9 cooler, it was a simple structure and the geometry did not allow the bias probes to be thermally isolated from the cooler. The experimental results (figure 5.19) were plotted using equation (5.9).

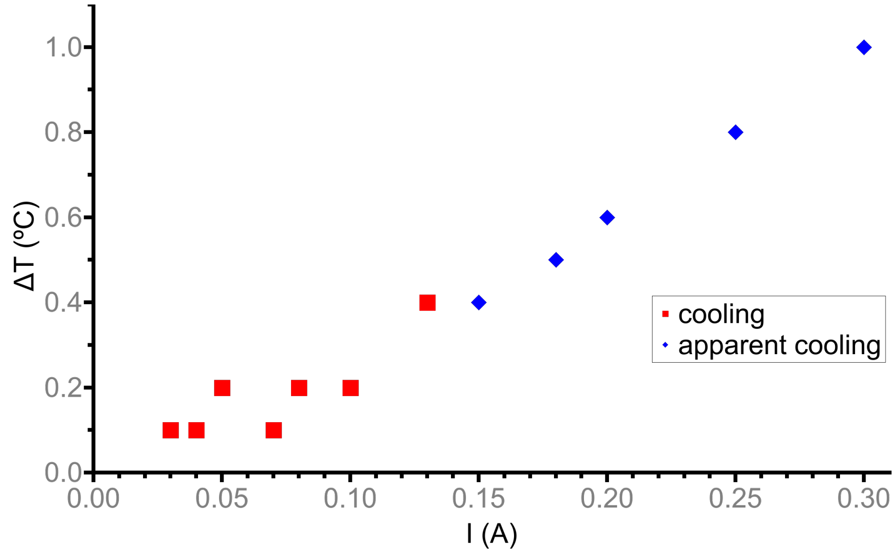

Figure 5.19: *Cooler A9 appearing to show exceptional levels of cooling at an operating temperature of 130 °C [8].*

Two separate gradients were observed (figure 5.20), one positive and one negative. The experimental results giving rise to the positive gradient (7 lowest bias conditions) followed the behaviour of equation (2.5), where only the cooling and self-heating effects of the cooler have an effect on the cooling performance. However, the negative gradient (the experimental points due to the higher bias conditions) do not follow this behaviour. These bias conditions have some additional thermal effect taking place that is not accounted for by equation (2.5). This can be interpreted as the thermal loading from the bias probes. Therefore, the highest bias conditions can be ignored as their observed cooling is anomalous. The results indicated that the maximum cooling of device A9 was ∼0.4 °C at ∼135 mA, this was similar to previously published results [48].
Further experiments were undertaken to verify the above analysis. Micro-cooler (H11 in figure 5.21) was assembled, where the cathode contact was thermally isolated using an external probe pad. This pad was an alumina stand-off bonded to the micro-cooler cathode by a 0.7 thou diameter gold bond wire giving good thermal isolation (figure 5.21). The H11 micro-cooler had a ring-like metallised cathode contact (where A9 had a solid circular, metallised cathode contact) and a notch built into the circular mesa (figure 5.21). The notch was an ideal location for adhesively bonding to the alumina stand-off. Otherwise, the geometry of micro-cooler H11 was similar to that of the A9 micro-cooler. Only the cathode contact was thermally isolated because the anode contact was a very large metallised area (shared between all micro-coolers on the same wafer, as shown

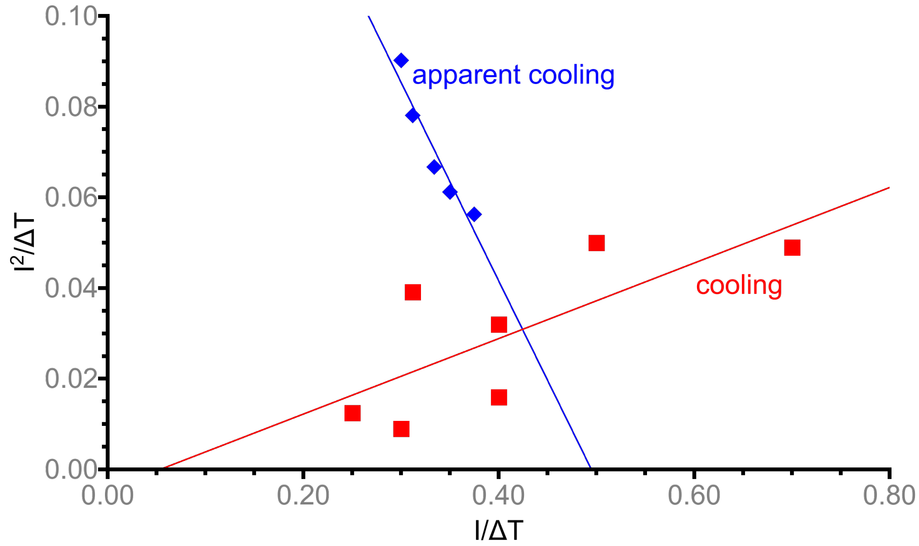

Figure 5.20: *Analysed plot showing that the higher current points do not fit with the conventional behaviour, the bias probes are adding additional heat to the system [8].*

in figure 5.21). Therefore, the positive bias probe was placed a long distance from the active micro-cooler. Any heat generated due to the anode probe contact resistance will spread-out and have a negligible effect on the measured anode temperature. The micro-particle sensor on the anode was placed next to the anode edge, while the positive bias probe was placed >100 μm from the active cooler area.

Cooler H11 from figure 5.21 was biased, thermally measured using the micro-particle sensors, and the results were plotted using equation (5.9) to give the results shown in figure 5.22. This shows that the thermally isolated cooler always shows a positive correlation between $\frac{I^2}{\Delta T}$ and $\frac{I}{\Delta T}$, as would be expected for normal cooler behaviour.

Figure 5.22 shows a positive correlation when both; the cooling was greater than the self-heating of the micro-cooler (positive ΔT) and when the self-heating was greater than the cooling (negative ΔT).

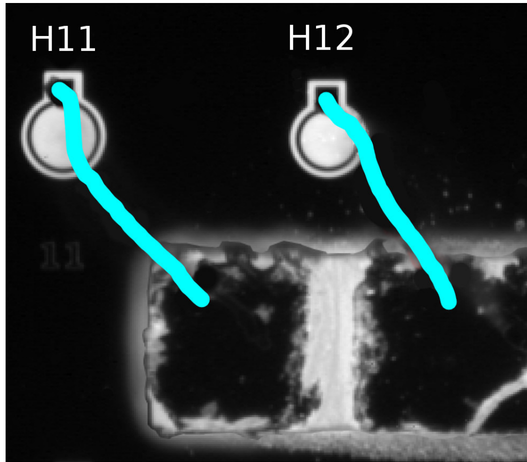

Figure 5.21: *Micro-coolers (H11 & H12) with thermally isolated cathodes via bond wires (displayed in blue) to probe pads on an alumina stand-off.*

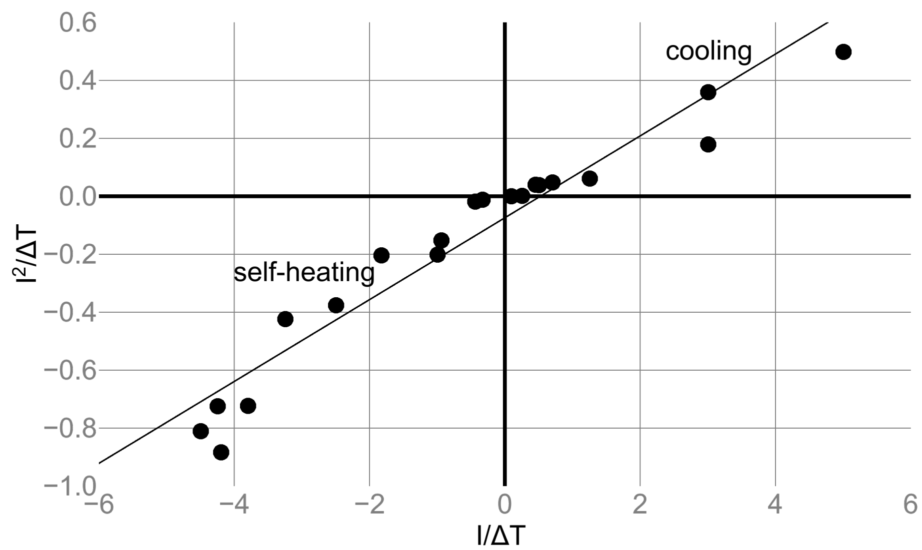

Figure 5.22: *Analysis on the thermal results from a thermally isolated H11 cooler, showing that when heat from the bias probes can be neglected the results do match the expected behaviour [8].*

5.4 Summary

A number of important points were raised in this chapter, including:

- A detailed procedure to calculate the specific contact resistivity (ρ_C) for wafers with a complex layer structure (for example the superlattice in the micro-cooler) has been described. This method was based on a TLM measurement technique published by Reeves & Harrison [72]. The calculated contact resistances for fabricated micro-cooler wafers have enabled the generation of micro-cooler models, which consider self-heating of the independent contacts and the bulk semiconductor region.

- A novel comparative micro-particle IR thermal measurement technique has been described. This was used to measure both the anode and cathode contact temperatures of micro-coolers at the same time, under identical bias conditions using a single thermal measurement.

- The potential problem of bias probes thermally loading small-scale wafer-bound micro-coolers has been verified. Therefore, micro-coolers require thermally isolated contacts to achieve the highest accuracy of thermal measurement. This problem has not been reported before as the author believes these to be the first micro-coolers tested on-wafer.

- If micro-cooler contacts are not thermally isolated, thermal measurements can be made and an analysis has been described that shows whether measured ΔT cooling is anomalous.

- Current micro-cooler geometries will have different anode and cathode contact resistances. This may give rise to problems with non-uniform self-heating of the contacts, which could either suppress or exaggerate the measured ΔT cooling (depending on which contact resistance was higher). This requires additional research.

- Only one micro-cooler wafer specification was fabricated (Ensemble Monte Carlo models carried out by a collaborative team at the University of Aberdeen suggested semiconductor layer thickness changes (increasing the thickness of the graded AlGaAs layers) could improve cooling in a micro-cooler structure [76; 77]).

Chapter 6

Simulations and optimisation of micro-cooler designs

There are potentially a large number of different designs of micro-coolers using a variety of material geometries. Fabricating and measuring all these potential designs would be prohibitively high in cost and time, therefore many cooler designs and options were only considered using computer simulation. The use of simulations gave the ability to run many wafer variations including changes in doping and numbers of semiconductor layers, which would have been very expensive to fabricate and test. Simulations also allowed for a faster turn-around of results. The turn-around time for the fabricated, experimental micro-cooler devices was many months compared to hours for simulations.
Initially, a simple 1D model was explored to represent the basic performance of the micro-cooler. As most published micro-coolers are vertical structures, the work presented here started with a simple vertical structure, where the vertical current flows through the mesa. An important factor in the simulation work was to have a realistic value for contact resistance (dependent on the contact metal combination, semiconductor, and annealing process). In this work the specific contact resistivity (ρ_C) for different metallisation schemes, semiconductor wafers and annealing processes were experimentally measured using transmission line method (TLM) structures, fabricated on supplied micro-cooler wafers. These wafers were supplied by the University of Glasgow. A description and the results of the TLM measurements can be found in section 5.2.2.

6.1 1D Model to match literature results

The 1D model was written (utilising published equations from multiple sources) and verified by reproducing a set of published III-V based micro-cooler results. The work chosen to reproduce was originally published by Shakouri et al. from the University of California [49; 78]. These papers were chosen as they gave a very complete set of cooler performance results, based on heat-flow equations and junction material properties. These enabled the development of a 1D model to reproduce the cooler performance results shown in the publications. The cooler device Shakouri et al. published was based on a III-V (InGaAsP) micro-cooler and was similar in material properties to the AlGaAs used in this research.
The reported equation focuses on the net cooling power density of the micro-cooler (Qd), measured in W/cm^2. Where Qd is a combination of the cooling power density (Qd_t), Joule (self-heating) heating power density (Qd_{jh}), and heat conduction (flow-back heat) power density (Qd_{hc}) in the form:

$$Qd = Qd_t - Qd_{jh} - Qd_{hc} \tag{6.1}$$

$$\text{Where:} \quad Qd_t = \left(\phi + \frac{2k \cdot T_c}{q}\right) J \quad [49]$$

$$Qd_{jh} = J \cdot V \left[\frac{1}{2} - \frac{\lambda_E}{d_B} - \frac{\lambda_E^2}{d_B^2}\left(e^{\frac{-d_B}{\lambda_E}} - 1\right)\right] \quad [49]$$

$$Qd_{hc} = \frac{\kappa \cdot \Delta T}{d_B} \quad [49]$$

$$\therefore \; Qd = \left(\phi + \frac{2k \cdot T_c}{q}\right) J \; - \; J \cdot V \left[\frac{1}{2} - \frac{\lambda_E}{d_B} - \frac{\lambda_E^2}{d_B^2}\left(e^{\frac{-d_B}{\lambda_E}} - 1\right)\right] \; - \; \frac{\kappa \cdot \Delta T}{d_B} \tag{6.2}$$

Where ϕ is the cooler junction barrier height (eV), k is the Boltzmann constant (J/K), T_c is the temperature of the cold contact (K), q is the charge of an electron (C), J is the current density (A/m^2), V is the voltage applied to the micro-cooler (V), λ_E is the electron relaxation length (m), d_B is the barrier thickness (m), κ is the thermal conductivity (W/m·K), and ΔT is the temperature difference between the hot and cold contacts of the micro-cooler (K).

The model was written using MATLAB and was used to reproduce the plot shown in figure 6.1 (net cooling power density (Qd) against barrier thickness (d_B) for three barrier heights (ϕ)). The plot was published in both of the Shakouri et al. papers [49; 78]. Within Shakouri's earlier paper from 1998 [49], there was an additional plot that showed the current density (J) against the barrier thicknesses (d_B) for the three given barrier heights (ϕ), figure 6.2. This plot enabled

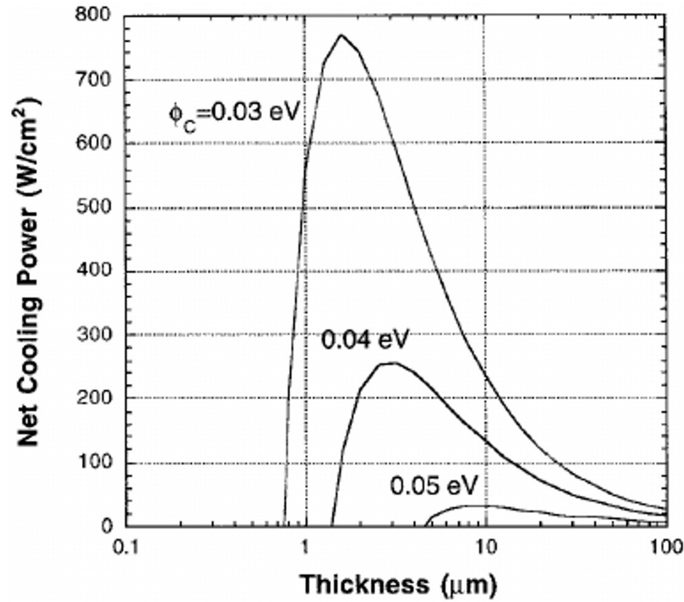

Figure 6.1: *Plot of net cooling power density (Qd) against barrier thickness (d_B) for three barrier heights (ϕ) taken from papers by Shakouri et al. [49; 78].*

values of J to be estimated for different barrier thickness (d_B) at the three barrier heights (ϕ).

This enabled a model to be developed around a limited sample of J within the range of barrier thicknesses (d_B) from 0.1 to 100 μm.

The presented MATLAB model is documented in Appendix B1 and the computed results for net cooling power density (Qd) against barrier thickness (d_B), for three barrier height (ϕ), are shown in figure 6.3.

The computed curves, in figure 6.3, show a very similar behaviour to those in figure 6.1, however to further improve the fit (to make the curves smoother) more data points were required. When considering the curve for $\phi = 0.03$ eV, a similar trend can be seen to that in figure 6.1 (with the peak net cooling power (Qd) at a thickness (d_B) of approximately 1 μm). In general, net cooling power densities in figure 6.3 were slightly higher for the same barrier thicknesses as in figure 6.1. This was possibly due to errors in the current density approximations from figure 6.2. This was more apparent at barrier thicknesses above 10 μm, as variations in the current density were very small, therefore difficult to determine on a logarithmic scale.

To improve the accuracy of J in terms of barrier thickness (d_B) best fit algebraic equations were generated to provide further values of current density (J) over the range of barrier thicknesses (from 0.1 to 100 μm) for the three barrier heights (ϕ), these have been plotted in figure 6.4.

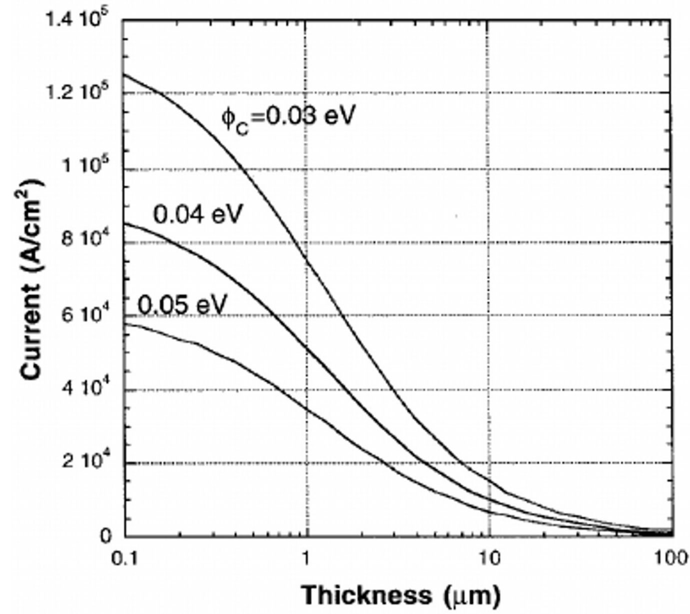

Figure 6.2: *Plot of current density (J) against barrier thickness (d_B) for three barrier heights (ϕ) taken from a paper by Shakouri et al. [49].*

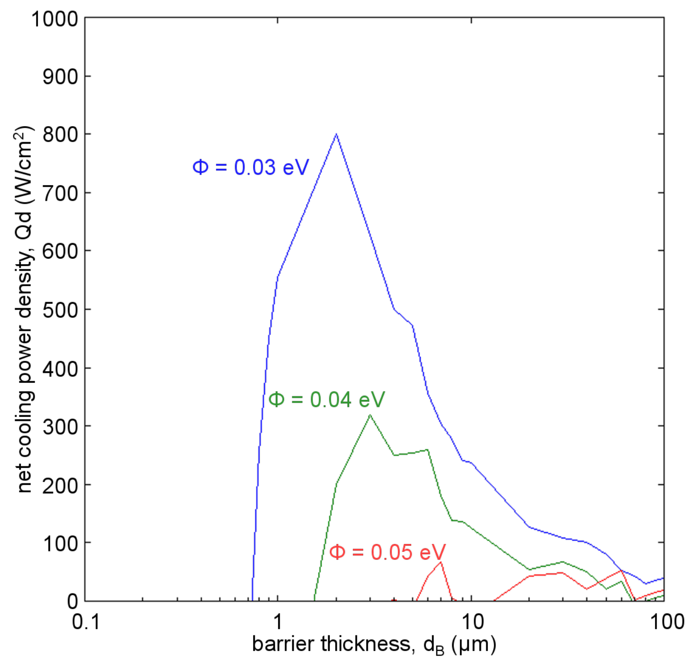

Figure 6.3: *Initial 1D model plot of net cooling power density (Qd) against barrier thickness (d_B) for three barrier heights (ϕ) to match results published by Shakouri et al. [49; 78].*

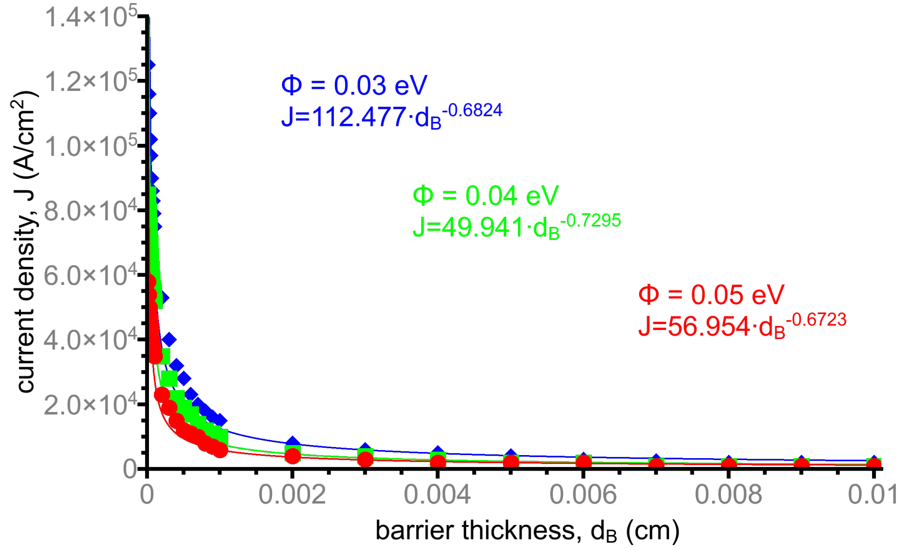

Figure 6.4: *Plot of approximated current density (J) against barrier thickness (d_{B}) for three barrier heights (ϕ), read from figure 6.2 to create functions to approximate J based on d_{B}.*

The algebraic equations were then added to the model (documented in Appendix B2). This enabled the current density (J) to be calculated for many more data points than before (the model calculated J for 1,000 values of barrier thickness (d_{B}), in 100 nm steps from 0.1 to 100 μm). The results for net cooling power density (Qd) against barrier thickness (d_{B}), for three barrier heights (ϕ) using the second model are shown in figure 6.5. The results shown in figure 6.5 more closely match the behaviour of figure 6.1. However, a lot of the calculated J values were still slightly higher than in the Shakouri et al. published results. The comparative error between the Shakouri et al. published results and the 1D model was relatively small, but more importantly the 1D model reproduced the same trends and order of magnitudes seen in the Shakouri et al. results. Therefore, the 1D model was used to simulate micro-coolers.

6.2 Combining cooling equations to make a complete 1D model

The complete net cooling power density equation from Shakouri et al. (6.2) was used to verify the model, but was then further simplified. To further simplify, the cooling power (Q) was computed rather than the cooling power density (Q_{d}),

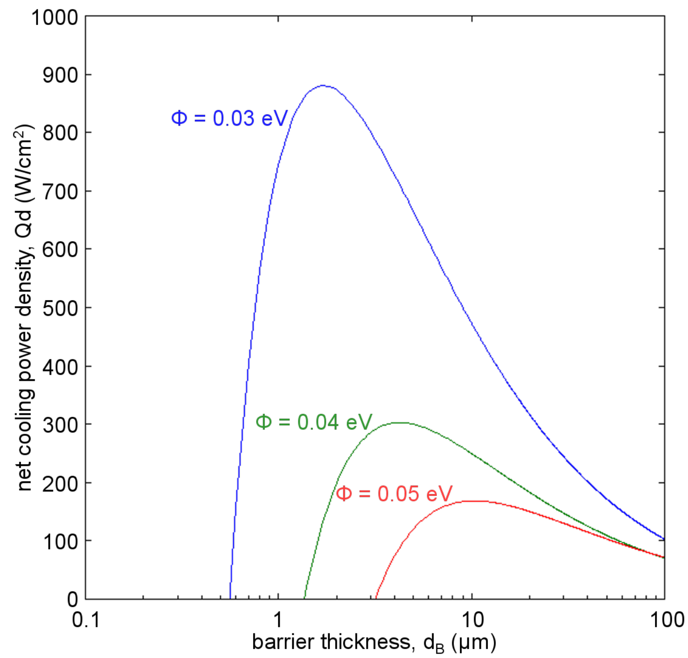

Figure 6.5: *1D model plot of net cooling power density (Qd) against barrier thickness (d_B) for three barrier heights (ϕ) to match results published by Shakouri et al. [49; 78] (made with the current density trends obtained from figure 6.4).*

making the equation a function of current (I) rather than current density (J). Equation (6.3) shows the net cooling power equation, which has previously been published [79].

$$Q = \left(\phi + \frac{2k \cdot T_c}{q}\right) I \; - \; I \cdot V \left[\tfrac{1}{2} - \frac{\lambda_E}{d_B} - \frac{\lambda_E^2}{d_B^2}\left(e^{\frac{-d_B}{\lambda_E}} - 1\right)\right] \; - \; \frac{\kappa \cdot A \cdot \Delta T}{d_B} \tag{6.3}$$

As with equation (6.2), where $Qd = Qd_t - Qd_{jh} - Qd_{hc}$, in equation (6.3) $Q = Q_t - Q_{jh} - Q_{hc}$ (where Q_t is the cooling power of the micro-cooler, Q_{jh} is the Joule (self-heating) heating power of the micro-cooler, and Q_{hc} is the heat conduction (flow-back heat) power of the micro-cooler). The Q_{jh} term in equation (6.3) required knowledge of the electron relaxation length (λ_E) of the simulated material. However, as λ_E is very small ($\sim 10^{-9}$ m) it can be assumed to equal 0, whereupon Q_{jh} will reach a maximum of $\frac{1}{2} I \cdot V$ (or half of the total power applied to the micro-cooler). Maximising Q_{jh} may be beneficial as it will increase one of the losses associated with the modelled micro-cooler, and any real-world (fabricated) micro-cooler will have far greater losses than those accounted for in the model. However, as V is proportional to I (which was varied for the model analysis) and is not a material property, it was simpler to calculate the total power applied to the micro-cooler as $I^2 \cdot R_{tot}$ instead of $I \cdot V$. The Q_{hc} term was simplified as $\frac{d_B}{\kappa \cdot A} = \Theta_C$, where Θ_C is the thermal impedance of the micro-cooler (K/W).

$$\therefore \; Q = I\left(\phi + \frac{2k \cdot T_c}{q}\right) \; - \; \tfrac{1}{2} I^2 \cdot R_{tot} \; - \; \frac{\Delta T}{\Theta_C} \tag{6.4}$$

The Q_t term can also be simplified, for a III-V based micro-cooler (with a similar style and area to those in this research), a maximum cooling of approximately 1 °C is expected. Therefore, $T_c \simeq T_{amb}$ (where T_{amb} is the ambient temperature around the micro-cooler). As temperatures are recorded in Kelvin on or around room temperature, $T_c = T_{amb} = 300 \pm 1$ K. This led to a simplified equation (6.5) that still gives a relatively good approximation for the proposed micro-coolers within this research.

$$Q = I\left(\phi + \frac{2k \cdot T_{amb}}{q}\right) \; - \; \tfrac{1}{2} I^2 \cdot R_{tot} \; - \; \frac{\Delta T}{\Theta_C} \tag{6.5}$$

In the published literature, plots of ΔT against the applied bias current (I) are often used to characterise a cooler [42; 43; 48; 61; 73; 75; 80; 81; 82; 83]. Therefore, computer models developed in this research work focused on determining the temperature difference between the contacts (ΔT) of the micro-cooler. The temperature difference (ΔT) of a micro-cooler was also experimentally measured

(chapter 5) and therefore enabled a direct comparison with the simulated micro-cooler results. Equation (6.5) was rearranged so that it was in terms of ΔT:

$$\Delta T = \Theta_C \left[I \left(\phi + \frac{2k \cdot T_{amb}}{q} \right) \; - \; \tfrac{1}{2} I^2 \cdot R_{tot} \; - \; Q \right] \tag{6.6}$$

ΔT_{max} will occur when $Q = 0$ (when the micro-cooler is in a state of equilibrium). As ΔT and Q are codependent upon each other, neither can be calculated if both are unknown. However, ΔT_{max} will also occur when $\frac{d\Delta T}{dI} = 0$ and since:

$$\frac{d\Delta T}{dI} = \Theta_C \left[\left(\phi + \frac{2k \cdot T_{amb}}{q} \right) \; - \; I \cdot R_{tot} \right]$$

The value and current at which ΔT_{max} occurs is independent of Q. Therefore, if the micro-cooler is always assumed to be in a quasi-steady-state ($Q = 0$), it will not affect ΔT_{max} or the current at which ΔT_{max} occurs, which can be written as I_{opt}. There will be some effect on the rate of change of ΔT with relation to I, but this will be negligible with respect to the amount of variation between a modelled and a real (fabricated) micro-cooler. This simplifies equation (6.6) to equation (6.7):

$$\Delta T = \Theta_C \left[I \left(\phi + \frac{2k \cdot T_{amb}}{q} \right) \; - \; \tfrac{1}{2} I^2 \cdot R_{tot} \right] \tag{6.7}$$

Equation (6.7) was used to model micro-coolers, provided R_{tot} was known. This was found from the IV measurements reported in chapter 5. However, $R_{tot} = R_{TC} + R_{SL} + R_{BC}$ (where R_{TC} is the top contact resistance, R_{SL} is the bulk resistance of the semiconductor layers, and R_{BC} is the bottom contact resistance). It was shown (in chapter 5) that the contact resistance (R_C) of the micro-cooler accounts for a large percentage of R_{tot}. Therefore, an estimate of the specific contact resistivity (ρ_C) is required. This was determined from the experimentally measured micro-cooler wafers using the TLM analyses, as described in chapter 5. However, the self-heating term in equation (6.7) states only half of the total internal heating will have a negative effect on the cooling performance ($\frac{1}{2} I^2 R_{tot} \Theta_C$), and represents the top (cooled) contact of the micro-cooler.

$$\therefore \; \tfrac{1}{2} I^2 \cdot R_{tot} = I^2 \left(\tfrac{1}{2} R_{SL} + R_{TC} \right)$$

The model was modified further, to equation (6.8).

$$\Delta T = \Theta_C \left[I \left(\phi + \frac{2k \cdot T_{amb}}{q} \right) \; - \; I^2 \left(\tfrac{1}{2} R_{SL} + R_{TC} \right) \right] \tag{6.8}$$

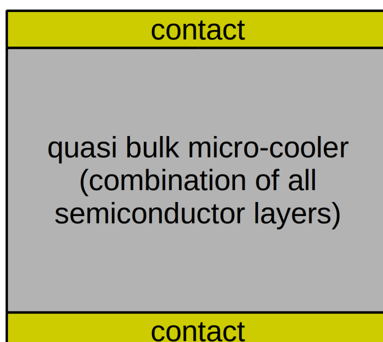

Figure 6.6: *Basic 1D model structure of a micro-cooler, as represented by the developed model.*

Equation (6.8) was used to perform 1D simulations of structures similar to that shown in figure 6.6. Equation (6.8) enabled the simulation of basic micro-cooler structures for a range of bias currents (I) and at a known ambient (operating) temperature (T_{amb}). The simulation required the knowledge of very few material properties, for example; barrier height (ϕ), thermal impedance (Θ_C), bulk semiconductor electrical resistance (R_{SL}), and top contact resistance (R_{TC}).
The above 1D model was completed and validated against the published micro-cooler results from the literature. The model was then used to investigate the effect of different material properties on the cooling performance of the micro-cooler. Most of the micro-coolers in this research were based on an AlGaAs superlattice. Therefore, the differences in cooling performance was primarily dependent on the geometry and contact resistance, as the thermal and electrical material properties will remain almost constant. It was shown experimentally (chapter 5, figure 5.9) that the specific contact resistivity (ρ_C) varies between fabrication iterations (it is dependent on the contact metal combination, semiconductor, and annealing process), for the AlGaAs superlattice micro-coolers. The work focussed on using the specific contact resistivities calculated from the Reeves & Harrison TLM, as it is believed they more accurately represent the contact resistance for devices fabricated as a superlattice structure.

6.3 How material properties of the semiconductor will affect cooling performance

The maximum ΔT cooling (ΔT_{max}) was chosen as the parameter to compare cooling performance between coolers with different material properties as the analysis does not consider exact bias conditions. ΔT_{max} occurs when $\frac{d\Delta T}{dI} = 0$

and this occurs at an optimal bias current (I_{opt}), which could be any value of I. Since:

$$\Delta T = \Theta_C \left[I \left(\phi + \frac{2k \cdot T_{amb}}{q} \right) - I^2 \left(\tfrac{1}{2} R_{SL} + R_{TC} \right) \right] \quad (6.8)$$

$$I_{opt} = \frac{\phi + \frac{2k \cdot T_{amb}}{q}}{R_{SL} + 2R_{TC}}$$

$$\therefore \ \Delta T_{max} = \frac{\Theta_C}{2R_{SL} + 4R_{TC}} \left(\phi + \frac{2k \cdot T_{amb}}{q} \right)^2 \quad (6.9)$$

As $\Theta_C = \frac{d_B}{\kappa \cdot A}$, $R_{SL} = \frac{d_B}{\sigma \cdot A}$, and $R_{TC} = \frac{\rho_C}{A}$, ΔT_{max} can be rewritten as:

$$\Delta T_{max} = \frac{\sigma}{2\kappa(1 + \frac{2\rho_C \cdot \sigma}{d_B})} \left(\phi + \frac{2k \cdot T_{amb}}{q} \right)^2 \quad (6.10)$$

or

$$\Delta T_{max} = \frac{d_B}{2\kappa(\frac{d_B}{\sigma} + 2\rho_C)} \left(\phi + \frac{2k \cdot T_{amb}}{q} \right)^2 \quad (6.11)$$

Where κ is the thermal conductivity of the bulk semiconductor (superlattice) region (W/m·K) and σ is the electrical conductivity of the bulk semiconductor (superlattice) region (S/m).

Equations (6.10) and (6.11) show that ΔT_{max}:

- is independent of the micro-cooler area (A)
- increases with ambient temperature (T_{amb}), superlattice thickness (d_B), barrier height (ϕ), and electrical conductivity (σ) of the semiconductor
- decreases with specific contact resistivity (ρ_C) and thermal conductivity (κ) of the semiconductor

The equation manipulation and derivation is shown in Appendix A1.
Most of these properties are determined by the semiconductor materials used. Therefore, for III-V bulk semiconductors, there are minimal variations of the above properties that can be achieved. The use of a superlattice enabled the material properties to be manipulated to give, for example a higher electrical conductivity (σ) but lower thermal conductivity (κ) compared to the properties of the bulk materials making the superlattice (section 6.3.2). The contacting technology can also be used to improve the contact resistance by reducing the specific contact resistivity of the metal-semiconductor interface (section 6.3.1).

6.3.1 Effect of contact resistance

The range of specific contact resistivity (ρ_C) measured using the Reeves & Harrison TLM was from approximately 8×10^{-6} to 3×10^{-5} $\Omega\cdot$cm^2 (figure 5.9 of chapter 5). For a simple micro-cooler with a top contact of 100×100 μm (A = 10,000 μm^2), the contact resistance (R_C) ranges from 80 to 300 mΩ for both the top contact (R_{TC}) and bottom contact (R_{BC}) resistances. This is a large range of resistance to consider, especially as any variation to ρ_C (and therefore R_{TC}) will affect ΔT_{max} (and I_{opt}). As ρ_C increases, the self-heating also increases, which reduces ΔT_{max} and the current (I_{opt}).
Modelling ΔT_{max} against ρ_C enabled a maximum useful ρ_C (that could supply useful ΔT cooling) to be determined for a specific micro-cooler geometry (Area, $A = 10,000\ \mu m^2$ and superlattice thickness, $d_B = 2\ \mu m$), figure 6.7.

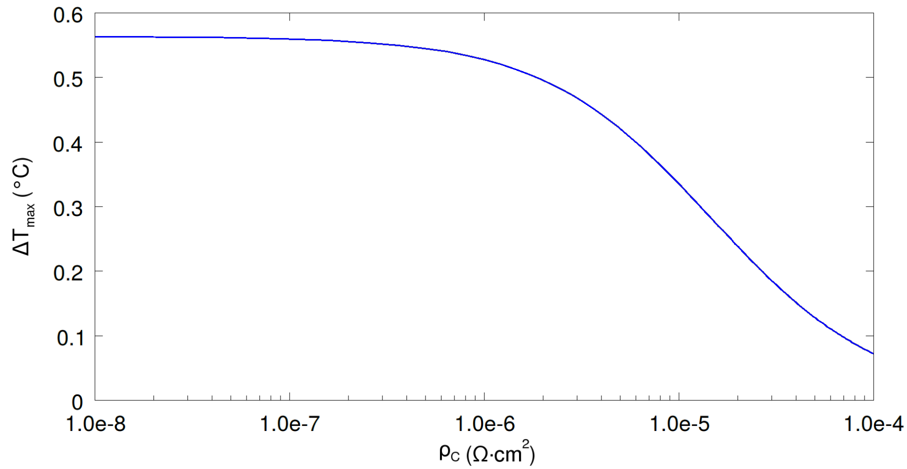

Figure 6.7: *Modelled plot showing how* ΔT_{max} *changes with respect to* ρ_C*, for* ρ_C *values from* 10^{-8} *to* 10^{-4} $\Omega\cdot cm^2$*, on an AlGaAs superlattice micro-cooler of* $A = 10,000\ \mu m^2$ *and* $d_B = 2\ \mu m$*, at a temperature of* $T_{amb} = 300\ K$*.*

Since $R_{TC} = \frac{\rho_C}{A}$, equation (6.9) was used to plot ΔT_{max} with respect to ρ_C, as in figure 6.7. (The model is documented in Appendix B3).
Figure 6.7 shows for a 100×100 μm AlGaAs superlattice micro-cooler, a ΔT of >0.5 °C was achievable provided $\rho_C \leq 2\times10^{-6}$ $\Omega\cdot$cm^2. However, if $\rho_C \geq 6\times10^{-5}$ $\Omega\cdot$cm^2 then ΔT_{max} will be less than 0.1 °C, which corresponds to the thermal resolution of the IR thermal microscope. The low ΔT_{max} would prevent the use of the IR thermal measurement technique in making useful temperature measurements of the fabricated AlGaAs superlattice micro-coolers, with $\rho_C \geq 6\times10^{-5}$ $\Omega\cdot$cm^2.

To further understand how changes in ρ_C (which will affect the values of R_{TC} and R_{tot}) will affect the ΔT cooling, equation (6.8) was used to simulate the same AlGaAs superlattice micro-cooler for four values of ρ_C; 10^{-4}, 10^{-5}, 10^{-6}, and 10^{-7} $\Omega\cdot cm^2$ respectively, over a current range from 0 to 2 A (figure 6.8). The four selected values of ρ_C cover the experimental values of ρ_C obtained from the Reeves & Harrison TLM as well as 10^{-6} and 10^{-7} $\Omega\cdot cm^2$ as values of ρ_C for the technology value to aim for. The developed model is documented in Appendix B4.

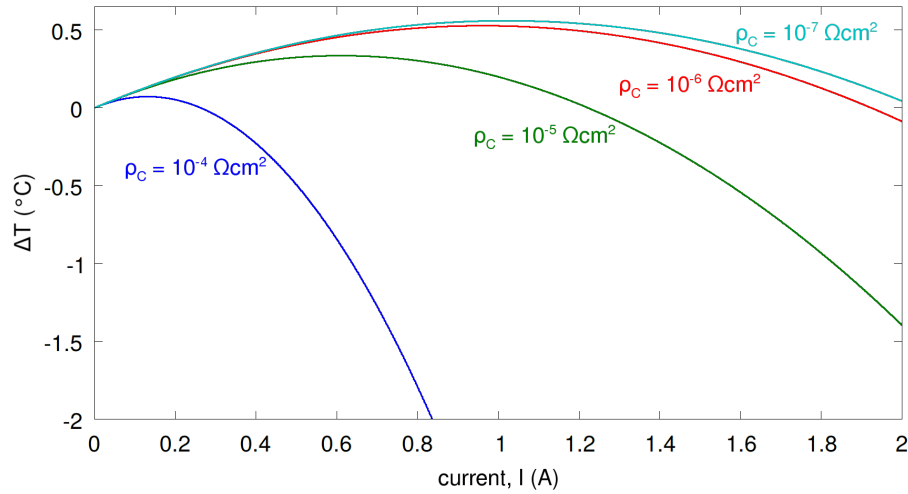

Figure 6.8: *Modelled plot showing how ΔT changes with respect to I, for 4 values of ρ_C (10^{-4}, 10^{-5}, 10^{-6}, and 10^{-7} $\Omega\cdot cm^2$), on an AlGaAs superlattice micro-cooler of* $A = 10,000$ μm^2, $d_B = 2$ μm, *and* $T_{amb} = 300$ K.

Figure 6.8 shows that as ρ_C reduces, ΔT_{max} and I_{opt} both increase.
Equation (6.8) shows that the parasitic electrical resistance of the micro-cooler will always reduce the cooling performance. As the resistance increases, ΔT decreases because of the increase in self-heating.
It can also be seen that when $\rho_C > 10^{-6}$ $\Omega\cdot cm^2$ there is a negligible increase to ΔT_{max} (figure 6.8). For this condition, $R_{TC} \ll R_{SL}$ and so the bulk resistance of the micro-cooler (R_{SL}) dominates R_{tot}, therefore further reductions to ρ_C (and therefore R_{TC}) have a limited effect on R_{tot} and the amount of self-heating in the micro-cooler.

6.3.2 Thermal conductivity

The optimisation of the thermal conductivity of the materials that the micro-cooler is fabricated from is clearly a useful calculation to achieve an improved

cooling performance (as shown earlier in section 6.3). Experimentally determining the thermal conductivity of non-standard semiconductor alloys is difficult as many measurements would have to be made as the percentage of the alloying semiconductor is increased. Some of these alloys have been analysed for their thermal conductivity and so have known values, but this has not been carried out for all possible percentage variations of an alloy. In this research a simple 1D model has been developed to simulate the behaviour of materials, for example $Al_xGa_{1-x}As$ for varying values of x. The model was based on the work of Adachi [84], who published a set of equations used to estimate the thermal conductivity (κ) of many III-V semiconductor alloys, for example AlGaAs, AlGaN, InGaAs, and InAlAs. Adachi reported that for a 3-material alloy, which is made of two 2-material alloys (AC and BC) with one shared alloying material (C). The thermal conductivity varies as shown in equation (6.12).

$$\kappa(x) = \frac{1}{x\theta_{\mathrm{AC}} + (1-x)\theta_{\mathrm{BC}} + x(1-x)\mathrm{C}_{\mathrm{A-B}}} \quad [84] \tag{6.12}$$

Where $\kappa(x)$ is the thermal conductivity (W/m·K) as a function of x, θ_{AC} is the thermal resistivity of material AC (m·K/W), θ_{BC} is the thermal resistivity of material BC (m·K/W), and $\mathrm{C}_{\mathrm{A-B}}$ is a thermal resistivity contribution based on the lattice disorder between materials A and B (m·K/W) (as referred to by Adachi [84]).

Within the 2007 paper [84], Adachi included thermal resistivity values for many of the reported alloys, including:

$$\theta_{\mathrm{AlAs}} = 1.10 \text{ cm·K/W} \quad \theta_{\mathrm{GaAs}} = 2.22 \text{ cm·K/W} \quad \theta_{\mathrm{InAs}} = 3.3 \text{ cm·K/W}$$

However, Palankovski's PhD thesis [85] reported that $\kappa_{\mathrm{AlAs}} = 80$ W/m·K, which equates to $\theta_{\mathrm{AlAs}} = 1.25$ cm·K/W. The thermal conductivities for GaAs and InAs reported by Palankovski were similar to those reported by Adachi. Additionally, Adachi reported values for the lattice disorder thermal resistivity contribution ($\mathrm{C}_{\mathrm{A-B}}$) for Al−Ga ($\mathrm{C}_{\mathrm{Al-Ga}} = 32$ cm·K/W), Ga−In ($\mathrm{C}_{\mathrm{Ga-In}} = 72$ cm·K/W), and Al−In ($\mathrm{C}_{\mathrm{Al-In}} = 15$ cm·K/W) [84]. This enabled the development of a model to reproduce Adachi's results (including experimental results by Abrahams et al. [86] for InGaAs alloys, extrapolated from FIG. 6(a) that is in reference [84]). The model is documented in Appendix B5. Figure 6.9 shows the thermal conductivity (κ) values for $In_{1-x}Ga_xAs$ for the variations of x and figure 6.10 shows the thermal conductivity (κ) values for $Al_xGa_{1-x}As$ for the variations of x (using both Adachi's and Palankovski's thermal conductivity of AlAs).

Figure 6.9 shows a good correlation between Adachi's equation (6.12) [84] and the reported experimental results [86]. This gave confidence in Adachi's equation to be used for estimating the thermal conductivity of semiconductor alloys such as the AlGaAs used in this research.

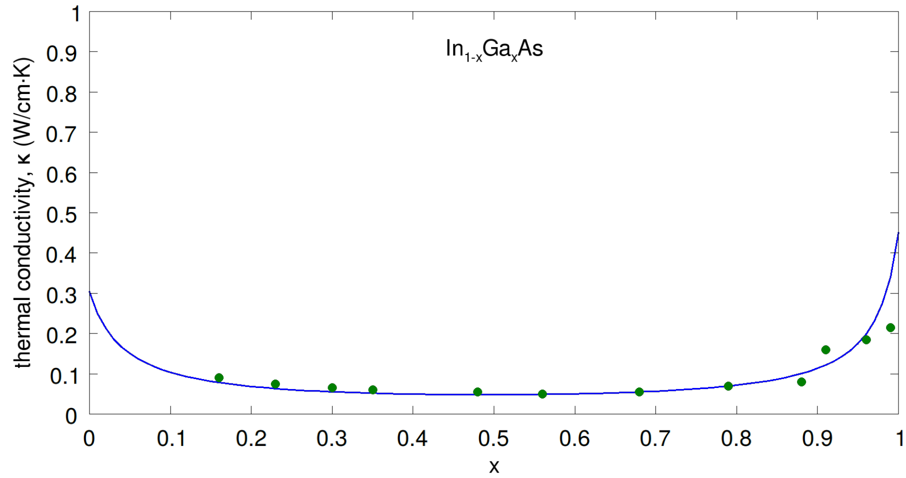

Figure 6.9: *Modelled results to analyse the thermal conductivity (κ) of $In_{1-x}Ga_xAs$ for variations of x (blue line), including numerous experimental results [86] for a variety of InGaAs alloys (green circles), extrapolated from [84].*

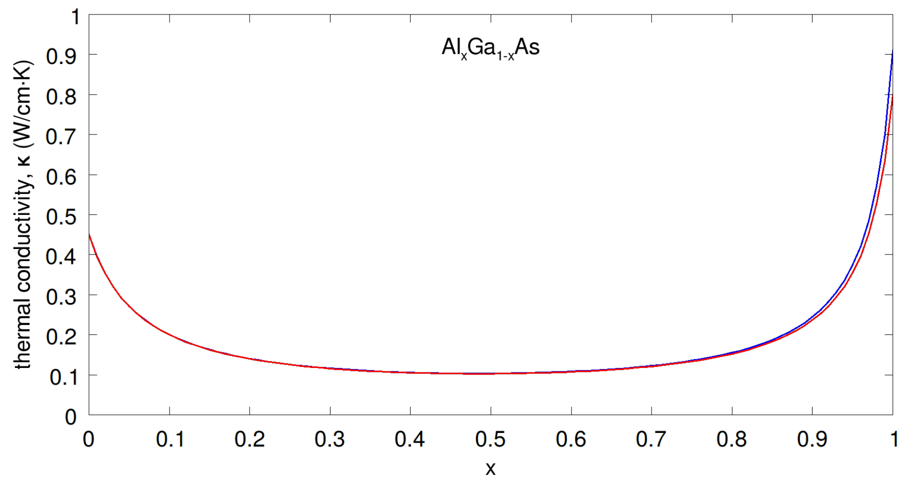

Figure 6.10: *Modelled results to analyse the thermal conductivity (κ) of $Al_xGa_{1-x}As$ for variations of x, considering two κ_{AlAs} values, from Adachi (blue line) [84] and Palankovski (red line) [85].*

Both values of κ_{AlAs} in figure 6.10 (the blue line from Adachi [84] and red line from Palankovski [85]) showed very similar characteristics. Variations in $\kappa(x)$ for both values was negligible when $x < 0.9$. Therefore, small variations in κ_{AlAs} can be ignored unless the aluminium content approaches $x = 1$.
This ability to approximate the thermal conductivity of III-V semiconductor alloys enables modelling of almost any material configuration (as long as a $\mathrm{C}_{\mathrm{A-B}}$ can be obtained), enabling a complete thermal conductivity optimisation process for the micro-coolers.
Once these individual alloy thermal conductivities are known, the thermal conductivity of a superlattice (made from two different III-V alloys) can be calculated. Simkin et al. [56] showed an approximation of the thermal conductivity of a superlattice (κ_{SL}), made from a combination of material 1 and 2, as:

$$\kappa_{\mathrm{SL}} = \frac{\mathrm{L}_1 + \mathrm{L}_2}{\frac{\mathrm{L}_1}{\kappa_1} + \frac{\mathrm{L}_2}{\kappa_2} + \Theta_{\mathrm{B}}} \quad [56] \tag{6.13}$$

Where L_1 is the thickness of one period of material 1 (m), L_2 is the thickness of one period of material 2 (m), κ_1 is the thermal conductivity of material 1 (W/m·K), κ_2 is the thermal conductivity of material 2 (W/m·K), and Θ_{B} is the thermal boundary impedance between materials 1 and 2 (K/W).

However, the thermal boundary impedance (Θ_{B}) is not always known. For superlattices that are fabricated from two similar semiconductor alloys, such as $\mathrm{Al_{0.1}Ga_{0.9}As}$ and $\mathrm{Al_{0.2}Ga_{0.8}As}$ used in this research, Θ_{B} will be small and approximates to zero. Huxtable [87] reported a simplified equation (6.13) that does not consider Θ_{B}:

$$\kappa_{\mathrm{SL}} = \frac{\mathrm{L}_1 + \mathrm{L}_2}{\frac{\mathrm{L}_1}{\kappa_1} + \frac{\mathrm{L}_2}{\kappa_2}} \quad [87] \tag{6.14}$$

The simplified equation (6.14) gives an approximation of the thermal conductivity of a superlattice containing similar semiconductor alloys. The resulting thermal conductivity of the superlattice can be substituted for the bulk semiconductor value of thermal conductivity in the 1D model developed for the micro-coolers.
Both equation (6.13) & (6.14) will give a superlattice thermal conductivity (κ_{SL}) that is lower than the average thermal conductivity of the materials used to make up the superlattice (κ_1 & κ_2). Therefore, the cooling performance of a superlattice micro-cooler will be improved compared to a micro-cooler using a bulk semiconductor.

6.3.3 Comparing experimental results with the model

Combining all the described aspects of the micro-cooler thermal model enabled a comparison to be made with the experimental work. The model considers a vertical structure with the complete mesa area metallised. Therefore, micro-cooler A9 (section 5.3) was the closest fabricated micro-cooler to the structure assumed by the 1D model. The micro-cooler A9 had a round cathode contact that covered almost all the mesa area. The analysis from section 5.3.2 showed that the cooling behaviour of A9 only matched that of the standard micro-cooler equations for the low bias currents (30 to 125 mA). Therefore, only the experimental results in this current range were used for the comparison (figure 6.11).

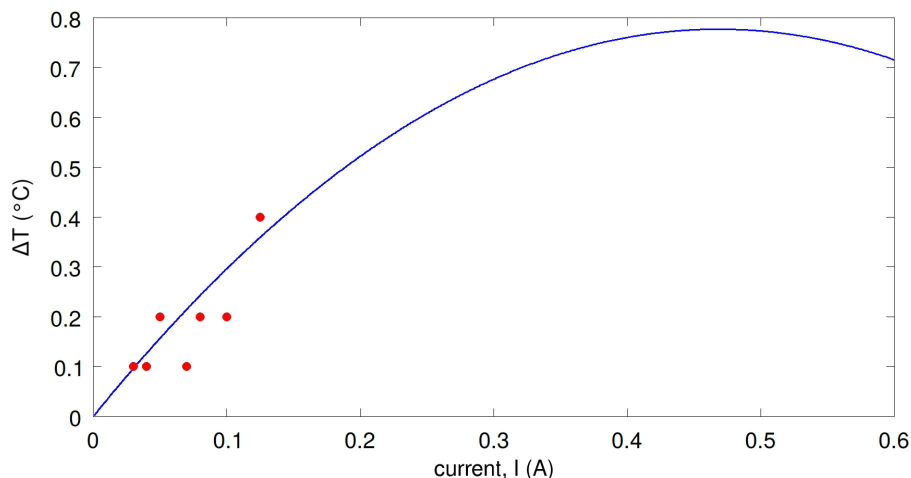

Figure 6.11: *Comparison between experimental results (red circles) with model (blue line), for micro-cooler A9.*

Figure 6.11 shows a very similar behaviour between the simulation and experiment to currents approaching 150 mA. At higher currents the experimental results showed high levels of probe heating, which was not included in the 1D model.

6.4 Creating model of integrated micro-cooler

The developed 1D model of the micro-cooler was used to give an estimate of the cooling performance from coolers fabricated with a wide range of structures and materials. One of the aims of this research was to consider how the micro-cooler will behave as part of an integrated circuit. Where the cooler and active device are both fabricated on a thick supporting substrate (figure 6.12). This work was

published in the Semiconductor Science and Technology journal in 2015 [9]. All integrated circuit structures have to be fabricated on a substrate that provides mechanical support and a thermal path to the heat-sink.

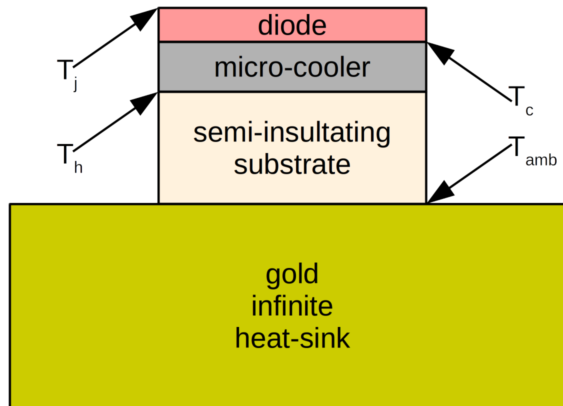

Figure 6.12: *Basic structure of a planar Gunn diode integrated as part of the micro-cooler, including positions of the four temperatures of importance during the analysis of this structure.*

6.4.1 Effect of substrate thickness

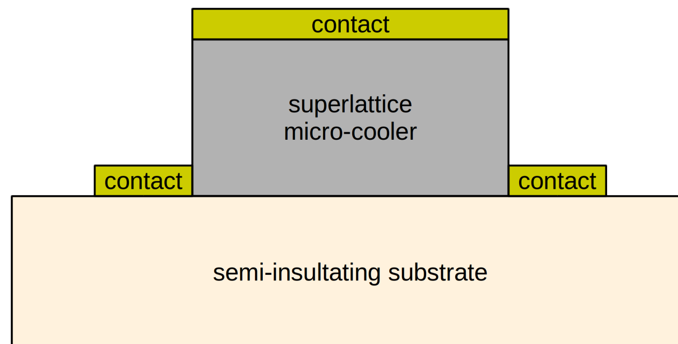

Figure 6.13: *Micro-cooler and substrate structure, which was analysed to estimate the effect of the integrated semi-insulating substrate on the micro-cooler performance.*

An equation was developed to approximate the ΔT of a micro-cooler mounted on a thick semi-insulating substrate (figure 6.13) [9]. This approach is novel and was developed as part of this research program. The substrate gives mechanical

support for the growth of the semiconductor layers and then the subsequent processing to realise the micro-cooler and active device. However, the substrate also acts as a thermal barrier between the micro-cooler and heat-sink.
Most published work on micro-coolers has not included a substrate. The modelling of the micro-coolers was based on two equations (6.7) (developed within this research) and (6.15) (based on the classic thermoelectric equation (2.5), section 2.3.2).

$$\Delta T = \Theta_C \left[I \left(\phi + \frac{2k \cdot T_{amb}}{q} \right) - \tfrac{1}{2} I^2 \cdot R_{tot} \right] \quad (6.7)$$

$$\Delta T = \Theta_C \left(SIT_c - \tfrac{1}{2} I^2 R_{tot} \right) \tag{6.15}$$

Both of these equations have the same basic structure, where the observed cooling (ΔT) is the total cooling minus the self-heating ($\frac{1}{2}\Theta_C I^2 R_{tot}$). The only structural difference between the two equations are the parts representing the total cooling power, $I(\phi + \frac{2k \cdot T_{amb}}{q})$ and SIT_c respectively. As both equations approximate the same behaviour, they can be considered as equivalents, therefore:

$$\phi + \frac{2k \cdot T_{amb}}{q} = ST_c$$

Equation (6.15) is clearly easier to follow and understand than equation (6.7) because there are fewer variables. Therefore, when considering the more complex integrated micro-coolers, the simpler form of the equation was adopted, which includes the Seebeck coefficient. The cooling temperature was not the focus of this section of the research, the focus was on how heat is distributed throughout the whole structure and how quickly/effectively heat can be removed. Equation (6.16) is the base equation derived to consider the behaviour of a cooler and substrate combination [9]. The derivation of equation (6.16) from fundamental equations (2.4) & (2.5) is shown in Appendix A2.

$$\Delta T = \frac{\Theta_C SIT_{amb} + \Theta_C I^2 R_{TC}(\Theta_S SI - 1) + \Theta_S \Theta_C SI^3 R_{BC}}{1 + \Theta_C SI} \quad [9] \tag{6.16}$$

Where Θ_C is the thermal impedance of the micro-cooler (K/W) and Θ_S is the thermal impedance of the substrate (K/W).

For an ideal, non-integrated micro-cooler, where an ideal heat-sink is directly underneath the heated contact of the cooler, Θ_S tends to zero, so that:

$$\Delta T = \frac{\Theta_C SIT_{amb} - \Theta_C I^2 R_{TC}}{1 + \Theta_C SI} \tag{6.17}$$

It is interesting to note that S is very small ($\sim 10^{-6}$ V/K), therefore $1+\Theta_C SI \simeq 1$ and equation (6.17) approximates to the classic equation for an ideal cooler, partially validating the approach taken:

$$\Delta T = \Theta_C \left(SIT_c - \tfrac{1}{2}I^2R_{tot}\right) \quad (6.15)$$

Additionally, in an ideal, non-integrated micro-cooler, the bottom contact would be in direct contact with the heat-sink. This means that $T_h = T_{amb}$ and so $T_c = T_{amb} - \Delta T$, therefore (6.15) can be rewritten as:

$$\Delta T = \Theta_C SI(T_{amb} - \Delta T) - \Theta_C I^2 R_{TC} \tag{6.18}$$

Hence, equation (6.16) becomes:

$$\Delta T = \frac{\Theta_C SI(T_{amb} + \Theta_S I^2 R_{TC} + \Theta_S I^2 R_{BC}) - \Theta_C I^2 R_{TC}}{1 + \Theta_C SI} \tag{6.19}$$

This can be approximated to:

$$\Delta T = \Theta_C SI(T_{amb} + \Theta_S I^2 R_{TC} + \Theta_S I^2 R_{BC}) - \Theta_C I^2 R_{TC} \tag{6.20}$$

So with this integrated structure, there is a $T_{amb} + \Theta_S I^2 R_{TC} + \Theta_S I^2 R_{BC}$ term instead of the $T_{amb} - \Delta T$ term. This new term can be considered as $T_{amb} - \Delta T + \Delta T_1$, where $\Delta T_1 = \Theta_S I^2(R_{TC} + R_{BC})$. This leads (6.20) to be written as:

$$\Delta T = \Theta_C SI(T_{amb} - \Delta T + \Delta T_1) - \Theta_C I^2 R_{TC} \tag{6.21}$$

ΔT_1 can be considered as the temperature rise at the base of the micro-cooler (at the top of the substrate) due to the self-heating of the micro-cooler contacts (top and bottom). For an integrated cooler with a semi-insulating substrate, the heat deposited at the bottom contact of the cooler (as well as the self-heating in this region) is not absorbed into the heat-sink instantly. The heat has to flow through the substrate (with a relatively high thickness) before it can be dissipated within a heat-sink.
In equation (6.21) with the ΔT_1 term there are a number of interpretations, which are given below as four scenarios:

1. ΔT increases (as $T_h > T_c$ and $\Theta_C SI(T_{amb} - \Delta T + \Delta T_1) > \Theta_C I^2 R_{TC}$), therefore cooling occurs ($\Delta T > \Delta T_1$).

2. ΔT decreases (as $T_c > T_h$ and $\Theta_C I^2 R_{TC} > \Theta_C SI(T_{amb} - \Delta T + \Delta T_1)$), therefore normal self-heating occurs ($\Delta T > \Delta T_1$).

3. ΔT increases (as $T_h > T_c$ and $\Theta_C SI(T_{amb} - \Delta T + \Delta T_1) > \Theta_C I^2 R_{TC}$), no cooling occurs ($\Delta T_1 > \Delta T$).

4. ΔT decreases (as $T_c > T_h$ and $\Theta_C I^2 R_{TC} > \Theta_C SI(T_{amb} - \Delta T + \Delta T_1)$), excessive (top contact) self-heating occurs to counteract the increased $\Theta_C SI(T_{amb} - \Delta T + \Delta T_1)$ term ($\Delta T_1 > \Delta T$).

1 and 2 represent the usual cooling behaviour of a non-integrated micro-cooler, while 3 and 4 represent the additional conditions because of the semi-insulating substrate. If a micro-cooler was solely analysed by a measured ΔT value, 1 and 3 would suggest cooling is taking place.
Therefore, considering an integrated micro-cooler, the thermal impedance of the substrate (Θ_S) as well as the top and bottom contact resistances (R_{TC} and R_{BC}) become very important parameters in determining the cooling performance. The analysis shows that to maximise the cooling performance ΔT_1 needs to be minimised. This can be achieved by minimising both the substrate thermal impedance and the contact resistances of the micro-cooler. For a III-V based integrated micro-cooler the substrate is most likely to be either semi-insulating GaAs or InP, and the thermal conductivity of these materials are low (0.55 and 0.68 W/cm·K respectively [88]). In a real micro-cooler as part of an integrated circuit, the best way to minimise the thermal impedance is to mechanically thin the substrate. The importance of a thin substrate can be seen from tables 6.1, 6.2, & 6.3, which are based on an AlGaAs/GaAs micro-cooler on a semi-insulating GaAs substrate [9]. ΔT was calculated as a function of substrate thickness for three scenarios; no substrate, a 50 μm thick substrate, and a 600 μm thick substrate. ΔT was then calculated as a function of micro-cooler current (I) for the above three substrate thicknesses. All computed ΔT values were positive, suggesting cooling for all three scenarios. However, when ΔT is compared to ΔT_1, it was seen that cooling does not always occur. When there is no substrate (table 6.1) or the 50 μm thick substrate (table 6.2) at low bias currents, cooling occurred ($\Delta T > \Delta T_1$). However, when the substrate thickness was increased to 600 μm, no cooling occurred as $\Delta T_1 > \Delta T$.
Therefore, for any useful cooling to be observed the substrates will have to be substantially thinned, however this will reduce the mechanical support that the substrate would usually provide.
The work shows for the first time that the substrate material should have a high thermal conductivity and be as thin as possible, while still sufficiently robust to provide mechanical support to the integrated components. It is also interesting to note that all supplied fabricated micro-coolers were on a GaAs substrate material approaching 600 μm thick and all devices gave very small amounts of cooling (typically 0.1 to 0.4 °C), even when the micro-cooler contacts were thermally isolated and bias probe loading was taken into account.

Table 6.1: *No semi-insulating substrate (cooling only).*

I (A)	**ΔT (°C)**	**ΔT_1 (°C)**
0.01	0.03 (cooling)	0
0.05	0.13 (cooling)	0
0.10	0.25 (cooling)	0
0.15	0.35 (cooling)	0
0.20	0.44 (cooling)	0
0.25	0.52 (cooling)	0
0.30	0.58 (cooling)	0
0.35	0.62 (cooling)	0
0.40	0.66 (cooling)	0
0.45	0.67 (cooling)	0
0.50	0.67 (cooling)	0
0.55	0.66 (cooling)	0
0.60	0.64 (cooling)	0
0.65	0.59 (cooling)	0
0.70	0.54 (cooling)	0
0.75	0.47 (cooling)	0
0.80	0.38 (cooling)	0

Table 6.2: *50 μm substrate (cooling and heating).*

I (A)	**ΔT (°C)**	**ΔT_1 (°C)**
0.01	0.03 (cooling)	0.0002
0.05	0.13 (cooling)	0.05
0.10	0.25 (cooling)	0.19
0.15	0.36 (heating)	0.43
0.20	0.44 (heating)	0.76
0.25	0.52 (heating)	1.2
0.30	0.58 (heating)	1.7
0.35	0.63 (heating)	2.4
0.40	0.67 (heating)	3.1
0.45	0.68 (heating)	3.9
0.50	0.69 (heating)	4.8
0.55	0.69 (heating)	5.8
0.60	0.67 (heating)	6.9
0.65	0.64 (heating)	8.1

Table 6.3: *600 μm substrate (heating only).*

I (A)	**ΔT (°C)**	**ΔT_1 (°C)**
0.01	0.03	0.03
0.05	0.13 (heating)	0.59
0.10	0.25 (heating)	2.36
0.15	0.38 (heating)	5.31
0.20	0.46 (heating)	9.44
0.25	0.55 (heating)	14.75
0.30	0.63 (heating)	21.26
0.35	0.70 (heating)	28.96
0.40	0.77 (heating)	37.76
0.45	0.84 (heating)	47.8
0.50	0.90 (heating)	59.0
0.55	0.96 (heating)	71.4
0.60	1.02 (heating)	85
0.65	1.10 (heating)	101

6.5 Summary

Important points raised in this chapter are:

- A developed 1D model to approximate micro-cooler behaviour.
- The importance of minimising specific contact resistivity (ρ_C) was shown.
- ΔT will be slightly higher for a superlattice micro-cooler when compared to a bulk semiconductor micro-cooler, as the thermal conductivity of the superlattice can be engineered.
- Micro-cooler cooling performance is only beneficial if the semi-insulating GaAs substrate can be substantially thinned ($<$50 μm). Otherwise, useful cooling will not be feasible.

Chapter 7

Conclusions & future work

7.1 Infra-red thermal measurement

Throughout this research (chapters 3, 4, & 5) developments have been made to the novel carbon micro-particle sensor measurement technique, utilising infra-red (IR) thermal microscopy. These include showing that sub-10 μm diameter micro-particle sensors are as usable as larger particles (for example 20 μm diameter) for accurate temperature measurements over the 80 to 110 °C operating temperature range, even though the emitted radiance for sub-10 μm diameter particles is known to be lower than for larger diameter particles (chapter 3). Precision positioning of micro-particle sensors has also been achieved by the development of the camera software, which superimposes a precision optical grid onto a still frame of the DUT to measure the position of the micro-particle.

7.2 Planar Gunn diode

The research has reported the use of the micro-particle sensor for more detailed IR thermal microscopy measurements, enabling thermal profiling in the channel region of planar Gunn diodes (section 4.4.2). The thermal profiles were measured both along the central region of the channel and across the channel by manipulating a single micro-particle sensor into the required positions inside the channel or on the metal contacts, which run parallel to the channel. This technique required the voltage bias to the Gunn diode to be reset for every micro-particle position. The repositioning of the micro-particle sensor required removal of the bias probes. Repeated positioning of the bias probes led to damage of the planar Gunn diode contacts.

To enable all the micro-particle sensor positions to be measured under the same bias conditions, an alternative profiling technique was adopted. The second technique utilised multiple micro-particle sensors (of similar diameters), one at every profile position, which could all be measured at the same time and therefore under an identical bias condition. Unfortunately this method may thermally load a small device, the performance of multiple micro-particle sensor profiles is a subject of ongoing research. However, to the author's knowledge, this is the first time an IR micro-particle sensor has been used to measure the channel temperature profile of a planar Gunn diode. The measured temperature profiles showed that the temperature in the channel peaked at approximately the centre of the channel.

7.3 Micro-coolers

Many AlGaAs superlattice micro-cooler structures were measured and simulated. It was found common to all the structures that the cooling temperature (ΔT), which is the difference between the temperature of the anode (heated contact, T_h) and cathode (cooled contact, T_c), was always small (<1 °C). This was in-line with the already published work on individual AlGaAs superlattice based micro-coolers by Zhang [48].
In this work a novel method for measuring the small temperature difference (ΔT) between the anode and cathode contacts was developed. The method used two micro-particle sensors, one placed on the anode contact and the other on the cathode contact. Both micro-particles could be focused simultaneously under the IR microscope, enabling the temperature of both contacts to be measured at the same time, with identical bias conditions (section 5.3). This method enabled temperature differences approaching 0.1 °C to be measured.
Some AlGaAs superlattice micro-coolers were found to give an anomalously high ΔT (>1 °C) when compared with published work and computer simulation. This was thought to be due to the bias probes thermally loading the anode contact of the micro-cooler. A novel analytical method (section 5.3.2) was developed to ascertain which part of the measured ΔT was due to cooling of the cathode contact and which part was due to bias probe thermal loading. This was achieved by plotting ΔT as a function of the square of the bias current (I^2) applied to the micro-cooler. The resulting graph resulted in two linear trend-lines. One line showed a positive gradient and represented cooling, while the second showed a negative gradient and represented the probe thermal loading. The plot indicated that the maximum ΔT achieved was only 0.4 °C. This analysis was applied to a number of experimental AlGaAs superlattice micro-coolers, to observe when the

measured ΔT was not affected by the probe thermal loading. This also begs the question of the validity of the ΔT cooling observed for some earlier experimental work on III-V based micro-coolers, with the bias probes making a direct connection with the contacts.
The analysis of thermal loading of a micro-cooler (section 5.3.1) showed that thermal loading from the bias probes was a significant problem when making connection to an individual micro-cooler, while still on-wafer. To experimentally make thermal measurements with minimal bias probe thermal loading, the micro-cooler contacts had to be thermally isolated from the bias probes.
Work on measuring the contact resistance of AlGaAs superlattice micro-coolers showed that the Reeves & Harrison based TLM gave a higher specific contact resistivity (ρ_C) than the conventional TLM (section 5.2.2). The Reeves & Harrison based TLM was used to collect data to feed into the micro-cooler simulations, as the measurement took into account both the horizontal and vertical resistances of the semiconductor layers below the metallised contact.

7.4 Integration of micro-cooler

The research work on AlGaAs superlattice micro-coolers was instigated by the requirement to provide enhanced cooling for the milli-metric/terahertz planar Gunn diode. The solution was to fabricate the planar Gunn diode and micro-cooler as an integrated circuit. In other words, using the micro-cooler as an active cooling device with the GaAs based planar Gunn diode fabricated directly above the micro-cooler. This approach would be a fully integrated solution and required no adhesive processes as currently used to mount individual active devices to individual micro-coolers. The adoption of an integrated micro-cooler also enabled the area of the devices to be substantially reduced when compared to conventional, commercial micro-coolers, which are tens of square millimetres in area. However, a problem was found when trying to integrate a micro-cooler as part of an integrated circuit, due to the supporting substrate (section 6.4). The high thermal impedance of the substrate, partially due to its thickness (620 μm), prevented heat-flow through the substrate. Therefore, heat was restricted at the interface between the micro-cooler structure and the substrate. This resulted in additional anode heating, as well as an increase to the thermodynamic flow-back of heat towards the cathode contact. For a GaAs based micro-cooler the substrate thickness would have to be substantially thinned from the standard substrate thickness of 620 μm to realise any cooling performance from the micro-cooler. This research work suggested that the substrate would have to be thinned to $<$50 μm and to be fabricated directly onto a thick gold plated heat-sink, to provide a good thermal

sink (as close to ideal as possible). This analysis would also apply to other semiconductor materials, for example InP based micro-coolers. The above research work and analysis suggests severe limitations to the use of micro-coolers as part of a MMIC approach. The author believes this was the first time an analysis was performed on an integrated micro-cooler as an element on a thick semi-insulating substrate.

7.5 Future work

Areas of continued research from this project work are:

- To develop an improved single micro-particle manipulation process, which does not require the removal of the bias probes for the repositioning of a micro-particle sensor. This will enable thermal profiles (of devices like the planar Gunn diode) to be completed without causing excess damage to the metallised contacts.
- To further develop the use of multiple micro-particle sensors for thermal profiling of an active device. However there are two questions:
    1. Will multiple micro-particles cause excessive thermal loading, reducing the thermal spatial resolution compared to a single micro-particle?
    2. Will multiple micro-particles interfere with the electromagnetic behaviour of the device when operating in transient mode or under RF conditions?
- To more completely analyse the lateral current flow in the micro-cooler will require 2D and 3D models to be developed to model the superlattice micro-cooler structures.
- To compare the specific contact resistivity (ρ_C) of both the anode and cathode contacts on the micro-cooler. These will differ due to the metallised contacts being deposited on different semiconductor contacting layers of the micro-cooler wafer specification. TLM structures will be needed on both the highly doped contacting layer at the top of the mesa (for the cathode contact) and on the second highly doped contacting layer, which was exposed by etching away the top mesa semiconductor layers (for the anode contact).
- To investigate novel geometrical and material structures to improve the ΔT cooling performance of micro-coolers fabricated as an on-wafer element.

- To further develop models and fabrication processes to enable direct integration of active power/small signal devices on an active micro-cooler.

Appendix A1

$$\Delta\mathrm{T} = \Theta_\mathrm{C}\left[\mathrm{I}\left(\phi + \frac{2\mathrm{k}\cdot\mathrm{T_{amb}}}{\mathrm{q}}\right) - \mathrm{I}^2\left(\tfrac{1}{2}\mathrm{R_{SL}} + \mathrm{R_{TC}}\right)\right] \quad (6.8) \tag{1}$$

$\Delta\mathrm{T_{max}}$ occurs at current $\mathrm{I} = \mathrm{I_{opt}}$ and when $\frac{\mathrm{d}\Delta\mathrm{T}}{\mathrm{dI}} = 0$

$$\begin{aligned}
\text{Since } \frac{\mathrm{d}\Delta\mathrm{T}}{\mathrm{dI}} &= \Theta_\mathrm{C}\left[\phi + \frac{2\mathrm{k}\cdot\mathrm{T_{amb}}}{\mathrm{q}} - 2\mathrm{I}\left(\tfrac{1}{2}\mathrm{R_{SL}} + \mathrm{R_{TC}}\right)\right] \\
0 &= \Theta_\mathrm{C}\left[\phi + \frac{2\mathrm{k}\cdot\mathrm{T_{amb}}}{\mathrm{q}} - \mathrm{I_{opt}}\left(\mathrm{R_{SL}} + 2\mathrm{R_{TC}}\right)\right] \\
&= \phi + \frac{2\mathrm{k}\cdot\mathrm{T_{amb}}}{\mathrm{q}} - \mathrm{I_{opt}}\left(\mathrm{R_{SL}} + 2\mathrm{R_{TC}}\right) \\
\mathrm{I_{opt}}\left(\mathrm{R_{SL}} + 2\mathrm{R_{TC}}\right) &= \phi + \frac{2\mathrm{k}\cdot\mathrm{T_{amb}}}{\mathrm{q}} \\
\mathrm{I_{opt}} &= \frac{\phi + \frac{2\mathrm{k}\cdot\mathrm{T_{amb}}}{\mathrm{q}}}{\mathrm{R_{SL}} + 2\mathrm{R_{TC}}} \qquad (2)
\end{aligned}$$

(2) ⇒ (1)

$$\begin{aligned}
\Delta\mathrm{T_{max}} &= \Theta_\mathrm{C}\left[\left(\phi + \frac{2\mathrm{k}\cdot\mathrm{T_{amb}}}{\mathrm{q}}\right)\mathrm{I_{opt}} - \mathrm{I_{opt}^2}\left(\tfrac{1}{2}\mathrm{R_{SL}} + \mathrm{R_{TC}}\right)\right] \\
&= \Theta_\mathrm{C}\left[\frac{\left(\phi + \frac{2\mathrm{k}\cdot\mathrm{T_{amb}}}{\mathrm{q}}\right)^2}{\left(\mathrm{R_{SL}} + 2\mathrm{R_{TC}}\right)} - \frac{\left(\phi + \frac{2\mathrm{k}\cdot\mathrm{T_{amb}}}{\mathrm{q}}\right)^2\left(\tfrac{1}{2}\mathrm{R_{SL}} + \mathrm{R_{TC}}\right)}{\left(\mathrm{R_{SL}} + 2\mathrm{R_{TC}}\right)^2}\right] \\
&= \Theta_\mathrm{C}\left[\frac{2\left(\phi + \frac{2\mathrm{k}\cdot\mathrm{T_{amb}}}{\mathrm{q}}\right)^2}{2\left(\mathrm{R_{SL}} + 2\mathrm{R_{TC}}\right)} - \frac{\left(\phi + \frac{2\mathrm{k}\cdot\mathrm{T_{amb}}}{\mathrm{q}}\right)^2\left(\mathrm{R_{SL}} + 2\mathrm{R_{TC}}\right)}{2\left(\mathrm{R_{SL}} + 2\mathrm{R_{TC}}\right)^2}\right] \\
&= \Theta_\mathrm{C}\left[\frac{2\left(\phi + \frac{2\mathrm{k}\cdot\mathrm{T_{amb}}}{\mathrm{q}}\right)^2}{2\left(\mathrm{R_{SL}} + 2\mathrm{R_{TC}}\right)} - \frac{\left(\phi + \frac{2\mathrm{k}\cdot\mathrm{T_{amb}}}{\mathrm{q}}\right)^2}{2\left(\mathrm{R_{SL}} + 2\mathrm{R_{TC}}\right)}\right]
\end{aligned}$$

$$
\begin{aligned}
&= \Theta_C \left[\frac{\left(\phi + \frac{2k \cdot T_{amb}}{q}\right)^2}{2\left(R_{SL} + 2R_{TC}\right)} \right] \\
&= \frac{\Theta_C}{2R_{SL} + 4R_{TC}} \left(\phi + \frac{2k \cdot T_{amb}}{q}\right)^2 \qquad (6.9)
\end{aligned}
$$

Since $\Theta_C = \frac{d_B}{\kappa \cdot A}$, $R_{SL} = \frac{d_B}{\sigma \cdot A}$, and $R_{TC} = \frac{\rho_C}{A}$

$$
\begin{aligned}
\Delta T_{max} &= \frac{\frac{d_B}{\kappa \cdot A}}{\frac{2d}{\sigma \cdot A} + \frac{4\rho_C}{A}} \left(\phi + \frac{2k \cdot T_{amb}}{q}\right)^2 \\
&= \frac{d \cdot A \cdot \sigma}{\kappa \cdot A(2d + 4\rho_C \cdot \sigma)} \left(\phi + \frac{2k \cdot T_{amb}}{q}\right)^2 \\
&= \frac{d \cdot \sigma}{\kappa(2d + 4\rho_C \cdot \sigma)} \left(\phi + \frac{2k \cdot T_{amb}}{q}\right)^2 \\
&= \frac{d \cdot \sigma}{2\kappa(d + 2\rho_C \cdot \sigma)} \left(\phi + \frac{2k \cdot T_{amb}}{q}\right)^2 \\
&= \frac{\sigma}{2\kappa(1 + \frac{2\rho_C \cdot \sigma}{d_B})} \left(\phi + \frac{2k \cdot T_{amb}}{q}\right)^2 \qquad (6.10)
\end{aligned}
$$

or

$$
\Delta T_{max} = \frac{d_B}{2\kappa(\frac{d_B}{\sigma} + 2\rho_C)} \left(\phi + \frac{2k \cdot T_{amb}}{q}\right)^2 \qquad (6.11)
$$

Appendix A2

Based on the fundamental thermoelectric equations:

$$\Delta T = T_h - T_c \quad (2.4) \tag{3}$$

Where T_h and T_c are the temperatures of the heated and cooled sides of the cooler, respectively.

$$\Delta T = \Theta_C(SIT_c - I^2R_{TC}) \quad (2.5) \tag{4}$$

Where Θ_C is the thermal impedance of the cooler, S is the Seebeck coefficient of the cooler, I is the current flowing through the cooler, and R_{TC} is the top contact resistance of the cooler (the resistance for the cooled contact).
Within equation (4), SIT_c is the cooling power and I^2R_{TC} is the self-heating power of the cooler.

$$P_C = SIT_c + I^2(R_{TC} + R_{BC}) \tag{5}$$

Where R_{BC} is the bottom contact resistance of the cooler (the resistance for the heated contact) and P_C is the total power output from the cooler. It is assumed that $R_{TC} + R_{BC} = R_{tot}$ (the total resistance of the cooler), and so $I^2(R_{TC} + R_{BC})$ is the input, bias, power to the cooler

$$\therefore \; T_h = T_{amb} + P_C\Theta_S \tag{6}$$

Where T_{amb} is the ambient temperature of the cooler and Θ_S is the thermal impedance of the substrate. Here T_h is the temperature rise due to the cooler being into of the substrate ($P_C\Theta_S$) above T_{amb}.

Rearranging equation (3) gives:

$$T_c = T_h - \Delta T \tag{7}$$

(6) & (4) ⇒ (7)

$$\mathrm{T_c = T_{amb} + P_C\Theta_S - \Theta_C(SIT_c - I^2R_{TC})} \tag{8}$$

(5) ⇒ (8)

$$\begin{aligned}\mathrm{T_c} &= \mathrm{T_{amb} + [SIT_c + I^2(R_{TC} + R_{BC})]\Theta_S - \Theta_C(SIT_c - I^2R_{TC})} \\ &= \mathrm{T_{amb} + \Theta_S SIT_c + \Theta_S I^2R_{TC} + \Theta_S I^2R_{BC} - \Theta_C SIT_c + \Theta_C I^2R_{TC}} \end{aligned} \tag{9}$$

Rearranging equation (6) gives:

$$\mathrm{T_{amb} = T_h - P_C\Theta_S} \tag{10}$$

(10) ⇒ (9)

$$\mathrm{T_c = T_h - P_C\Theta_S + \Theta_S SIT_c + \Theta_S I^2R_{TC} + \Theta_S I^2R_{BC} + \Theta_C I^2R_{TC} - \Theta_C SIT_c} \tag{11}$$

(5) ⇒ (11)

$$\begin{aligned}\mathrm{T_c = T_h} &\mathrm{- [SIT_c + I^2(R_{TC} + R_{BC})]\Theta_S + \Theta_S SIT_c + \Theta_S I^2R_{TC}} \\ &\mathrm{+ \Theta_S I^2R_{BC} + \Theta_C I^2R_{TC} - \Theta_C SIT_c}\end{aligned}$$

$$\begin{aligned}\mathrm{T_c = T_h} &\mathrm{- \Theta_S SIT_c - \Theta_S I^2R_{TC} - \Theta_S I^2R_{BC}} \\ &\mathrm{+ \Theta_S SIT_c + \Theta_S I^2R_{TC} + \Theta_S I^2R_{BC} + \Theta_C I^2R_{TC} - \Theta_C SIT_c}\end{aligned}$$

$$\begin{aligned}\mathrm{T_c} &= \mathrm{T_h + \Theta_C I^2R_{TC} - \Theta_C SIT_c} \\ \mathrm{T_c + \Theta_C SIT_c} &= \mathrm{T_h + \Theta_C I^2R_{TC}} \\ \mathrm{T_c(1 + \Theta_C SI)} &= \mathrm{T_h + \Theta_C I^2R_{TC}} \\ \mathrm{T_c} &= \mathrm{\frac{T_h + \Theta_C I^2R_{TC}}{1 + \Theta_C SI}}\end{aligned} \tag{12}$$

Equation (4) can be rewritten as:

$$\mathrm{\Delta T = \Theta_C SIT_c - \Theta_C I^2R_{TC}} \tag{13}$$

(12) ⇒ (13)

$$\mathrm{\Delta T = \Theta_C SI\left(\frac{T_h + \Theta_C I^2R_{TC}}{1 + \Theta_C SI}\right) - \Theta_C I^2R_{TC}}$$

$$
\begin{aligned}
&= \frac{\Theta_C SIT_h + \Theta_C^2 SI^3 R_{TC}}{1+\Theta_C SI} - \frac{\Theta_C I^2 R_{TC}(1+\Theta_C SI)}{1+\Theta_C SI} \\
&= \frac{\Theta_C SIT_h + \Theta_C^2 SI^3 R_{TC} - \Theta_C^2 SI^3 R_{TC} - \Theta_C I^2 R_{TC}}{1+\Theta_C SI} \\
&= \frac{\Theta_C SIT_h - \Theta_C I^2 R_{TC}}{1+\Theta_C SI} \qquad (14)
\end{aligned}
$$

(6) $\Rightarrow$ (14)

$$
\begin{aligned}
\Delta T &= \frac{\Theta_C SI(T_{amb} + P_C \Theta_S) - \Theta_C I^2 R_{TC}}{1+\Theta_C SI} \\
&= \frac{\Theta_C SIT_{amb} + P_C \Theta_S \Theta_C SI - \Theta_C I^2 R_{TC}}{1+\Theta_C SI} \qquad (15)
\end{aligned}
$$

(5) $\Rightarrow$ (15)

$$
\begin{aligned}
\Delta T &= \frac{\Theta_C SIT_{amb} + (SIT_c + I^2 R_{TC} + I^2 R_{BC})\Theta_S \Theta_C SI - \Theta_C I^2 R_{TC}}{1+\Theta_C SI} \\
&= \frac{\Theta_C SIT_{amb} + \Theta_S \Theta_C S^2 I^2 T_c + \Theta_S \Theta_C SI^3 R_{TC} + \Theta_S \Theta_C SI^3 R_{BC} - \Theta_C I^2 R_{TC}}{1+\Theta_C SI} \\
&= \frac{\Theta_C SIT_{amb} + \Theta_C I^2 R_{TC}(\Theta_S SI - 1) + \Theta_S \Theta_C SI^3 R_{BC} + \Theta_S \Theta_C S^2 I^2 T_c}{1+\Theta_C SI}
\end{aligned}
$$

The Seebeck coefficient (S) in particular for IIIV compounds is relatively small and therefore in a normal operating range of currents (I) it was assumed that $\Theta_S \Theta_C S^2 I^2 T_c$ tends to zero:

$$
\therefore\ \Delta T = \frac{\Theta_C SIT_{amb} + \Theta_C I^2 R_{TC}(\Theta_S SI - 1) + \Theta_S \Theta_C SI^3 R_{BC}}{1+\Theta_C SI} \qquad (6.16)
$$

Appendix B1

Model to match Shakouri's results

```
clear all;
%Cold Contact, T_C (K)
Tc=300;

%Boltzmann Constant, k (J/K)
k=1.3806488e-23;

%Electron Charge, e (C)
e=1.602176565e-19;

%Electron relaxation length, lambda_E
    %(m)
    Lre_m=0.4e-6;
%(cm)
Lre=Lre_m*100;

%Thermal Conductivity, kappa
    %(W/[m K])
    kappa_m=4;
%(W/[cm K])
kappa=kappa_m/100;

%Maximum Temperature Diffeence between hot and cold
   contacts, DT_max (K)
dTmax=10;

%Dimensions of cooler
    %Length of cooler (plan view) (m)
```

```
28      L=90e-6;
29      %Width of cooler (plan view) (m)
30      W=180e-6;
31      %Area (m^2)
32      A_m=L*W;
33  %Area (cm^2)
34  A=A_m*10000;
35
36  %Mobility, mu
37      %(m^2/V s)
38      mob_m=1.5;
39  %(cm^2/V s)
40  mob=mob_m*10000;
41
42  %Carrier concentration (cm^-3)
43  N=2e17;
44
45  %Resistivity, rho (Ohm cm)
46  res=1/(e*mob*N);
47
48  V=0.085;
49
50  for i=1:28
51      %Depth of barrier (um)
52      D=[0.1 0.2 0.3 0.4 0.5 0.6 0.7 0.8 0.9 1 2 3 4 5 6
           7 8 9 10 20 30 40 50 60 70 80 90 100];
53
54      %Depth of barrier (cm)
55      d(i)=D(i)/10000;
56
57      %Resistance of Barrier (Ohm)
58      R(i)=res*d(i)/A;
59
60      for a=1:3
61          %Barrier Height, Phi (eV)
62          Bh=[0.03 0.04 0.05];
63          if Bh(a)==0.03
64              %Current Density (A/cm^2) - Taken from plot
                     in 1998 paper
65              Aj=[1.25e5 1.16e5 1.1e5 1.02e5 9.7e4 9e4
                    8.6e4 8.3e4 7.9e4 7.5e4 5.3e4 4e4 3.2e4
```

```
            2.8e4 2.3e4 2e4 1.8e4 1.6e4 1.5e4 8e3 6
            e3 5e3 4e3 3e3 2.5e3 2e3 2e3 2e3];
66
67          %Thermionic Cooling Power (W/cm^2)
68          AQt(i)=Aj(i)*(Bh(a)+2*k*Tc/e);
69
70          %Joule (or Ohmic) Heating Power (W/cm^2)
71          AQjh(i)=Aj(i)*V*(0.5-(Lre/d(i))-((Lre/d(i))
            ^2)*(exp(-d(i)/Lre)-1));
72
73      elseif Bh(a)==0.04
74          %Current Density (A/cm^2) - Taken from plot
             in 1998 paper
75          Bj=[8.5e4 8e4 7.5e4 7e4 6.6e4 6.2e4 5.9e4
            5.6e4 5.5e4 5.2e4 3.5e4 2.8e4 2.2e4 1.9
            e4 1.7e4 1.4e4 1.2e4 1.1e4 1e4 5e3 4e3 3
            e3 2e3 2e3 1e3 1e3 1e3 1e3];
76
77          %Thermionic Cooling Power (W/cm^2)
78          BQt(i)=Bj(i)*(Bh(a)+2*k*Tc/e);
79
80          %Joule (or Ohmic) Heating Power (W/cm^2)
81          BQjh(i)=Bj(i)*V*(0.5-(Lre/d(i))-((Lre/d(i))
            ^2)*(exp(-d(i)/Lre)-1));
82
83      elseif Bh(a)==0.05
84          %Current Density (A/cm^2) - Taken from plot
             in 1998 paper
85          Cj=[5.8e4 5.4e4 5e4 4.7e4 4.5e4 4.3e4 4e4
            3.8e4 3.7e4 3.5e4 2.3e4 1.9e4 1.5e4 1.2
            e4 1.1e4 1e4 8e3 7e3 6e3 4e3 3e3 2e3 2e3
             2e3 1e3 1e3 1e3 1e3];
86
87          %Thermionic Cooling Power (W/cm^2)
88          CQt(i)=Cj(i)*(Bh(a)+2*k*Tc/e);
89
90          %Joule (or Ohmic) Heating Power (W/cm^2)
91          CQjh(i)=Cj(i)*V*(0.5-(Lre/d(i))-((Lre/d(i))
            ^2)*(exp(-d(i)/Lre)-1));
92      end
93  end
```

```
    %Heat Conduction Power (W/cm^2)
    Qhc(i)=kappa*dTmax/d(i);

    %Net Cooling Power (W/cm^2)
    AQ(i)=AQt(i)-AQjh(i)-Qhc(i);
    BQ(i)=BQt(i)-BQjh(i)-Qhc(i);
    CQ(i)=CQt(i)-CQjh(i)-Qhc(i);
end
figure(1); semilogx(D,AQ); axis([0.1 100 0 800]); xlabel('Barrier thickness, d (microns)'); ylabel('Net Cooling Power, Q (W/cm^2)'); title('Phi=0.03')

figure(2); semilogx(D,BQ); axis([0.1 100 0 800]); xlabel('Barrier thickness, d (microns)'); ylabel('Net Cooling Power, Q (W/cm^2)'); title('Phi=0.04')

figure(3); semilogx(D,CQ); axis([0.1 100 0 800]); xlabel('Barrier thickness, d (microns)'); ylabel('Net Cooling Power, Q (W/cm^2)'); title('Phi=0.04')

figure(4); subplot(2,2,1); semilogx(D,AQt); axis tight; title('Thermionic Cooling Power')
figure(4); subplot(2,2,2); semilogx(D,AQjh); axis tight; title('Joule Heating Power')
figure(4); subplot(2,2,3); semilogx(D,Qhc); axis tight; title('Heat Conduction Power')
figure(4); subplot(2,2,4); semilogx(D,AQ); axis tight; title('Net Cooling Power')

figure(5); subplot(2,2,1); semilogx(D,BQt); axis tight; title('Thermionic Cooling Power')
figure(5); subplot(2,2,2); semilogx(D,BQjh); axis tight; title('Joule Heating Power')
figure(5); subplot(2,2,3); semilogx(D,Qhc); axis tight; title('Heat Conduction Power')
figure(5); subplot(2,2,4); semilogx(D,BQ); axis tight; title('Net Cooling Power')

figure(6); subplot(2,2,1); semilogx(D,CQt); axis tight; title('Thermionic Cooling Power')
```

```
120 figure(6); subplot(2,2,2); semilogx(D,CQjh); axis tight; title('Joule Heating Power')
121 figure(6); subplot(2,2,3); semilogx(D,Qhc); axis tight; title('Heat Conduction Power')
122 figure(6); subplot(2,2,4); semilogx(D,CQ); axis tight; title('Net Cooling Power')
123
124 figure(7); semilogx(D,AQ,D,BQ,D,CQ); axis([0.1 100 0 1000]); xlabel('barrier thickness, d_B ( m)'); ylabel('net cooling power density, Qd (W/cm )')
```

Appendix B2

Model to match Shakouri's results (with improved current density values)

```
clear all;
%Cold Contact, T_C (K)
Tc=300;

%Boltzmann Constant, k (J/K)
k=1.3806488e-23;

%Electron Charge, e (C)
e=1.602176565e-19;

%Electron relaxation length, lambda_E
    %(m)
    Lre_m=0.4e-6;
%(cm)
Lre=Lre_m*100;

%Thermal Conductivity, kappa
    %(W/[m K])
    kappa_m=4;
%(W/[cm K])
kappa=kappa_m/100;

%Maximum Temperature Diffeence between hot and cold
   contacts, DT_max (K)
dTmax=10;

```

```
26 %Dimensions of cooler
27     %Length of cooler (plan view) (m)
28     L=90e-6;
29     %Width of cooler (plan view) (m)
30     W=180e-6;
31     %Area (m^2)
32     A_m=L*W;
33 %Area (cm^2)
34 A=A_m*10000;
35
36 %Mobility, mu
37     %(m^2/V s)
38     mob_m=1.5;
39 %(cm^2/V s)
40 mob=mob_m*10000;
41
42 %Carrier concentration (cm^-3)
43 N=2e17;
44
45 %Resistivity, rho (Ohm cm)
46 res=1/(e*mob*N);
47
48 for i=1:1000
49     %Depth of barrier (um)
50     D(i)=i/10;
51
52     %Depth of barrier (cm)
53     d(i)=D(i)/10000;
54
55     %Resistance of Barrier (Ohm)
56     R(i)=res*d(i)/A;
57
58     for a=1:3
59         %Barrier Height, Phi (eV)
60         Bh=[0.03 0.04 0.05];
61         if Bh(a)==0.03
62             %Current Density (A/cm^2)
63             Aj(i)=112.4770*d(i)^-0.6824;
64
65             %Thermionic Cooling Power (W/cm^2)
66             AQt(i)=Aj(i)*(Bh(a)+2*k*Tc/e);
```

```
67
68              %Joule (or Ohmic) Heating Power (W/cm^2)
69              AQjh(i)=(Aj(i))^2*A*R(i)*(0.5-(Lre/d(i))-((
                   Lre/d(i))^2)*(exp(-d(i)/Lre)-1));
70
71          elseif Bh(a)==0.04
72              %Current Density (A/cm^2) - Taken from plot
                    in 1998 paper
73              Bj(i)=49.9412*d(i)^-0.7295;
74
75              %Thermionic Cooling Power (W/cm^2)
76              BQt(i)=Bj(i)*(Bh(a)+2*k*Tc/e);
77
78              %Joule (or Ohmic) Heating Power (W/cm^2)
79              BQjh(i)=(Bj(i))^2*A*R(i)*(0.5-(Lre/d(i))-((
                   Lre/d(i))^2)*(exp(-d(i)/Lre)-1));
80
81          elseif Bh(a)==0.05
82              %Current Density (A/cm^2) - Taken from plot
                    in 1998 paper
83              Cj(i)=56.9543*d(i)^-0.6723;
84
85              %Thermionic Cooling Power (W/cm^2)
86              CQt(i)=Cj(i)*(Bh(a)+2*k*Tc/e);
87
88              %Joule (or Ohmic) Heating Power (W/cm^2)
89              CQjh(i)=(Cj(i))^2*A*R(i)*(0.5-(Lre/d(i))-((
                   Lre/d(i))^2)*(exp(-d(i)/Lre)-1));
90          end
91      end
92
93      %Heat Conduction Power (W/cm^2)
94      Qhc(i)=kappa*dTmax/d(i);
95
96      %Net Cooling Power (W/cm^2)
97      AQ(i)=AQt(i)-AQjh(i)-Qhc(i);
98      BQ(i)=BQt(i)-BQjh(i)-Qhc(i);
99      CQ(i)=CQt(i)-CQjh(i)-Qhc(i);
100 end
101 figure(1); semilogx(D,AQ); axis([0.1 100 0 1000]);
       xlabel('Barrier thickness, d (um)'); ylabel('Net
```

```
    Cooling Power, Q (W/cm^2)'); title('Phi=0.03')
102
103 figure(2); semilogx(D,BQ); axis([0.1 100 0 1000]);
    xlabel('Barrier thickness, d (um)'); ylabel('Net
    Cooling Power, Q (W/cm^2)'); title('Phi=0.04')
104
105 figure(3); semilogx(D,CQ); axis([0.1 100 0 1000]);
    xlabel('Barrier thickness, d (um)'); ylabel('Net
    Cooling Power, Q (W/cm^2)'); title('Phi=0.04')
106
107 figure(4); subplot(2,2,1); semilogx(D,AQt); axis tight;
     title('Thermionic Cooling Power')
108 figure(4); subplot(2,2,2); semilogx(D,AQjh); axis tight
    ; title('Joule Heating Power')
109 figure(4); subplot(2,2,3); semilogx(D,Qhc); axis tight;
     title('Heat Conduction Power')
110 figure(4); subplot(2,2,4); semilogx(D,AQ); axis tight;
    title('Net Cooling Power')
111
112 figure(5); subplot(2,2,1); semilogx(D,BQt); axis tight;
     title('Thermionic Cooling Power')
113 figure(5); subplot(2,2,2); semilogx(D,BQjh); axis tight
    ; title('Joule Heating Power')
114 figure(5); subplot(2,2,3); semilogx(D,Qhc); axis tight;
     title('Heat Conduction Power')
115 figure(5); subplot(2,2,4); semilogx(D,BQ); axis tight;
    title('Net Cooling Power')
116
117 figure(6); subplot(2,2,1); semilogx(D,CQt); axis tight;
     title('Thermionic Cooling Power')
118 figure(6); subplot(2,2,2); semilogx(D,CQjh); axis tight
    ; title('Joule Heating Power')
119 figure(6); subplot(2,2,3); semilogx(D,Qhc); axis tight;
     title('Heat Conduction Power')
120 figure(6); subplot(2,2,4); semilogx(D,CQ); axis tight;
    title('Net Cooling Power')
121
122 figure(7); semilogx(D,AQ,D,BQ,D,CQ); axis([0.1 100 0
    1000]); xlabel('barrier thickness, d_B (um)');
    ylabel('net cooling power density, Qd (W/cm^2)')
```

Appendix B3

Effects of ρ_C on ΔT_{max}

```
clear all
%CONSTANTS - do not alter%
% Boltzmann Constant, k (J/ K)
k=1.3806488e-23;
% Electronic Charge, e (C)
e=1.602176565e-19;

    %REQUIRED VALUES - must not be zero%
% Barrier Height,    (eV) - Calculations on Log Book 3
bh=0.25;
% Ambient Temperature ( K)
Tamb=300;

    %ADDITIONAL VALUES - if not required/unknown set to
        zero%
% Length of top contact, L (m)
L_m=100e-6; % zero if unknown

% Width of top contact, W (m)
W_m=100e-6; % zero if unknown

% Area of top contact, A
A_m=1e-8; % Manually set AREA (m^2)
% (cm^2)
if L_m == 0 || W_m == 0
    A=A_m*10000;
else
    A=L_m*W_m*10000;
```

```
28 end
29
30 % Thickness of active region
31     % (m)
32     d_m=2e-6;
33 % (cm)
34 d=d_m*100;
35
36 % Specific thermal conductivity of active region, K (W
   /[cm  K])
37 K=0.55; % zero if unknown
38 % Thermal Resistance, R_th (  K/W)
39 if K == 0
40     Rth=7.14; % Manually set THERMAL RESISTANCE
41 else
42     Rth=d/(K*A);
43 end
44
45 % Mobility of active region,    (cm^2/[V s})
46 mob=8.5e3; % zero if unknown
47 % Carrier consentration of active region, N (cm^-3)
48 N=5e15; % zero  if unknown
49 % Conductivity of active region,    (S/m) | (1/[   m])
50 if mob == 0 || N == 0
51     cond=0; % Manually set CONDUCTIVITY
52 else
53     cond=e*mob*N;
54 end
55 % Resistivity of active region,    (   m)
56 if cond == 0
57     res=6.9e-4; % Manually set RESISTIVITY
58 else
59     res=1/cond;
60 end
61 % Resistance of active region (  )
62 if res == 0
63     R=1.38e-3; % Manually set RESISTANCE
64 else
65     R=d*res/A;
66 end
67
```

```
68  % Specific contact restance, r_c |   _c (    cm^2)
69  for j=1:100
70
71      rc(j)=j^2*1e-8;
72      Rc(j)=rc(j)/A;
73      Rtot(j)=2*Rc(j)+R;
74
75
76      % Temperature Difference,   T (  K)
77      % Tmax = ( Rth / (2Rsl+4Rtc) )*( (    + 2 k T_amb)
           / e )^2%
78      dTmax(j)=(Rth/(2*R+4*Rc(j)))*(bh+((2*k*Tamb)/e))*(
           bh+((2*k*Tamb)/e));
79  end
80
81  semilogx(rc,dTmax,'LineWidth',3); set(gca,'FontSize'
       ,32); axis([1e-8,1e-4,0,0.6]); %xlabel('specific
       contact resistivity,   _c (    cm )'); ylabel('
        T_max (K)');
```

Appendix B4

How cooling performance changes with the contact resistance

```
clear all
%CONSTANTS - do not alter%
% Boltzmann Constant, k (J/K)
k=1.3806488e-23;
% Electronic Charge, e (C)
e=1.602176565e-19;

    %REQUIRED VALUES - must not be zero%
% Barrier Height, Phi (eV) - Calculations on Log Book 3
bh=0.25;
% Ambient Temperature (K)
Tamb=300;

    %ADDITIONAL VALUES - if not required/unknown set to
        zero%
% Length of top contact, L (m)
L_m=100e-6; % zero if unknown

% Width of top contact, W (m)
W_m=100e-6; % zero if unknown

% Area of top contact, A
A_m=1e-8; % Manually set AREA (m^2)
% (cm^2)
if L_m == 0 || W_m == 0
    A=A_m*10000;
```

```
26 else
27     A=L_m*W_m*10000;
28 end
29
30 % Thickness of active region
31     % (m)
32     d_m=2e-6;
33 % (cm)
34 d=d_m*100;
35
36 % Specific thermal conductivity of active region, K (W
   /[cm K])
37 K=0.55; % zero if unknown
38 % Thermal Resistance, R_th (K/W)
39 if K == 0
40     Rth=7.14; % Manually set THERMAL RESISTANCE
41 else
42     Rth=d/(K*A);
43 end
44
45 % Mobility of active region, mu (cm^2/[V s])
46 mob=8.5e3; % zero if unknown
47 % Carrier consentration of active region, N (cm^-3)
48 N=5e15; % zero  if unknown
49 % Conductivity of active region, sigma (S/m) | (1/[Ohm
   m])
50 if mob == 0 || N == 0
51     cond=0; % Manually set CONDUCTIVITY
52 else
53     cond=e*mob*N;
54 end
55 % Resistivity of active region, rho (Ohm m)
56 if cond == 0
57     res=6.9e-4; % Manually set RESISTIVITY
58 else
59     res=1/cond;
60 end
61 % Resistance of active region (Ohm)
62 if res == 0
63     R=1.38e-3; % Manually set RESISTANCE
64 else
```

```
65      R=d*res/A;
66  end
67
68  for i=1:2000
69      % Current (A)
70      I(i)=i/1000;
71
72      % Temperature Difference,   T (K)
73      %DT = Rth [ (Phi + 2 k T_amb / e) I      I^2 (0.5R +
           R_c) ]%
74      for j=1:4
75          if j == 1
76              rc=1e-4;
77              Rc=rc/A;
78              dTa(i)=Rth*((bh+2*k*Tamb/e)*I(i)-I(i)
                   ^2*(0.5*R+Rc));
79          elseif j ==2
80              rc=1e-5;
81              Rc=rc/A;
82              dTb(i)=Rth*((bh+2*k*Tamb/e)*I(i)-I(i)
                   ^2*(0.5*R+Rc));
83          elseif j ==3
84              rc=1e-6;
85              Rc=rc/A;
86              dTc(i)=Rth*((bh+2*k*Tamb/e)*I(i)-I(i)
                   ^2*(0.5*R+Rc));
87          else
88              rc=1e-7;
89              Rc=rc/A;
90              dTd(i)=Rth*((bh+2*k*Tamb/e)*I(i)-I(i)
                   ^2*(0.5*R+Rc));
91          end
92      end
93  end
94
95  %Current vs DT
96  figure(1); plot(I,dTa,I,dTb,I,dTc,I,dTd); axis([0 2 -2
       0.65]); xlabel('current, I (A)'); ylabel('DT (K)');
97  figure(2); plot(I,dTa,I,dTb,I,dTc,I,dTd); axis([0 0.2 0
       0.2]); xlabel('current, I (A)'); ylabel('DT (K)');
```

Appendix B5

Thermal conductivity for III-V semiconductor alloys

```
clear all

AlAs1=1.1; %cm K/W - Adachi's thermal conductivity (W)
   for AlAs
AlAs2=1.25; %cm K/W - Palankovski's thermal
   conductivity (W) for AlAs
GaAs=2.22; %cm K/W - Adachi's thermal conductivity (W)
   for GaAs
InAs=3.3; %cm K/W - Adachi's thermal conductivity (W)
   for InAs

for i=1:101;
    x(i)=(i-1)/100;

    %Al_{x}Ga_{1-x}As based on Adachi's W for AlAs
    AlGaAs1(i)=1/(x(i)*AlAs1+(1-x(i))*GaAs+x(i)*(1-x(i)
       )*32);
    %Al_{x}Ga_{1-x}As based on Palakovski's W for AlAs
    AlGaAs2(i)=1/(x(i)*AlAs2+(1-x(i))*GaAs+x(i)*(1-x(i)
       )*32);

    %In_{1-x}Al_{x}As based on Adachi's W for AlAs
    InAlAs1(i)=1/(x(i)*AlAs1+(1-x(i))*InAs+x(i)*(1-x(i)
       )*15);
    %In_{1-x}Al_{x}As based on Palakovski's W for AlAs
```

```
19      InAlAs2(i)=1/(x(i)*AlAs2+(1-x(i))*InAs+x(i)*(1-x(i)
           )*15);
20
21      %In_{1-x}Ga_{x}As
22      InGaAs(i)=1/(x(i)*GaAs+(1-x(i))*InAs+x(i)*(1-x(i))
           *72);
23  end
24  x1=[0.16 0.23 0.30 0.35 0.48 0.56 0.68 0.79 0.88 0.91
       0.96 0.99];
25  K=[0.09 0.075 0.065 0.06 0.055 0.05 0.055 0.07 0.08
       0.16 0.185 0.215];
26
27  figure(1); plot(x,AlGaAs1,'b',x,AlGaAs2,'r'); axis
       ([0,1,0,1]); xlabel('x'); ylabel('thermal
       conductivity (W/cmK)'); title('Al{x}Ga{1-x}As');
28  figure(2); plot(x,InAlAs1,'b',x,InAlAs2,'r'); axis
       ([0,1,0,1]); xlabel('x'); ylabel('thermal
       conductivity (W/cmK)'); title('In{1-x}Al{x}As');
29  figure(3); plot(x,InGaAs,'b',x1,K,'go'); axis
       ([0,1,0,1]); xlabel('x'); ylabel('thermal
       conductivity (W/cmK)'); title('In{1-x}Ga{x}As');
```

Appendix B6

Comparing experimental results with model, for micro-cooler A9

```
clear all
%CONSTANTS - do not alter%
% Boltzmann Constant, k (J/ K)
k=1.3806488e-23;
% Electronic Charge, e (C)
e=1.602176565e-19;

    %REQUIRED VALUES - must not be zero%
% Barrier Height, phi (eV)
bh=0.3;
% Ambient Temperature (K)
Tamb=400;

    %ADDITIONAL VALUES - if not required/unknown set to
        zero%
% Length of top contact, L (m)
L_m=0; % zero if unknown

% Width of top contact, W (m)
W_m=0; % zero if unknown

% Area of top contact, A
A_m=1.23e-8; % Manually set AREA (m^2)
% (cm^2)
if L_m == 0 || W_m == 0
    A=A_m*10000;
```

```
26 else
27     A=L_m*W_m*10000;
28 end
29
30 % Thickness of active region
31     % (m)
32     d_m=2.1e-6;
33 % (cm)
34 d=d_m*100;
35
36 % Specific thermal conductivity of active region, kappa
      (W/[cm K])
37 K=0.1898; % zero if unknown
38 % Thermal Resistance, R_th (K/W)
39 if K == 0
40     Rth=7.14; % Manually set THERMAL RESISTANCE
41 else
42     Rth=d/(K*A);
43 end
44
45 % Mobility of active region, mu (cm^2/[V s})
46 mob=0; % zero if unknown
47 % Carrier consentration of active region, N (cm^-3)
48 N=0; % zero  if unknown
49 % Conductivity of active region, sigma (S/m) | (1/[Ohm
    m])
50 if mob == 0 || N == 0
51     cond=0; % Manually set CONDUCTIVITY
52 else
53     cond=e*mob*N;
54 end
55 % Resistivity of active region, rho (Ohm m)
56 if cond == 0
57     res=0; % Manually set RESISTIVITY
58 else
59     res=1/cond;
60 end
61 % Resistance of active region (Ohm)
62 if res == 0
63     R=0.3; % Manually set RESISTANCE
64 else
```

```
65     R=d*res/A; %internal res
66 end
67
68 % Specific contact restance, rho_c (Ohm cm^2)
69 rc=3e-5; % zero if unknown
70 % Contact Resistance (Ohm)
71 if rc == 0
72     Rc=0.1; % Manually set CONTACT RESISTANCE
73 else
74     Rc=rc/A;
75 end
76
77 for i=1:600
78     % Current (A)
79     I(i)=i/1000;
80
81     % Temperature Difference, DeltaT (K)
82     dT(i)=Rth*((bh+2*k*Tamb/e)*I(i)-I(i)^2*(0.5*R+Rc));
83 end
84 I2=[0.03,0.04,0.05,0.07,0.08,0.1,0.125];
85 DT=[0.1,0.1,0.2,0.1,0.2,0.2,0.4];
86
87 hold('on'); plot(I,dT,'b'); plot(I2,DT,'ro'); xlabel('
       current, I (A)'); ylabel(' T (K)');
```

References

[1] A. Khalid, N. J. Pilgrim, G. M. Dunn, M. C. Holland, C. R. Stanley, I. G. Thayne, and D. R. S. Cumming, "A Planar Gunn Diode Operating Above 100 GHz," *Electron Device Lett. IEEE*, vol. 28, no. 10, pp. 849–851, oct 2007. [Online]. Available: http://ieeexplore.ieee.org/lpdocs/epic03/wrapper.htm?arnumber=4317659 1, 18, 19, 21, 46, 71

[2] A. Khalid, C. Li, V. Papageorgiou, N. J. Pilgrim, G. M. Dunn, and D. R. S. Cumming, "A 218-GHz second-harmonic multiquantum well GaAs-based planar Gunn diodes," *Microw. Opt. Technol. Lett.*, vol. 55, no. 3, pp. 686–688, mar 2013. [Online]. Available: http://doi.wiley.com/10.1002/mop.27393http://eprints.gla.ac.uk/86366/ 1, 18, 22, 71

[3] C. Li, A. Khalid, S. H. P. Caldwell, N. J. Pilgrim, M. C. Holland, G. M. Dunn, I. G. Thayne, and D. R. S. Cumming, "Design and Fabrication of Pseudomorphic In0.23Ga0.77As-channel Planar Gunn Diodes," *(Unpublished - Glas.*, pp. 1–7, 2010. 1, 71

[4] C. Li, A. Khalid, N. J. Pilgrim, M. C. Holland, G. M. Dunn, and D. R. S. Cumming, "Novel planar Gunn diode operating in fundamental mode up to 158 GHz," *J. Phys. Conf. Ser.*, vol. 193, no. 1, pp. 1–4, nov 2009. [Online]. Available: http://stacks.iop.org/1742-6596/193/i=1/a=012029?key=crossref.e8fb48e5ec76f6fc6bb2c64d31a82385 1, 71

[5] A. Khalid, C. Li, V. Papageogiou, G. M. Dunn, M. J. Steer, I. G. Thayne, M. Kuball, C. H. Oxley, M. Montes Bajo, A. Stephen, J. Glover, and D. R. S. Cumming, "In_{0.53}Ga_{0.47}As Planar Gunn Diodes Operating at a Fundamental Frequency of 164 GHz," *IEEE Electron Device Lett.*, vol. 34, no. 1, pp. 39–41, jan 2013. [Online]. Available: http://ieeexplore.ieee.org/lpdocs/epic03/wrapper.htm?arnumber=6352833 1, 21, 46, 71

[6] M. I. Maricar, “Design of circuits to enhance the performance of high frequency planar Gunn diodes,” PhD Thesis, De Montfort University, Leicester, UK, 2014. 1, 20, 21, 22, 46, 50

[7] M. Kuball, D. R. S. Cumming, A. Khalid, C. H. Oxley, and G. M. Dunn, “Novel Thermal Management Concepts: High Power High Frequency Planar Gunn Diodes,” 2009. 1

[8] J. Glover, A. Khalid, D. R. S. Cumming, M. M. Bajo, M. Kuball, A. Stephen, G. M. Dunn, and C. H. Oxley, “On wafer thermal characterization of miniature gallium arsenide microcoolers with thermal loading from DC probes,” *Microw. Opt. Technol. Lett.*, vol. 56, no. 11, pp. 2699–2700, nov 2014. [Online]. Available: http://doi.wiley.com/10.1002/mop.28681 5, 88, 89, 90, 91

[9] J. Glover, A. Khalid, A. Stephen, G. Dunn, D. Cumming, and C. H. Oxley, “Micro-coolers fabricated as a component in an integrated circuit,” *Semicond. Sci. Technol.*, vol. 30, no. 1, p. 5, 2015. [Online]. Available: http://stacks.iop.org/0268-1242/30/i=1/a=015005?key=crossref.0114a5d9b30380593b394485df7f789d 5, 109, 110, 112

[10] T. Borca-Tasciuc, G. Chen, D. Wang, and K. L. Wang, “Thermal Conductivity Measurement and Microscopy of Thin Film Structures,” in *Thermoelectr. 1997. Proc. ICT '97. XVI Int. Conf.* IEEE, 1997, pp. 726–729. [Online]. Available: http://ieeexplore.ieee.org/lpdocs/epic03/wrapper.htm?arnumber=667632 8

[11] N. Killat, M. Montes, J. W. Pomeroy, T. Paskova, K. R. Evans, J. Leach, X. Li, U. Ozgur, H. Morkoc, K. D. Chabak, A. Crespo, J. K. Gillespie, R. Fitch, M. Kossler, D. E. Walker, M. Trejo, G. D. Via, J. D. Blevins, and M. Kuball, “Thermal Properties of AlGaN/GaN HFETs on Bulk GaN Substrates,” *IEEE Electron Device Lett.*, vol. 33, no. 3, pp. 366–368, mar 2012. [Online]. Available: http://zr7av6yc4v.scholar.serialssolutions.com/?sid=google{&}auinit=N{&}aulast=Killat{&}atitle=Thermal+properties+of+AlGaN/GaN+HFETs+on+bulk+GaN+substrates{&}id=doi:10.1109/LED.2011.2179972{&}title=IEEE+electron+device+letters{&}volume=33{&}issue=3{&}date=2012{&}spage=366{&} 9

[12] innovative products & systems, “Effects of low emissive wall coatings on thermal comfort and energy consumtion,” 2007. [Online]. Available: http://www.ips-innovations.com/low{_}emissive{_}wall{_}coatings{_}ref.htm 11

[13] P. W. Webb, "Thermal imaging of electronic devices with low surface emissivity," *Circuits, Devices Syst. IEE Proc. G*, vol. 138, no. 3, pp. 390–400, 1991. [Online]. Available: http://link.aip.org/link/IPGSEB/v138/i3/p390/s1{&}Agg=doihttp://ieeexplore.ieee.org/search/srchabstract.jsp?tp={&}arnumber=258031{&}queryText=p+w+webb{&}refinements=4294945219{&}openedRefinements=*{&}searchField=Search+All 13

[14] R. H. Hopper, "Accurate Temperature Measurements on Semiconductor Devices," PhD Thesis, De Montfort University, Leicester, UK, 2010. 15, 17, 36, 38

[15] C. H. Oxley, R. H. Hopper, D. Prime, M. Leaper, G. A. Evans, and A. Levick, "Probe propels IR thermal microscopy to a new level," *Compd. Semicond.*, vol. 17, no. February, pp. 33–36, 2011. [Online]. Available: http://compoundsemiconductor.net/csc/features-details.php?cat=features{&}id=19733175 15, 36, 42

[16] J. B. Gunn, "Microwave oscillations of current in IIIV semiconductors," *Solid State Commun.*, vol. 1, no. 4, pp. 88–91, sep 1963. [Online]. Available: http://linkinghub.elsevier.com/retrieve/pii/0038109863900413 17, 46

[17] ——, "Recent work on the direct generation of microwaves in bulk semiconductors," in *1963 Int. Electron Devices Meet.* IRE, 1963, pp. 24–24. [Online]. Available: http://ieeexplore.ieee.org/lpdocs/epic03/wrapper.htm?arnumber=1473589 17, 46

[18] ——, "Instabilities of Current in IIIV Semiconductors," *IBM J. Res. Dev.*, vol. 8, no. 2, pp. 141–159, apr 1964. [Online]. Available: http://ieeexplore.ieee.org/lpdocs/epic03/wrapper.htm?arnumber=5392214 17, 46

[19] B. K. Ridley and T. B. Watkins, "The Possibility of Negative Resistance Effects in Semiconductors," *Proc. Phys. Soc.*, vol. 78, no. 2, pp. 293–304, aug 1961. [Online]. Available: http://stacks.iop.org/0370-1328/78/i=2/a=315?key=crossref.38d9a6d14f2a7df5cd7a5853f91c3461 17

[20] H. Kroemer, "Theory of the Gunn effect," *Proc. IEEE*, vol. 52, no. 12, pp. 1736–1736, 1964. [Online]. Available: http://ieeexplore.ieee.org/lpdocs/epic03/wrapper.htm?arnumber=1445406 17

[21] J. S. Heeks, "Some properties of the moving high-field domain in Gunn effect devices," *IEEE Trans. Electron Devices*, vol. ED-13, no. 1, pp.

68–79, jan 1966. [Online]. Available: http://ieeexplore.ieee.org/lpdocs/epic03/wrapper.htm?arnumber=1474227 17

[22] W. H. Haydl, "Planar Gunn diodes with ideal contact geometry," *Proc. IEEE*, vol. 61, no. 4, p. 497, nov 1973. [Online]. Available: http://ieeexplore.ieee.org/search/srchabstract.jsp?tp={&}arnumber=1451020{&}queryText=planar+gunn+diodes+with+ideal+contact+geometry{&}openedRefinements=*{&}searchField=Search+Allhttp://ieeexplore.ieee.org/lpdocs/epic03/wrapper.htm?arnumber=1451020 18, 19, 46

[23] R. L. Franz, "Use Nonlinear Devices As Linchpins To Next-Generation Design," 2010. [Online]. Available: http://electronicdesign.com/archive/use-nonlinear-devices-linchpins-next-generation-design 18

[24] N. Priestley and N. Farrington, "Millimetre-Wave Gunn Diode Technology and," in *ARMMS RF Microw. Soc.*, 2010, pp. 1–10. [Online]. Available: http://www.armms.org/conferences/?conference=18http://www.armms.org/media/uploads/1326114401.pdf 18

[25] Y. P. Teoh, G. M. Dunn, N. E. Priestley, and M. Carr, "Monte Carlo simulations of asymmetry multiple transit region Gunn diodes," *Semicond. Sci. Technol.*, vol. 20, no. 5, pp. 418–422, may 2005. [Online]. Available: http://stacks.iop.org/0268-1242/20/i=5/a=016?key=crossref.3cb4f0e9a28df0187b1d0bd35d5dcfb0 19

[26] N. E. Priestley and B. Prime, "A Compact 77GHz Transceiver Module Using G3D Diode Technology for Automotive Applications," in *Adv. Microsystems Automot. Appl.* Berlin: Springer, 2003, pp. 175–188. [Online]. Available: http://link.springer.com/chapter/10.1007/978-3-540-76988-0{_}15 19

[27] A. Khalid, C. Li, N. J. Pilgrim, M. C. Holland, G. M. Dunn, and D. R. S. Cumming, "Novel composite contact design and fabrication for planar Gunn devices for millimeter-wave and terahertz frequencies," pp. 1–3, 2010. 21

[28] L. B. Lok, C. Li, A. Khalid, N. J. Pilgrim, G. M. Dunn, and D. R. S. Cumming, "Demonstration of the self-mixing effect with a planar gunn diode at millimeter-wave frequency," in *Infrared Millim. Terahertz Waves (IRMMW-THz), 2010 35th Int. Conf.*, 2010, pp. 1–2. [Online]. Available: http://ieeexplore.ieee.org/search/srchabstract.jsp?tp={&}arnumber=5612316{&}queryText=Demonstration+of+the+Self-Mixing+Effect+with+a+Planar+Gunn+Diode+at+Millimeter-Wave+Frequency{&}openedRefinements=*{&}searchField=Search+All{&}tag=1 21

[29] A. N. Broers, “Resolution limits for electron-beam lithography,” *IBM J. Res. Dev.*, vol. 32, no. 4, pp. 502–513, jul 1988. [Online]. Available: http://ieeexplore.ieee.org/lpdocs/epic03/wrapper.htm?arnumber=5390017 21, 22

[30] A. E. Grigorescu and C. W. Hagen, “Resists for sub-20-nm electron beam lithography with a focus on HSQ: state of the art,” *Nanotechnology*, vol. 20, no. 29, p. 31, 2009. [Online]. Available: http://stacks.iop.org/0957-4484/20/i=29/a=292001?key=crossref.a3e9e2549e2330c9c3157965afaa09ba 21, 22

[31] S. A. Rishton and D. P. Kern, “Point exposure distribution measurements for proximity correction in electron beam lithography on a sub-100 nm scale,” *J. Vac. Sci. Technol. B Microelectron. Nanom. Struct.*, vol. 5, no. 1, p. 135, jan 1987. [Online]. Available: http://scitation.aip.org/content/avs/journal/jvstb/5/1/10.1116/1.583847 21, 22

[32] C. Li, “Design and characterisation of millimetre wave planar Gunn diodes and integrated circuits,” PhD Thesis, University of Glasgow, Glasgow, UK, 2012. [Online]. Available: http://theses.gla.ac.uk/3117/ 22, 46, 50

[33] E2V, “E2V Technologies Gunn Diodes Application Notes,” Tech. Rep. 4, 2002. 22

[34] C. Wen, “Coplanar Waveguide: A Surface Strip Transmission Line Suitable for Nonreciprocal Gyromagnetic Device Applications,” *IEEE Trans. Microw. Theory Tech.*, vol. 17, no. 12, pp. 1087–1090, dec 1969. [Online]. Available: http://ieeexplore.ieee.org/lpdocs/epic03/wrapper.htm?arnumber=1127105 22

[35] S. Garimella, “Advances in mesoscale thermal management technologies for microelectronics,” *Microelectronics J.*, vol. 37, no. 11, pp. 1165–1185, nov 2006. [Online]. Available: http://linkinghub.elsevier.com/retrieve/pii/S0026269205003071 23

[36] B. Dang, M. S. Bakir, and J. D. Meindl, “Integrated thermal-fluidic I/O interconnects for an on-chip microchannel heat sink,” *Electron Device Lett. IEEE*, vol. 27, no. 2, pp. 117–119, feb 2006. [Online]. Available: http://ieeexplore.ieee.org/lpdocs/epic03/wrapper.htm?arnumber=1580600 23

[37] S. Godfrey, “An introduction to thermoelectric coolers,” pp. 1–6, 1996. [Online]. Available: http://www.electronics-cooling.com/1996/09/an-introduction-to-thermoelectric-coolers 23

[38] L. Rushing, A. Shakouri, P. Abraham, and J. E. Bowers, "Micro thermoelectric coolers for integrated applications," in *Thermoelectr. 1997. Proc. ICT '97. XVI Int. Conf.*, no. 1997. Ieee, 1997, pp. 646–649. [Online]. Available: http://ieeexplore.ieee.org/lpdocs/epic03/wrapper.htm?arnumber=667612 23, 30

[39] T. J. Seebeck, *Magnetische Polarisation der Metalle und Erze durch Temperatur-Differenz.* Leipzig W. Engelmann, 1825, vol. 1822-1823. [Online]. Available: https://archive.org/details/magnetischepolar00seebuofthttps://openlibrary.org/works/OL7842367W/Magnetische{_}Polarisation{_}der{_}Metalle{_}und{_}Erze{_}durch{_}Temperatur-Differenz{_}1822-1823 24

[40] J. C. A. Peltier, "Nouvelles Expériences sur la Caloricité des courans électriques," *Ann. Chim. Phys.*, vol. 56, no. i, pp. 371–386, 1834. 24

[41] Y. Zhang, Y. Chen, C. Gong, J. Yang, R. Qian, and Y. Wang, "Optimization of Superlattice Thermoelectric Materials and Microcoolers," *Microelectromechanical Syst. J.*, vol. 16, no. 5, pp. 1113–1119, oct 2007. [Online]. Available: http://ieeexplore.ieee.org/lpdocs/epic03/wrapper.htm?arnumber=4337813 26, 30, 31, 82

[42] Y. Zhang, G. Zeng, J. Piprek, A. Bar-Cohen, and A. Shakouri, "Superlattice microrefrigerators fusion bonded with optoelectronic devices," *Components Packag. Technol. IEEE Trans.*, vol. 28, no. 4, pp. 658–666, dec 2005. [Online]. Available: http://ieeexplore.ieee.org/lpdocs/epic03/wrapper.htm?arnumber=1546171 26, 99

[43] Y. Zhang, G. Zeng, C. Hoffman, A. Bar-Cohen, and A. Shakouri, "Enhanced Hot Spot Cooling Using Bonded Superlattice Microcoolers With a Trench Structure," *Components Packag. Technol. IEEE Trans.*, vol. 31, no. 3, pp. 552–558, 2008. [Online]. Available: http://ieeexplore.ieee.org/search/srchabstract.jsp?tp={&}arnumber=4609951{&}queryText=Superlattice+Microrefrigerator{&}openedRefinements=*{&}searchField=Search+All 26, 30, 82, 99

[44] Wikipedia, "http://en.wikipedia.org/wiki/Thermoelectric_effect," 2010. [Online]. Available: http://en.wikipedia.org/wiki/Thermoelectric{_}effect 28

[45] PCBheaven, "The Peltier Thermo-Element," 2009. [Online]. Available: http://pcbheaven.com/wikipages/The{_}Peltier{_}Thermo-Element/ 28

[46] Warsash Scientific, "Marlow Industries, Thermoelectric Coolers (TECs)," 2012. [Online]. Available: http://www.warsash.com.au/suppliers/marlow-industries.php 29

[47] L. Han and C. Wang, "Advances in Thermoelectric Microcooling," in *Electron. Packag. Technol. High Density Packag. (ICEPT-HDP), 2010 11th Int. Conf.*, 2010, pp. 1359–1361. [Online]. Available: http://ieeexplore.ieee.org/search/srchabstract.jsp?tp={&}arnumber=5582813{&}queryText=Advances+in+Thermoelectric+Microcooling{&}openedRefinements=*{&}searchField=Search+All 30, 31

[48] J. Zhang, N. G. Anderson, and K. M. Lau, "AlGaAs Superlattice Microcoolers," *Appl. Phys. Lett.*, vol. 83, no. 2, pp. 374–376, 2003. [Online]. Available: http://link.aip.org/link/APPLAB/v83/i2/p374/s1{&}Agg=doihttp://apl.aip.org/resource/1/applab/v83/i2/p374{_}s1 30, 69, 82, 84, 88, 89, 99, 116

[49] A. Shakouri, E. Y. Lee, D. L. Smith, V. Narayanamurti, and J. E. Bowers, "Thermoelectric Effects in Submicron Heterostructure Barriers," *Microscale Thermophys. Eng.*, vol. 2, no. 1, pp. 37–47, feb 1998. [Online]. Available: http://www.tandfonline.com/doi/abs/10.1080/108939598200097http://repository.ias.ac.in/30704/1/403.pdf 30, 94, 95, 96, 98

[50] A. Fitting, J. Christofferson, X. Fan, G. Zeng, C. LaBounty, J. E. Bowers, and S. Barbara, "Transient response of thin film SiGe micro coolers," in *Int. Mech. Eng. Congr. Exhib.*, 2001. 30

[51] A. Shakouri and J. E. Bowers, "Heterostructure integrated thermionic coolers," *Appl. Phys. Lett.*, vol. 71, no. 9, p. 1234, 1997. [Online]. Available: http://link.aip.org/link/APPLAB/v71/i9/p1234/s1{&}Agg=doihttp://web.ebscohost.com/ehost/detail?sid=1b22d72a-ab6c-4165-bbb6-6ef373e2cd3a@sessionmgr113{&}vid=1{&}hid=119{&}bdata=JnNpdGU9ZWhvc3QtbGl2ZQ=={#}db=aph{&}AN=4250851 30

[52] G. D. Mahan and L. M. Woods, "Multilayer Thermionic Refrigeration," *Phys. Rev. Lett.*, vol. 80, no. 18, pp. 4016–4019, may 1998. [Online]. Available: http://link.aps.org/doi/10.1103/PhysRevLett.80.4016http://shell.cas.usf.edu/{~}lwoods2/publications/p4016{_}1.pdf 30

[53] A. Shakouri, C. LaBounty, J. Piprek, P. Abraham, and J. E. Bowers, "Thermionic emission cooling in single barrier heterostructures,"

Appl. Phys. Lett., vol. 74, no. 1, p. 88, 1999. [Online]. Available: http://link.aip.org/link/APPLAB/v74/i1/p88/s1{&}Agg=doihttp://www.dtic.mil/cgi-bin/GetTRDoc?AD=ADA461836{&}Location=U2{&}doc=GetTRDoc.pdf 30

[54] G. S. Nolas and H. J. Goldsmid, "A comparison of projected thermoelectric and thermionic refrigerators," *J. Appl. Phys.*, vol. 85, no. 8, p. 4066, 1999. [Online]. Available: http://link.aip.org/link/JAPIAU/v85/i8/p4066/s1{&}Agg=doihttp://web.ebscohost.com/ehost/detail?sid=423db4e6-4bc3-40c2-81ca-8f6fc38b46b0@sessionmgr115{&}vid=1{&}hid=119{&}bdata=JnNpdGU9ZWhvc3QtbGl2ZQ=={#}db=aph{&}AN=1815789 30

[55] T. E. Humphrey, M. F. O'Dwyer, and A. Shakouri, "A further comparison of solid-state thermionic and thermoelectric refrigeration," in *Thermoelectr. 2005. ICT 2005. 24th Int. Conf.*, no. 4. Ieee, 2005, pp. 211–214. [Online]. Available: http://ieeexplore.ieee.org/lpdocs/epic03/wrapper.htm?arnumber=1519921 30

[56] M. V. Simkin and G. D. Mahan, "Minimum Thermal Conductivity of Superlattices," *Phys. Rev. Lett.*, vol. 84, no. 5, pp. 927–930, jan 2000. [Online]. Available: http://arxiv.org/abs/cond-mat/9907368http://link.aps.org/doi/10.1103/PhysRevLett.84.927 31, 107

[57] W. S. Capinski and H. J. Maris, "Thermal conductivity of GaAs/AlAs superlattices," *Phys. B Condens. Matter*, vol. 219-220, pp. 699–701, apr 1996. [Online]. Available: http://linkinghub.elsevier.com/retrieve/pii/0921452695008586http://www.sciencedirect.com/science/article/pii/0921452695008586 31

[58] S.-M. Lee, D. G. Cahill, and R. Venkatasubramanian, "Thermal conductivity of SiGe superlattices," *Appl. Phys. Lett.*, vol. 70, no. 22, pp. 2957 – 2959, 1997. [Online]. Available: http://link.aip.org/link/APPLAB/v70/i22/p2957/s1{&}Agg=doihttp://ieeexplore.ieee.org/xpl/freeabs{_}all.jsp?arnumber=4891186{&}abstractAccess=no{&}userType=insthttp://web.ebscohost.com/ehost/detail?sid=f1444d63-0a7c-438b-b3ba-c6ce1d89965f@sessionmgr14{&}vid=1{&}hid=7{&}bdata=JnNpdGU9ZWhvc3QtbGl2ZQ=={#}db=aph{&}AN=4207912 31

[59] G. D. Mahan, J. O. Sofo, and M. Bartkowiak, "Multilayer thermionic refrigerator and generator," *J. Appl. Phys.*, vol. 83, no. 9, pp. 4683 – 4689, 1998. [Online]. Available: http://link.aip.org/link/

JAPIAU/v83/i9/p4683/s1{&}Agg=doihttp://web.ebscohost.com/ehost/detail?sid=a51e51ff-56f0-49a1-a38a-78550b4e3153@sessionmgr104{&}vid=1{&}hid=119{&}bdata=JnNpdGU9ZWhvc3QtbGl2ZQ=={#}db=aph{&}AN=562189 31

[60] A. Shakouri and C. Labounty, "Material optimization for heterostructure integrated thermionic coolers," in *Thermoelectr. 1999. Eighteenth Int. Conf.*, 1999, pp. 35–39. [Online]. Available: http://ieeexplore.ieee.org/lpdocs/epic03/wrapper.htm?arnumber=843329{%}5Cnhttp://www.dtic.mil/cgi-bin/GetTRDoc?AD=ADA460087{&}Location=U2{&}doc=GetTRDoc.pdf 31

[61] R. Singh, D. Vashaee, Y. Zhang, M. Negassi, A. Shakouri, Y. Okuno, G. Zeng, C. LaBounty, and J. E. Bowers, "Experimental Characterization and Modeling of InP-based Microcoolers," *MRS Proc.*, vol. 793, pp. 1–7, feb 2004. [Online]. Available: http://journals.cambridge.org/abstract{_}S1946427400103768www.ece.ucsb.edu/uoeg/publications/papers/singh04mrs.pdf 31, 99

[62] A. Shakouri and J. E. Bowers, "Heterostructure integrated thermionic refrigeration," in *Thermoelectr. 1997. Proc. ICT '97. XVI Int. Conf.*, no. 1 997. IEEE, 1997, pp. 636–640. [Online]. Available: http://ieeexplore.ieee.org/lpdocs/epic03/wrapper.htm?arnumber=667610 31

[63] R. H. Hopper, I. Haneef, S. Z. Ali, F. Udrea, and C. H. Oxley, "Use of carbon micro-particles for improved infrared temperature measurement of CMOS MEMS devices," *Meas. Sci. Technol.*, vol. 21, no. 4, p. 45107, 2010. [Online]. Available: http://stacks.iop.org/0957-0233/21/i=4/a=045107 41

[64] Scientifica, "PatchStar Motorised Micromanipulator." [Online]. Available: http://www.scientifica.uk.com/products/scientifica-patchstar-micromanipulator 42, 44

[65] Y. Zhou and B. J. Nelson, "The effect of material properties and gripping force on micrograsping," *Proc. 2000 ICRA. Millenn. Conf. IEEE Int. Conf. Robot. Autom. Symp. Proc. (Cat. No.00CH37065)*, vol. 2, no. April, pp. 1115–1120, 2000. [Online]. Available: http://ieeexplore.ieee.org/lpdocs/epic03/wrapper.htm?arnumber=844748 43

[66] G. M. Dunn, A. Phillips, and P. J. Topham, "Gunn instabilities in power HEMTs," *Electron. Lett.*, vol. 37, no. 8, p. 530, 2001. [Online]. Available: http://digital-library.theiet.org/content/journals/10.1049/el{_}20010362http://ieeexplore.ieee.org/xpl/articleDetails.jsp?

tp={&}arnumber=920004{&}searchWithin{%}3Dp{_}Publication{_}Number{%}3A2220{%}26searchWithin{%}3Dp{_}Volume{%}3A37{%}26searchWithin{%}3Dp{_}Issue{%}3A8{%}26searchWit 46

[67] S. Chandran, "IV Automation of Gunn Diodes," Masters Thesis, De Montfort University, Leicester, UK, 2011. 52

[68] S. J. J. Teng and R. E. Goldwasser, "High-performance second-harmonic operation W-band GaAs Gunn diodes," *Electron Device Lett. IEEE*, vol. 10, no. 9, pp. 412–414, 1989. [Online]. Available: http://ieeexplore.ieee.org/lpdocs/epic03/wrapper.htm?arnumber=34726http://ieeexplore.ieee.org/search/srchabstract.jsp?tp={&}arnumber=34726{&}queryText=High-performance+second-harmonics+operation+w-band+GaAs+Gunn+diode{&}openedRefinements=*{&}searchField=Search+All 71

[69] N. J. Pilgrim, A. Khalid, G. M. Dunn, and D. R. S. Cumming, "Gunn oscillations in planar heterostructure diodes," *Semicond. Sci. Technol.*, vol. 23, no. 7, pp. 1–10, jul 2008. [Online]. Available: http://stacks.iop.org/0268-1242/23/i=7/a=075013?key=crossref.ed03b17eb848fb82479eaf51c7f71a0d 71

[70] C. Li, A. Khalid, L. B. Lok, N. J. Pilgrim, M. C. Holland, G. M. Dunn, and D. R. S. Cumming, "An In0.23Ga0.77As-based pHEMT-like Planar Gunn Diode Operating at 116 GHz," in *Infrared Millim. Terahertz Waves (IRMMW-THz), 2010 35th Int. Conf.*, 2010, pp. 1–3. [Online]. Available: http://ieeexplore.ieee.org/search/srchabstract.jsp?tp={&}arnumber=5612507{&}queryText=An+In0.23Ga0.77As-based+pHEMT-like+Planar+Gunn+Diode+Operating+at+116+GHz{&}openedRefinements=*{&}searchField=Search+All 71

[71] A. Goetzberger and R. M. Scarlett, "Research and investigation of inverse epitaxial UHF power transistors," AF Avionics Laboratory, Research and Technology Division, Air Force Systems Command, Wright-Patterson Air Force Base, Ohio, AF Avionics Laboratory, Research and Technology Division, Air Force Systems Command, Wright-Patterson Air Force Base, Ohio, Tech. Rep., 1964. [Online]. Available: http://oai.dtic.mil/oai/oai?verb=getRecord{&}metadataPrefix=html{&}identifier=AD0605376 73, 75

[72] G. K. Reeves and H. B. Harrison, "Obtaining the specific contact resistance from transmission line model measurements," *IEEE Electron Device Lett.*, vol. 3, no. 5, pp. 111–113, may 1982. [Online]. Available: http:

//ieeexplore.ieee.org/lpdocs/epic03/wrapper.htm?arnumber=1482607 75, 76, 77, 92

[73] Y. Zhang, G. Zeng, J. Piprek, A. Bar-Cohen, and A. Shakouri, "Superlattice microrefrigerators flip-chip bonded with optoelectronic devices," in *Twent. Annu. IEEE Semicond. Therm. Meas. Manag. Symp. (IEEE Cat. No.04CH37545).* IEEE, 2004, pp. 190–197. [Online]. Available: http://ieeexplore.ieee.org/xpls/abs{_}all.jsp?arnumber=1320474http://ieeexplore.ieee.org/lpdocs/epic03/wrapper.htm?arnumber=1320474 82, 84, 99

[74] V. Litvinovitch, P. Wang, and A. Bar-Cohen, "Superlattice TEC Hot Spot Cooling," *Components Packag. Technol. IEEE Trans.*, vol. 33, no. 1, pp. 229–239, 2010. [Online]. Available: http://ieeexplore.ieee.org/search/srchabstract.jsp?tp={&}arnumber=5291741{&}queryText=Superlattice+?TEC+Hot+Spot+Cooling{&}openedRefinements=*{&}searchField=Search+All 82

[75] J. Zhang, N. Anderson, and K. Lau, "Al/sub 0.10/Ga/sub 0.90/As-GaAs microcoolers," *IEEE Electron Device Lett.*, vol. 25, no. 6, pp. 345–347, jun 2004. [Online]. Available: http://ieeexplore.ieee.org/lpdocs/epic03/wrapper.htm?arnumber=1302221 82, 84, 99

[76] A. Stephen, G. M. Dunn, C. H. Oxley, J. Glover, M. Montes Bajo, D. R. S. Cumming, A. Khalid, and M. Kuball, "Improvements in thermionic cooling through engineering of the heterostructure interface using Monte Carlo simulations," *J. Appl. Phys.*, vol. 114, no. 4, p. 043717, 2013. [Online]. Available: http://link.aip.org/link/JAPIAU/v114/i4/p043717/s1{&}Agg=doihttp://scitation.aip.org/content/aip/journal/jap/114/4/10.1063/1.4817087 92

[77] A. Stephen, G. M. Dunn, J. Glover, C. H. Oxley, M. M. Bajo, D. R. S. Cumming, A. Khalid, and M. Kuball, "Micro-cooler enhancements by barrier interface analysis," *AIP Adv.*, vol. 4, no. 2, p. 027105, feb 2014. [Online]. Available: http://scitation.aip.org/content/aip/journal/adva/4/2/10.1063/1.4865251 92

[78] A. Shakouri, C. LaBounty, P. Abraham, J. Piprek, and J. E. Bowers, "Enhanced thermionic emission cooling in high barrier superlattice heterostructures," in *Mater. Res. Soc. Symp. Proc.*, vol. 545. MATERIALS RESEARCH SOCIETY, 1999, pp. 449 – 458. [Online]. Available: http://www.soe.ucsc.edu/{~}ali/MRS98.pdf 94, 95, 96, 98

[79] C. LaBounty, "Heterostructure Integrated Thermionic Cooling of Optoelectronic Devices," PhD Thesis, University of California, Santa Barbara, CA, 2001. [Online]. Available: http://citeseerx.ist.psu.edu/viewdoc/download?doi=10.1.1.133.2771{&}rep=rep1{&}type=pdf 99

[80] H. Chen, L. Hsu, and X. Wei, "A novel VLSI technology to manufacture high-density thermoelectric cooling devices," in *Therm. Investig. ICs Syst. 2007. THERMINIC 2007. 13th Int. Work.*, 2007, pp. 66 – 71. [Online]. Available: http://ieeexplore.ieee.org/search/srchabstract.jsp?tp={&}arnumber=4451749{&}queryText=novel+vlsi+technology+to+manufacture+high+density+themmoelectric+cooling+devices{&}openedRefinements=*{&}searchField=Search+All 99

[81] J. Christofferson, K. Maize, Y. Ezzahri, J. Shabani, X. Wang, and A. Shakouri, "Microscale and Nanoscale Thermal Characterization Techniques," in *2007 Int. Conf. Therm. Issues Emerg. Technol. Theory Appl.* IEEE, jan 2007, pp. 3–9. [Online]. Available: http://ieeexplore.ieee.org/lpdocs/epic03/wrapper.htm?arnumber=4211077 99

[82] M. Zebarjadi, A. Shakouri, and K. Esfarjani, "Thermoelectric transport perpendicular to thin-film heterostructures calculated using the Monte Carlo technique," *Phys. Rev. B*, vol. 74, no. 19, pp. 1–11, nov 2006. [Online]. Available: http://arxiv.org/abs/cond-mat/0610056http://link.aps.org/doi/10.1103/PhysRevB.74.195331 99

[83] B. J. Huang, C. J. Chin, and C. L. Duang, "A design method of thermoelectric cooler," *Int. J. Refrig.*, vol. 23, no. 3, pp. 208–218, 2000. [Online]. Available: http://www.sciencedirect.com/science?{_}ob=ArticleURL{&}{_}udi=B6V4R-3YXB29M-4{&}{_}user=698911{&}{_}coverDate=05/31/2000{&}{_}rdoc=1{&}{_}fmt=high{&}{_}orig=gateway{&}{_}origin=gateway{&}{_}sort=d{&}{_}docanchor={&}view=c{&}{_}acct=C000039118{&}{_}version=1{&}{_}urlVersion=0{&}{_}userid=698911{&}md5=e2eab3353610a67627611e4d08962888{&}searchtype=a 99

[84] S. Adachi, "Lattice thermal conductivity of group-IV and IIIV semiconductor alloys," *J. Appl. Phys.*, vol. 102, no. 6, p. 063502, 2007. [Online]. Available: http://scitation.aip.org/content/aip/journal/jap/102/6/10.1063/1.2779259 105, 106, 107

[85] V. Palankovski, "Simulation of Heterojunction Bipolar Transistors," Doctor of Technical Sciences, Technical University of Vienna, 2000. [Online]. Available: http://www.iue.tuwien.ac.at/phd/palankovski/ 105, 106, 107

[86] M. Abrahams, R. Braunstein, and F. Rosi, "Thermal, electrical and optical properties of (In,Ga)as alloys," *J. Phys. Chem. Solids*, vol. 10, no. 2-3, pp. 204–210, jul 1959. [Online]. Available: http://linkinghub.elsevier.com/retrieve/pii/0022369759900769 105, 106

[87] S. Huxtable, A. Shakouri, P. Abraham, Y.-J. Chiu, X. Fan, J. Bowers, and A. Majumdar, "Thermal conductivity of indium phosphide based superlattices," in *Eighteenth Int. Conf. Thermoelectr. Proceedings, ICT'99 (Cat. No.99TH8407)*, vol. 4, no. 3. IEEE, jul 1999, pp. 594–597. [Online]. Available: http://ieeexplore.ieee.org/xpls/abs{_}all.jsp?arnumber=843459 107

[88] Ioffe Institute, "Semiconductors on NSM," 2012. [Online]. Available: http://www.ioffe.ru/SVA/NSM/Semicond/index.html 112